Biomechanical Evaluation of Bone Marrow Lesions in the Knee

Oluwasegun Deborah Kayode

Submitted in accordance with the requirements for the degree of

Doctor of Philosophy

The University of Leeds

Institute of Medical and Biological Engineering

School of Mechanical Engineering

December, 2022

The candidate confirms that the work submitted is her own and that appropriate credit has been given where reference has been made to the work of others.

This copy has been supplied on the understanding that it is copyright material and that no quotation from the thesis may be published without proper acknowledgement.

Acknowledgements

I would like to thank my supervisors and advisors who have helped me throughout this PhD project. I would especially like to thank my primary supervisor, Professor Ruth Wilcox, for her guidance, optimism and willingness to discuss random and often last-minute bursts of ideas. I would also like to thank my co-supervisors, Dr Marlène Mengoni and Professor Philip Conaghan, for their invaluable input and many ideas that helped move the project forward. I would like to thank my post-doctoral advisor, Dr Gavin Day, and Dr Nagitha Wijayathunga for their contributions to this project and for the time and effort they took to answer my numerous questions.

I am grateful to members of my CDT cohort and the IMBE PhD office for the lunchtime chats that certainly provided much needed lightness on otherwise dreary days. The sense of collegiality in the office contributed to an overall positive of experience during this PhD.

I would like to thank my family and friends who have cheered me on and supported me with prayers, food and company during late night working sessions. I am immensely thankful to be surrounded by such great love and dedication.

Most importantly, I am incredibly full of thanks to God, my constant source of strength and encouragement, for the many privileges of my life, one of which is the opportunity to have begun and completed this PhD. All praise and glory to God forever.

Abstract

Osteoarthritis is a degenerative disease of the joint leading to pain and disability. The knee is the most common site for osteoarthritis. Bone marrow lesions (BMLs) have been associated with knee osteoarthritis symptoms and progression, however there has been limited investigation of the mechanical effects of BMLs on joint function. Subchondroplasty has been proposed as a minimally invasive surgical treatment for BMLs where the lesion site is augmented with bone substitute material in attempt to restore biomechanical function. However, it is not known how the presence of BMLs affect knee joint contact mechanics and whether augmentation of this area could address this.

The aim of the work presented in this thesis was to investigate the effect of BMLs on knee joint mechanics and to investigate the efficacy of augmentation of BML areas to restore knee joint mechanics. Computational methods were developed to model BMLs in the knee joint and augmentation cases using finite element (FE) models. Experimental methods were also developed to characterize the mechanical properties of bone in BML areas. The experimental and computational methods developed were combined to create specimen-specific models of human knee joints incorporating BMLs with derived mechanical properties.

From initial FE studies undertaken with homogenous bone material properties, it was found that the size, location, and shape of the BML affected the joint contact mechanics, especially when the elastic modulus in the BML area was much lower than the surrounding bone. Different bone morphology – to –elastic modulus relationships were derived for bone in BML and non-BML regions. Using specimen-specific FE models of cadaveric human knee joints, it was found that material properties derived through experimental tests for bone in BML regions had little mechanical effect on the cartilage and surrounding bone. However, with much lower elastic material properties, adverse effects were seen in the overlying cartilage and surrounding bone.

The mechanical properties of bone in BML areas were characterized for the first time using experimental methods developed in this thesis. The combined results indicate that subchondroplasty is only likely to be useful in cases where the bone quality in the BML region is very poor.

Table of Contents

List of Figures

List of Tables

Abbreviations

OA	Osteoarthritis
BML	Bone Marrow Lesions
FE	Finite Element
ACL	Anterior Cruciate Ligament
PCL	Posterior Cruciate Ligament
ECM	Extracellular Matrix
K&L	Kellgren and Lawrence
CT	Computed Tomography
MRI	Magnetic Resonance Imaging
WORMS	Whole-Organ MRI Scoring
BLOKS	Boston-Leeds Osteoarthritis Knee Score
MOAKS	MRI Osteoarthritis Knee Score
DICOM	Digital Imaging and Communications in Medicine
RMSE	Root Means Square Error
CCC	Concordance Correlation Coefficient

Chapter 1 : Literature review

1.1 Introduction

Osteoarthritis (OA) is a degenerative disease of the joints affecting more than 8 million people in the United Kingdom alone [1]. It is one of the lead causes of pain and disability, and the knee is the most common site of OA. Total knee replacement is the gold standard surgical intervention for knee osteoarthritis and it has been relatively successful especially in older patients. However, younger patients have reported dissatisfaction relating to pain, and range of function during activities [2-6]. There is therefore a need to develop effective early-stage interventions for knee OA with the aim of slowing down the progression of the disease and relieving symptoms.

Bone marrow lesions (BMLs) have been shown to be associated with OA progression and symptoms. The presence of BMLs has also been shown to be a predictor of subchondral bone attrition and articular cartilage denudation [7-10]. A technique ('subchondroplasty') has been developed to augment BMLs using bone substitute materials in an attempt to restore biomechanical function [11]. A small number of clinical trials have reported outcomes from subchondroplasty but there have been limited investigations of the biomechanical action of this treatment [12-18].

Finite element (FE) methods of analysis have been widely used in modelling and evaluating structural materials. The technique offers a method to evaluate complex structures that cannot be otherwise solved using classical analytical methods. Finite element analysis may be a useful tool for evaluating the mechanical effect of BMLs and providing underpinning information on the performance of subchondroplasty.

1.2 The Natural Knee Joint

The knee joint is an important load-bearing joint that enables the motion required for daily locomotion of the lower body. It consists of several complex interactions of bony and soft tissues. The knee functions to allow motion and to withstand loads arising from these movements. The knee joint is made up of two articulations; the tibiofemoral articulation between the distal femur and the proximal tibia, and the patellofemoral articulation between the posterior surface of the patella and trochlear surface of the distal femur [19]. These articulating surfaces are covered in articular cartilage to provide a smooth bearing surface and to facilitate the transmission of load through the joint [20]. The surfaces of the proximal tibia (tibia plateaus) are quite flat while the ends of the distal femur (femoral condyles) are rounded in shape. This leads to a non-conforming articulation between the tibia and the femur.

The patellofemoral articulation plays an important role in knee extension as the patella acts as a mechanical pulley, improving the extension capacity of the knee [21]. The patella bone is shaped like an upside-down triangle as shown in Figure 1.1. The posterior articulating surface of the patella is divided by the vertical ridge into two halves with the lateral half being wider to maintain patellar position [22]. The articulating surface of the patella is divided into three facets; the lateral facet, the medial facet, and the odd facet which is region without cartilage located on the periphery of the medial facet. Like the tibiofemoral joint, the bony patella and femur trochlear are incongruent therefore, the stability of the patellofemoral joint is dependent on the surrounding soft tissue structures.
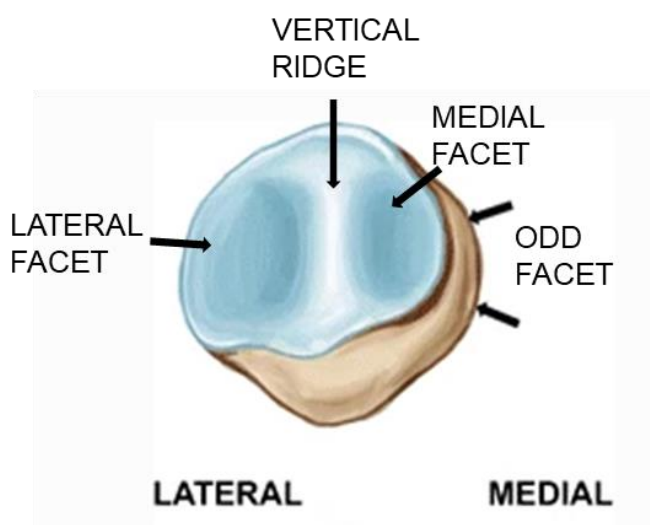
Figure 1.1: A left patella showing the bone, cartilage and facets of the patella [23]. (Adapted under creative commons license CC-BY)

As shown in Figure 1.2, the knee joint is made up other structures apart from the bone and articular cartilage. The menisci are two fibrocartilaginous structures which lie flat on the tibia and improve the conformity of the articulation between the tibia and femur. The menisci also function to withstand large hoop stresses and distribute loads of the knee joint in the medial and lateral directions. The menisci have different shapes to fit the shape and slope of the tibia plateaus and expand during compressive loads to maximize the contact area of the joint [24].

The anterior and posterior cruciate ligaments are arguably the most important ligaments of the knee. They function to restrain anterior and posterior knee motion, the anterior cruciate ligament (ACL) prevents the anterior translation of the tibia in flexion and extension, and it also resists internal rotation of the tibia. The posterior cruciate ligament (PCL) resists posterior translation of the tibia in knee flexion. The combined activity of the ACL and PCL is important for maintaining the stability of the knee joint during motion. Along with the dynamic muscles, the ACL and PCL help to balance functional and joint reaction loads involved in different phases of the gait cycle. The collateral ligaments however are primarily responsible for maintaining the medial and lateral stability of the knee joint [19].

During everyday activities such as walking, the knee joint experiences high mechanical loads of up to 3 - 3.4 times body weight [25]. Under higher impact activities such as squatting, stair climbing and running, the knee joint will experience even higher loads. Disease states such as osteoarthritis alter the normal biomechanical ability of the knee to bear these loads leading to pain and loss of function.
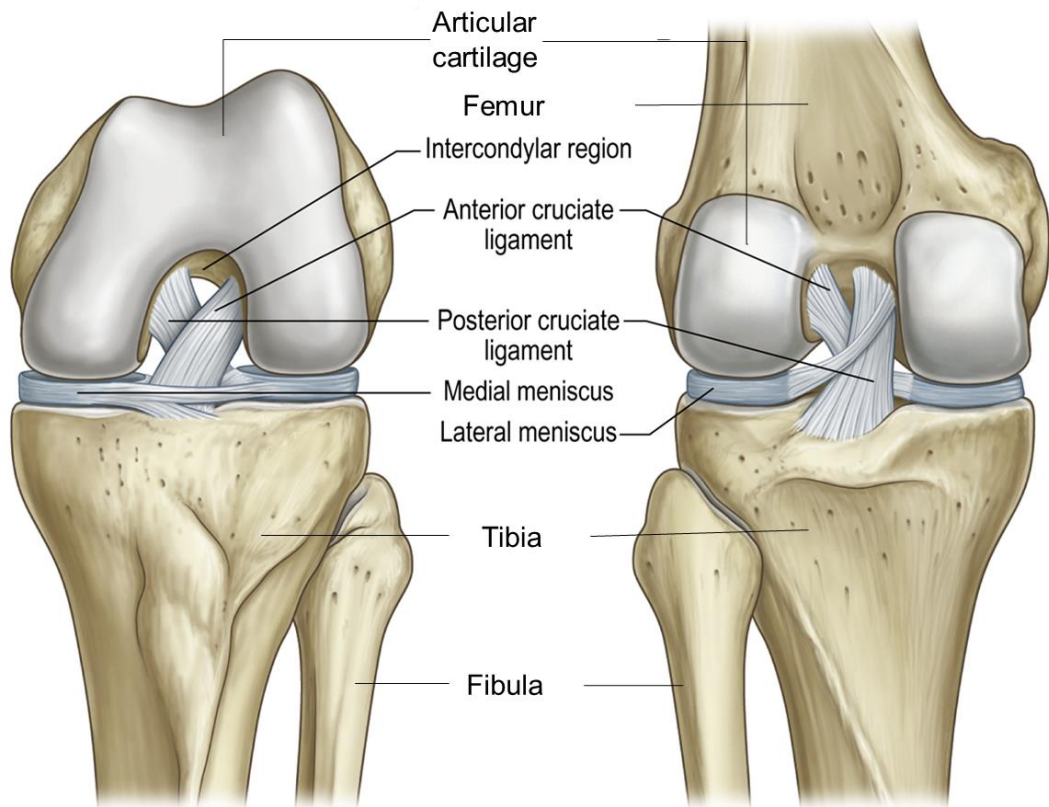
Figure 1.2: Anatomy of the natural human knee joint showing the femur, tibia, fibula, articular cartilage, lateral and medial menisci, and the anterior and posterior cruciate ligaments. (image adapted from Standring et al [26])

1.2.1 Articular cartilage

1.2.1.1 Structure

Articular cartilage is a highly specialized tissue which covers articulating surfaces of diarthrodial joints. Articular cartilage provides a lubricated low friction surface for articulation and therefore allows joint motion and facilitates the transmission of loads to the underlying bone [20, 27]. Articular cartilage consists of two phases: a fluid phase mostly composed of water along with other inorganic ions such as calcium, sodium and potassium and a solid phase consisting of the extracellular matrix (ECM) and chondrocytes [28, 29]. The ECM is composed of water, collagen, proteoglycans and other proteins and glycoproteins [30, 31].

Articular cartilage is organized into four different zones based on the collagen arrangement, ECM and chondrocyte interaction leading to unique tissue properties in each zone.
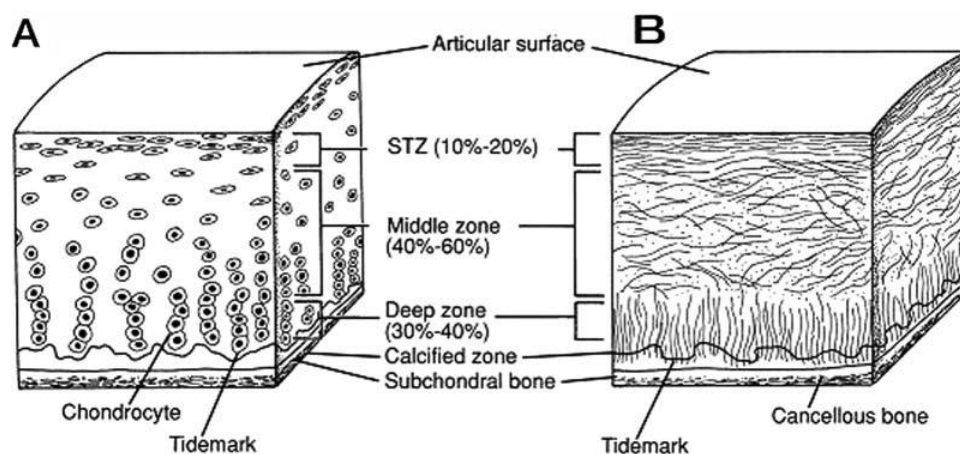
Figure 1.3: Schematic cross-sectional diagram of healthy articular cartilage: (A) cellular organization in the zones of articular cartilage; (B) collagen fibre architecture (image taken from Buckwalter et al with permission) [32].

The superficial zone is a thin zone that makes up approximately 10 – 20 % of the articular cartilage thickness and acts to protect the deeper layers from shear stresses. It can be seen from Figure 1.3 that this layer contains a high number of flattened chondrocytes all of which are responsible for its ability to resist high shear, tensile and compressive loads at the surface. The middle zone makes up 40 – 60 % of the total cartilage thickness. In this zone, collagen fibrils are thicker, more spaced out and more randomly oriented. The chondrocytes in this zone are spherical and there are fewer than in the superficial zone. In the deep zone, the collagen fibrils in this zone are the largest in diameter and arranged

perpendicular to the articular surface. The chondrocytes in the deep zone are arranged in a column parallel to the collagen fibrils. The fourth and final zone is the calcified zone which performs a very important role of fixing the cartilage to the bone. The collagen fibrils are aligned perpendicular to the articular surface and there are very few chondrocytes in this zone.

Articular cartilage is an avascular tissue, therefore the supply of nutrients into the articular cartilage occurs by diffusion through the interstitial fluid which is facilitated by the cyclic loading of the joint. Chondrocytes are responsible for maintaining homeostasis in the cartilage through balancing the development and degradation of the ECM. This is also mediated by the mechanical loading of the joint. The ECM in turn protects chondrocytes from potentially harmful biomechanical forces.

1.2.1.2 Biomechanical function

Articular cartilage functions primarily to provide a smooth low-friction surface for articulation and transmission of loads to the subchondral bone. The initial application of compressive loads causes a local increase in interstitial fluid pressure and the flowing out of some interstitial fluid from the ECM. This generates a large frictional drag on the ECM. Once the compressive load is removed, interstitial fluid flows back into the matrix [20]. Articular cartilage exhibits viscoelastic behaviour arising both from the frictional drag of the interstitial fluid and the viscoelastic properties of the collagen-proteoglycan matrix [28, 29]. Articular cartilage also demonstrates stress-relaxation and creep behaviour under compression. This means that at constant stress, the deformation increases demonstrating a creep behaviour until equilibrium is achieved.

Similarly, when a constant strain is applied to cartilage, a stress peak is reached after which stress-relaxation occurs until equilibrium is achieved.

1.2.2 Bone

Bone is a specialized tissue, an integral part of the musculoskeletal system, which plays an important role in movement and the protection of organs and soft tissues. Bone, unlike cartilage, is a highly vascularized tissue with a high cell density and is therefore able to adapt to mechanical changes and regenerate following injury.

There are cell types responsible for secreting, maintenance and removal of the organic matrix of bone. Osteoblasts are protein-secreting cells which synthesize, deposit and mineralize the organic bone matrix. When osteoblasts are embedded in the matrix they become osteoclasts. Osteocytes are the major cells types found in mature bone and are responsible for maintaining the bone matrix. Osteocyte death raises a signal for bone matrix resorption. Osteoclasts are cells responsible for the resorption of bone. The three cell types, osteoblasts, osteocytes and osteoclasts, remain in contact with one another so they are able to receive and respond to signals for bone deposition or resorption.

1.2.2.1 Structure

Bone architecture is hierarchically organized, with the heterogeneity varying based on the scale considered [33, 34]. The different structural elements at different levels of hierarchy contribute to the mechanical function of bone at the whole bone level. The major molecular components of bone are mineral calcium phosphate hydroxyapatite, type I collagen and a small proportion of non-collagenous components such as non-collagenous proteins, proteoglycans and phospholipids [35]. On the structural component level, the collagen molecules are organized into collagen fibrils with hydroxyapatite crystals deposited in the gaps within fibrils to form a mineralized composite matrix. Collagen fibrils are arranged to form arrays or bundles which are organized into a variety of patterns such as the parallel-fibered mineralized tendons found in attachment zones between tendons and bone, and a twisted plywood pattern commonly found in lamellar bone. These different patterns lead structural diversity optimised for function [34, 36].

Osteons are longitudinally cylindrical structures with layers of lamellae arrays surrounding a central hole as shown in Figure 1.4. The central hole allows resorption of bone by osteoclasts and deposition of new bone material by osteoblasts. There are other smaller features, canaliculi, built into the structures which house osteocytes. Secondary osteons with evidence of bone remodelling are known as 'Haversian canals'.

Outer circumferential lamellae

Osteon

Interstitial lamellae

Inner circumferential lamellae

Haversian canal

Periosteum

Volkmann's canal

Osteocyte lacuna

Canaliculi

Medullary trabecular bone
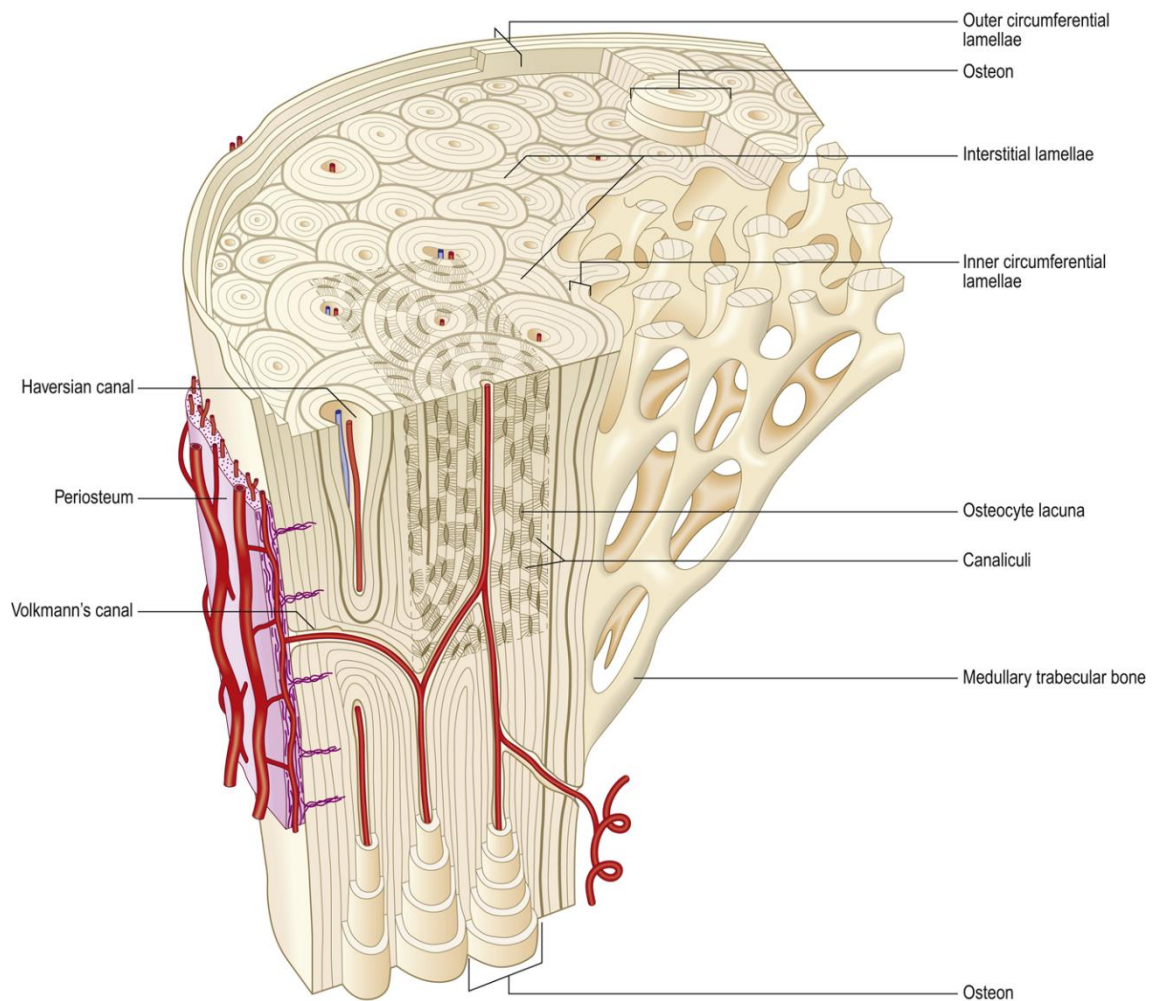
Osteon

Figure 1.4: microstructure of lamellar bone showing the general construction of osteon and contents of osteons, the arrangement osteons and lamellae in cortical bone, and trabecular bone [26]

From Figure 1.4, it can be seen that osteons are arranged parallel to one another and surrounded by lamellae in cortical bone. However, cancellous bone is a network of interconnected rod-shaped or plate-shaped trabeculae leading to a structure with variable porosity and density [26, 34].

Whole bones are made up of cortical bone and cancellous bone. The proportion of cortical to cancellous bone between and within different bones vary tailored to biomechanical function. For example, thick cortical bone is present in the diaphysis of long bone where strength in bending is required, while in the epiphysis of long bones, abundant trabecular bone spread over the volume of the epiphysis provides strength in compression [26]. The mechanical properties of bone reflect its structure and function. Even at the same

hierarchical level, mechanical properties can vary from bone to bone and between different regions of the same bone [37, 38].

The trabecular architecture of cancellous bone make it difficult to fashion into complex geometry such as the dumbbell shape especially when testing small specimen, therefore tissue level mechanical tests such as compressive tests which require simple specimen shapes like cylinders and cubes are often used to evaluate the mechanical properties of trabecular bone [39, 40].

1.3 Osteoarthritis and the Knee

Osteoarthritis (OA) is a degenerative disease of the joints affecting more than 8 million people in the United Kingdom alone [1]. It is the most prevalent joint disease, and one of the leading causes of pain and disability. The knee is the most common site for OA with an estimate of 10% of the population over the age of 55 showing symptoms of knee OA [41]. Due to the high socio-economic impacts of OA, there has been extensive evaluation of the pathological processes involved in the initiation and development of OA.

1.3.1 Diagnosis and Treatment of OA

Clinical diagnosis of OA requires careful history taking and patient reported complaints such as pain and stiffness of the joint [42]. Apart from clinical symptoms such as pain and reduced functionality, radiographs are a very important tool in diagnosing and staging of osteoarthritis. In clinical practice, the Kellgren and Lawrence (K&L) grading classification is most commonly used for the diagnosis and staging of knee osteoarthritis from radiographs [43]. As shown in Table 1.1, Kellgren and Lawrence define knee OA in five grades based on the presence of osteophytes, the narrowing of joint space and changes in the shape of bone ends. Osteophytes are fibrocartilage-capped bony outgrowths [44]

Table 1.1: Kellgren & Lawrence osteoarthritis classification and description [43].

Description	K&L Grade
None	0
Doubtful narrowing of joint space and possible osteophytic lipping	1
Definite osteophytes and possible narrowing of joint space	2
Moderate multiple osteophytes, definite narrowing of joint space and some sclerosis and possible deformity of bone ends	3
Large osteophytes, marked narrowing of joint space, severe sclerosis and definite deformity of bone ends	4

Despite the prevalence and burden of OA, no cure exists for the disease. However, there are several interventions and therapies which all aim to relieve OA symptoms, pain and restore mobility and function. Total knee arthroplasty is the gold standard treatment for end stage OA. It aims to restore the articulating surface by replacing it. However, a higher rate of dissatisfaction and poorer outcomes have been reported among patients younger than 55 [2-5]. This may be due to a difference in the expectations of younger patients.

Younger patients expect to be able to perform at more demanding levels on daily life, work and leisure activities after receiving knee replacements [6]. Unfortunately, current technology is not able to meet these expectations. There is therefore a need to develop effective therapies to target earlier stages of the disease to avoid or delay the need for total knee replacements.

1.3.2 Osteoarthritis Pathogenesis

Traditionally, OA has been thought of as a disease that primarily involved the wear of articular cartilage alone. But, research into the cartilage alone has not been able to fully define the disease pathway, therefore a more holistic approach has been adopted to investigate different tissues such as the calcified cartilage, subchondral bone and other joint capsular tissues and their involvement in OA [45].

1.3.2.1 Articular cartilage and OA pathogenesis

Advances in the definition of composition and structural organization of articular cartilage has provided great insight into the pathogenesis and pathology of OA initiation and progression. A combination of human and animal work allows investigators to create a picture of cartilage changes associated with of osteoarthritis.

The first stages of cartilage involvement in OA involve a disruption to the molecular composition and organization of the cartilage matrix. As a result, there is evidence of chondrocyte clustering in response to the changes in the ECM. This triggers an increase in catabolic activities associated with gradual loss of proteoglycans and eventual collagen degradation [46, 47] leading to an increase in compressive stiffness and reduction in hydration. This is followed by thickening of the calcified cartilage accompanied by an advancement of the tidemark and thinning of the articular cartilage [48, 49] which increases mechanical stresses in the deep zone of the cartilage which in turn accelerates the progression of OA.

1.3.2.2 Subchondral bone and OA pathogenesis

Subchondral bone refers to the calcified tissue found beneath the calcified cartilage zone of the articular cartilage. It consists of the subchondral bone plate, which is non-porous, poorly vascularized cortical bone, the underlying subchondral trabecular bone and cortical bone at joint margins [50].

Osteoarthritis is still thought of by many as primarily a disease of the articular cartilage but there is a growing community that believe that alterations in the bone may be

responsible for the initiation or progression of OA. For example, osteophytes which involve the formation of new bone at the edges of the joint, have been a hallmark in the diagnosis and staging of OA. Other changes associated to bone may also provide underpinning information on the initiation and progression of OA.

During OA, subchondral bone undergoes cell-mediated modelling and remodelling leading to a change in the architecture and mechanical properties. To maintain bone mass in a healthy state, resorption of bone by osteoclasts is balanced with bone formation by osteoblasts, and the cellular system provides information for adaptation of bone to varying mechanical loading conditions [50, 51]. However, during OA alterations in the normal modelling and remodelling process lead to a progressive increase in subchondral plate thickness, changes in the architecture of subchondral trabecular bone and osteophyte formation.

There exists a growing body of evidence that changes in subchondral bone occur early in OA and precede detectable changes in articular cartilage. In several studies Radin and colleagues [52-54] investigated the role of subchondral bone in OA initiation. It was suggested that an increase in subchondral trabecular bone stiffness led to alterations in the biomechanical environment of the overlying cartilage and subsequent changes in the cartilage structure and organization. However, a study where finite element models were constructed from microCT scans of cadaveric trabecular bone specimens from the proximal tibia of subjects with early OA associated cartilage damage indicated a different mechanism [55]. Here, the results showed that although the bone volume was increased when compared to normal donors, the elastic modulus was decreased by up to 60% at the apparent level. It was suggested that the reduction in elastic modulus was related incomplete mineralization due to increased rate of remodelling and bone turnover. These conflicting reports on the relationship between bone adaptation, subchondral trabecular stiffness, and OA initiation and progression pose a significant dilemma in creating OA therapies that target subchondral bone. However, it has been suggested that these differences represent changes seen in the subchondral bone at different stages of OA, with early OA being marked with resorption alterations and later stages of OA characterized with reparative changes involving bone sclerosis and osteophyte formation [56].

1.3.2.3 Bone marrow lesions

Magnetic resonance imaging (MRI) has been used extensively in medical practice and research. It offers the ability to visualize bone, cartilage and soft tissue at high level of detail. It can provide a unique tool for analysing and investigating structural changes in several tissues of the knee joint associated with OA. Subchondral bone alterations characterized by ill-delineated low signal intensities on T1-weighted MR images and areas of hyperintensity on T2-weighted MR images were first defined by Wilson et al in 1988 [57]. They were discovered in a group of patients with knee pain with no radiographic evidence of knee OA. They were originally termed *transient bone marrow edema*, however histological characterization showed bone marrow necrosis, bone marrow fibrosis, and other trabeculae abnormalities with very little bone marrow edema [58]. Therefore, a more general term *bone marrow lesion* (BML) has been adopted over the years and will be used in this thesis. MRI-detected subchondral bone marrow signal alterations may commonly be found in relation to joint trauma and osteoarthritis.

Figure 1.5: Fat suppressed T2-weighted magnetic resonance image of a knee in the coronal plane showing a BML in the tibia – delineated in red.

Signal alterations in BMLs, shown in Figure 1.5, are suggested to be indicative of hyperactivity and abnormal bone remodelling but little is known about mechanical properties of the bone contained in these regions. In a study by Hunter and colleagues [59] tibia bone cores of regions of BMLs were taken from postmenopausal women undergoing knee replacement surgery. Investigations of BML areas using microCT have reported several differences in the subchondral bone in BMLs compared to the subchondral bone in unaffected areas. Subchondral bone from BML regions showed

statistical significantly increased bone volume fraction and reduced tissue mineral density ($P < 0.04$) as well as increased trabecular thickness ($P = 0.02$).

In addition, several studies have found BMLs to coincide with areas of cartilage wear [60-62]. One study found that 88% of BMLs were collocated with adjacent cartilage damage in patients with symptoms and radiographic presence of medial OA [62]. Longitudinal studies have also been carried out to establish a relationship between BMLs and subsequent cartilage loss [60, 61]. A study found that the absence of BMLs at baseline resulted in a reduced risk of cartilage loss at 30-month follow up [61]. But, the presence of BMLs at baseline with continued increase in BML size increased the average odds ratio for progressive cartilage loss by 2.8. These findings are supported by Hunter et al who found a strong correlation between presence of BMLs at baseline and corresponding worsening of OA [60]. These bodies of evidence show that BMLs do play a role in the structural changes associated with OA progression. However, there are several conflicting reports on the resolution of bone marrow lesions. In one study, 50% of the lesions either reduced in size or completely resolved with no intervention at 30 months follow up [61]. But other studies have also reported increase in the size of bone marrow lesions over time and the development of new BMLs in previously unaffected regions [60, 63, 64]. This highlights the gaps that exist in the knowledge of BML mechanical properties and behaviour especially what role they may play in altering the mechanical environment of the joint. There is a need for further work into establishing the mechanical effect of BMLs on the joint.

Due to the ability of MRI to enable visualization of several tissues and structural components of the joint, several semi-quantitative scoring systems have been developed to enable multi-feature assessment of the joint. These systems score a variety of different features that have been associated to the pathophysiology of knee OA including cartilage morphology, subchondral bone marrow lesions and cysts, osteophytes, menisci, anterior and posterior cruciate ligaments and several other features. The whole-organ MRI scoring (WORMS) [65] was the first to be introduced. It graded subarticular bone marrow abnormalities in 14 articular regions based on the volume of the region involved. Subarticular bone marrow abnormality was defined as poorly margined areas of increased signal intensity in the normally fatty epiphyseal marrow on fat suppressed T2-weighted images and graded from 0 to 3 based on the volume involved as shown in Table 1.2.

Table 1.2: Descriptions of BML scoring based on WORMS [65]

Grade	Description
0	None
1	< 25% of the region
2	25% - 50% of the region
3	= > 50% of the region

Subsequently, the Boston-Leeds Osteoarthritis Knee Score (BLOKS) was developed to address some of the limitations of the WORMS particularly in how the grading of features related to clinical symptoms such as pain, and to cartilage loss [66]. In BLOKS, BMLs are graded based on:

(i)   Size
(ii)   The percentage surface area of the lesion which is adjacent to the subchondral plate
(iii)   The percentage of the lesion that is distinct from subchondral cyst.

Each criterion is graded between 0 and 3 in a similar way to WORMS. The authors reported a stronger association with pain using the BLOKS in comparison with WORMS. However, the application of BLOKS BML scoring system can be cumbersome and complex and the MRI Osteoarthritis Knee Score (MOAKS) was developed as an attempt to address the limitations of both WORMS and BLOKS [67]. In MOAKS, the knee is also divided into 14 articular sub-regions for scoring. BMLs are scored from 0-3 according to Table 1.3.

Table 1.3: Description of MOAKS Scoring system for BMLs [67].

Size of BML (including volume of any associated cysts) by volume	No. of BMLs	% of lesion that is BML
0: none		0: none
1: <33% of sub-region volume		1: <33%
2: 33 - 66% of sub-region volume		2: 33 - 66%
3: >66% of sub-region volume		3: >66%

MOAKS accounts for multiple BMLs occurring in one sub-region and cumulates them to give a single score for that region based on the total volume of the region occupied by BML. It also accounts for the volume of the BML that is distinct from cyst. A subchondral bone marrow cyst is defined as a well-defined lesion of fluid directly adjacent to the subchondral plate.

A recent classification of BMLs in the knee based on topographical location was proposed by Compagnoni et al [68]. In this six-letter (A-F) classification system shown in Figure 1.6, BMLs are classified as

A. Articular BMLs which are localized in the subchondral bone of the knee.
B. Border BMLs located in the lateral or medial cortex of the condyle or tibial plateau, with no subchondral bone involvement.
C. Complete BMLs which are combination of articular and border BML, and bigger than 50% of the medial or lateral articular surface or crosses the physis.
D. Distal BMLs which do involve either the subchondral bone or the border surface
E. Edge BMLs involve subchondral bone and border of the condyle and are smaller than 50% of the medial or lateral articular surface and stay within the physis.
F. Full BMLs extend to both medial and lateral region of the femur or the tibia.
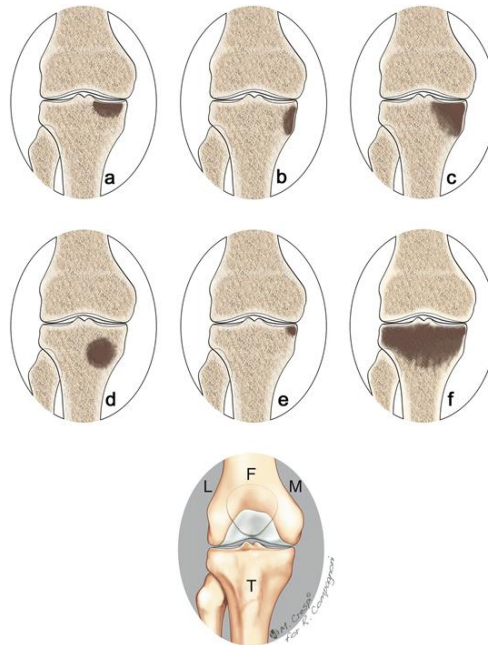
Figure 1.6: Classification of bone marrow lesions by anatomical location (figure taken from Compagnoni et al with permission) [68]

Several studies have used these scoring systems to grade MRI features associated with OA. However, there is little literature available with direct comparisons between the different scoring systems and how they relate to clinical presentation of OA.

1.3.3 Early-stage osteoarthritis

Based on the Kellgren and Lawrence (K&L) system described in Section 4.2.1, a grade of 2 is the cut-off for a definite but minimal osteoarthritis diagnosis. Although the K&L grade refers to bony structural changes associated with OA such as osteophytes, there are several other structural changes in the bone and surrounding soft tissue that cannot be picked up on a radiograph. A study of a cohort of patients with no radiographic evidence of OA (K&L grade 0) investigated structural MRI features found in the knees of these patients. The study found bone marrow lesions in 52% of the knees investigated. The study also found that osteophytes were prevalent in 74% of the knees investigated [7]. Since the definite presence of osteophytes is an important hallmark for the classification of osteoarthritis, this is a high number of osteophytes that were otherwise undetected by radiographs. This highlights the limitations of radiography as an imaging tool for diagnosis of knee osteoarthritis. It is possible that a large number of early-stage osteoarthritic knees have gone undetected. The radiograph is limited in its ability to detect structural abnormalities that may be related to the early stages of osteoarthritis (pre-radiographic osteoarthritis).

Given the rise in the prevalence of osteoarthritis and the need for the development of early-stage therapies that may modify the disease state (i.e., halt the progression of the disease), the need for early diagnosis becomes even more apparent. With the limitations of the radiograph, other imaging modalities such as MRI seem to offer unique advantages for OA classification and staging. However, the MRI features such as bone marrow lesions are yet to be definitely linked to clinical symptoms such as pain and decreased functionality. There is conflicting evidence on the link between MRI structural features and patient outcomes. Guermazi and colleagues [7] found that structural abnormalities seen on the MRI were prevalent in both painless and painful knees which suggests very low selectivity of the MRI to clinical symptom of OA such as pain. Several studies have made attempts to establish a relationship between the progression/changes in structural features and OA. Felson et al [8] found that increase in the sizes of BMLs was correlated with pain, another study [9] also found that patients with BMLs and no radiographic evidence of OA later developed knee pain and clinical symptoms of OA after 15 months. A nested-case control study found that the presence of BMLs 1 and 2 years before was

highly predictive of the diagnosis of OA [10]. The study found that while the presence of cartilage lesions did not predict OA diagnosis, the presence of BMLs did. The study also found the presence of multiple structural abnormalities to be the most predictive of OA 1 and 2 years before diagnosis. This suggests that the presence of changing BMLs and other features in the absence of radiographic evidence of OA and pain may be indicative of subsequent development of clinical OA symptoms and evidence. BMLs and other MRI features may be important markers of very early stages of OA and may therefore offer opportunities for early interventions for OA. However, more work is needed to establish a link between the MRI features, clinical symptoms and OA staging. A better understanding of the mechanical effects of these features on the joint may provide better guidance on how they relate to degenerative changes in OA.

1.3.4 Subchondroplasty

Several regenerative medicine and tissue engineered interventions are being developed to treat OA in earlier stages before the need for total knee arthroplasty. Most of them target the cartilage, including bone marrow stimulation, and autologous chondrocyte implantation, with the aim of regenerating or forming new articular cartilage. Very few therapies target the subchondral bone.

Subchondroplasty is an emerging intervention for treating OA-associated BMLs. It is a surgical procedure involving the injection of calcium-phosphate based bone substitute material into regions of BMLs. It was first described in 2007 as a method for treating joint pain relating to subchondral defect (BML). It aims to relieve pain and alter the progression of symptomatic BMLs by providing mechanical support to the diseased region of subchondral bone [11]. The surgical procedure, shown in Figure 1.7, is performed under fluoroscopic guidance in the anterior posterior view. A radiopaque cannula is inserted into the desired area and the positioning of the cannula is confirmed by comparison with preoperative MRI images. Reinforcing bone substitute material is then delivered into the area with slow and gentle pressure to prevent severe post-operative pain. Subchondroplasty is often performed in conjunction with arthroscopy to remove and material that may have escaped into the joint.
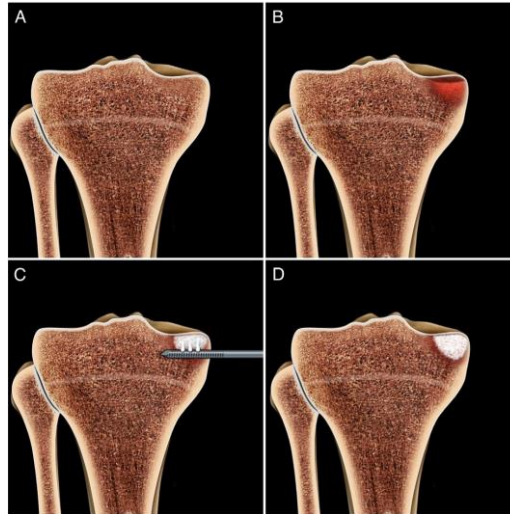
Figure 1.7: Images showing cross-sections of (a) a healthy tibia (b) A tibia with a bone marrow lesion (c) filling the BML with bone substitute material – subchondroplasty (d) tibia with reinforced bone in BML area. (image reused with permission from Colon et al [69])

There have been few studies that have used subchondroplasty for treating BMLs and have reported initial results; a summary of the findings currently available is shown in Table 1.4

Although the studies reported improvement in pain and outcome scores, all of the studies have short follow-up periods and small cohort numbers. Larger studies with longer follow-up times are needed to evaluate the effect of subchondroplasty on the progression of OA. Also, these are clinical studies and do not provide any information or insight into how the injection of bone substitute material led to improved outcome scores. However, the studies provided indications and contraindications for subchondroplasty with the main indication being the presence of OA-associated BML with pain and the most common contraindications being the presence of severe malalignment and pain due to the other pathologies. The majority of the BMLs treated in the studies were found in the medial compartment of the tibiofemoral joint with BMLs occurring in both distal femur and proximal tibia. The reason for this is not clear as BMLs have been shown to be prevalent in the medial and lateral compartments of the femur and tibia as well as in the patella [70]. The studies which included BMLs in the lateral compartment [14, 15, 18] and the patella [18] did not report any added complications or negative outcomes from doing so.

The wide age range and relatively low mean age in the studies shows prevalence of the BMLs in younger patients of not typically osteoarthritic age. One study [12] found increasing age, BMI and presence of kissing lesions (adjacent lesions in the tibia and

femur) to positively correlate with conversion to arthroplasty. This suggests that there may be characteristics that could define cohorts of patients more likely to benefit from subchondroplasty. Some studies also suggest that subchondroplasty is not suitable for patient with late-stage OA with full thickness cartilage loss [13, 14] and that these patients would benefit more from a total knee arthroplasty. However, more work is required to define, with greater clarity, clinical indications and the ideal subsets of patients likely to benefit from this treatment.

Although subchondroplasty is minimally invasive and considered safe, a few studies have reported some complications involving extravasation of the material into joint and over-pressurization which led to severe post-operative pain [12, 13].

Table 1.4: Clinical studies of subchondroplasty (continued overleaf)

Author(s)	Year	Indications	Contraindications	Number of patients	Age range (mean)	Results
Cohen & Sharkley [13]	2012	MRI detected BML with localized pain confirmed with physical examination	instability, fractures, dislocation, osteochondritis dissecans, severe malalignment (>8 degrees varus/valgus)	-	-	pain reduction
Cohen & Sharkley [12]	2015	pain for over 2 month, MRI-detected BML(s), Pain in region of BML, evidence of moderate joint disease in BML compartment	primary cause of pain and loss of function due to pathology other than BML, gross joint instability, > 8 degrees of varus or valgus, Tricompartmental K&L grade 4 OA	66	34 - 76 (55.9)	Improved pain score and function 70% survivorship at 2 years with conversion to arthroplasty being failure being end point

Farr & Cohen [15]	2013	Symptomatic knee subchondral BMLs,	-	59	35-76 (55.6)	Improved pain and function score. 75% survivorship at 2 years follow up with failure being conversion to arthroplasty
Chatterjee et al [14]	2015	presence of BML in weight bearing regions of knee and pain > 3 months	pain relating to non-degenerative meniscal tears, >8 degrees malalignment	33	38 -70 (53.5)	improved outcome scores
Fodor et al [16]	2016	MRI-detected BML with pain, grade 2 K&L score	-	1	51	increased pain and function score, improved range of motion in one year follow up
Bonadio et al [17]	2017	BML with pain > 6 months	autoimmune diseases, renal disease requiring dialysis, radiographic OA with K&L score > 3, >8 degree malalignment, radiographic alterations of patellofemoral joint	5 (4 female)	40-75	outcome improvement at 24 week follow up
Levy et al [18]	2020	Out of work due to radiographic OA with BML	-	179 (77 female)	23 -71 (54.2)	Improved pain and function with 85% return to work at 6 months. 86% survivorship at 2 years

1.3.4.1 Bone Substitute Materials

Bone substitute materials (BSMs) have been used extensively in orthopaedic surgery to fill bone defects and to fix prosthesis and fractures. The most widely used material has been poly-methyl methacrylate (PMMA). PMMA is commonly used in fixation of fractures and generally in situations requiring the reinforcement of bone [71, 72] but it has also been reported to cause damage to living bone due to the exothermic reaction of its setting [73, 74]. Calcium Phosphates (CaPs) have gained popularity in recent years because the setting reaction is endothermic and can occur at body temperature therefore it causes no damage to the surrounding biological tissue [15, 75]. CaPs also have improved handling properties as they can be injected as a paste or moulded into defects and voids. CaP cements are designed to be osteoconductive and resorbable because they are made of calcium and phosphate which are ions required for bone formation [76]. These properties make CaPs particularly suited for subchondroplasty. An important requirement for subchondroplasty is that the resulting composite of bone and material in the treated area should have similar structural properties to surrounding healthy trabecular bone to avoid stress shielding response [13]. The mechanical properties of CaP based materials can vary depending on the composition and preparation method. Some commercially available injectable BSMs and the accompanying manufacturer information on their compressive strengths are described in Table 1.5.

Table 1.5: Commercially available injectable bone substitute materials (adapted from Colon et al [69] and manufacturer's described properties)

Product (manufacturer)	Composition	Compressive Strength (MPa)
AccuFill (Zimmer Inc.)	Nanocrystalline $CaPO_4$ (CaP)	10
Beta-BSM (Zimmer Inc.)	Nanocrystalline CaP	30
Pro-Dense (Wright Medical Inc.)	CaS and CaP	40
StrucSure CP (Smith & Nephew)	Nanocrystalline CaP	24
Graftys HBS (Graftys)	Nanocrystalline CaP	12
HydroSet (Stryker)	$H_4Ca_2O_6P$, TTCP, and $Na_3C_6H_5O_7$	10 - 15
Norian SRS (DePuy Synthes)	CaP with Sodium	50

It can be seen from Table 1.5 that there is a wide variation in the compressive strengths of the commercially available BSMs. But there is no guidance given on which BSM is most suited to subchondroplasty and what mechanical properties are required for a BSM to provide adequate support in a BML without introducing additional stresses in the joint. In a study to investigate the injection behaviour and mechanical properties of eight commercially available BSMs, it was found that five out of seven materials did not maintain their physical properties when injected under pressure through a small cavity into polyurethane foam blocks [69]. The liquid component separated from the powder component, leaving the powder component in the syringe. This phase separation was seen in Beta-BSM, Pro-Dense, HydroSet and Norian. Only AccuFill, and StrucTure were able to be injected into the cavity. The injection force also differed greatly between the different BSMs with AccuFill and StrucTure giving the lowest average injection force. The amount of BSM introduced into the foam also greatly differed between BSMs. The weight and density of the BSMs were very different as well their interaction with the surrounding material/bone. It is likely that the mechanical properties of the BSM will affect the outcome of subchondroplasty, but as yet, the optimum properties are not known and there are no guidelines on what the right material would be.

1.3.5 Preclinical Animal Models

Diseases such as osteoarthritis are becoming increasingly prevalent, illustrating the need to continue to develop new and effective treatments. Before humans can benefit from treatments such as subchondroplasty, they need to be shown to be safe and effective. These can be done through preclinical testing using large animal models. Similarities in the musculoskeletal/biomechanical system between human and animals such as sheep, pigs and rabbits can be exploited to study disease progression and test new treatments. The similarities and differences between human and porcine knee joints are discussed in this section.

One important criterion for choosing a preclinical animal model for biomechanical applications is the ability to perform classical surgical or experimental testing techniques as human bone. The bones of the porcine knee joint have been shown to be large enough to receive prosthetic implants [77], withstand bone plug extraction [78] and have been tested in whole knee simulators [79], making it a good choice for an animal model.

The porcine knee joint also has the same articulating surfaces and joints as the human knee joint including the tibiofibular joint. Also, the major soft tissue structures found in the human knee, such as ligaments and meniscus, are also found in the porcine knee [80].

However, porcine knee joint is limited in extension compared to the human knee joint, being able to reach about 40°extension compared to full extension in human knee joints [80]. The differences in the range of motion between porcine and human knee joints should be kept in mind when translating data between from animal to human data.

Another important consideration is skeletal maturity. Pigs differ in life expectancy and skeletal growth than humans [81]. The properties of bone and articular cartilage will differ at different stages of maturity. Maturity should be matched between the animal model and proposed human equivalent, at the very least uniformity in age should be kept within the animal models to isolate confounding factors due to maturity.

1.4 Finite Element Modelling

The development of early-stage interventions for knee osteoarthritis require pre-clinical testing methods that are able to adequately represent the complex mechanical environment of the knee. While experimental methods can provide a controlled test environment, they are limited by the practicality, both financial and time intensity, of running many cases. Computational methods such as finite element modelling, can therefore be utilized to provide valuable information otherwise difficult to obtain from experimental tests. Computational and experimental models can be used together to improve the representation of the knee in pre-clinical testing of early-stage interventions to treat knee osteoarthritis.

Finite element (FE) methods of analysis have been widely used in modelling and evaluating structural materials. This is because they offer a method to analyse complex structures that cannot be otherwise solved using classical analytical methods. The method involves the discretization of a continuum structure into smaller sections and the application of equations to relate applied forces to nodal displacements based on the material behaviour and interactions of the structure. This usually involves making assumptions to simplify the problem. These equations are solved and the results can be propagated to provide some information in relation to the wider structure. In the field of biomechanics, finite element modelling has been utilised to investigate stresses involved in the loading and motion of the musculoskeletal system.

7.
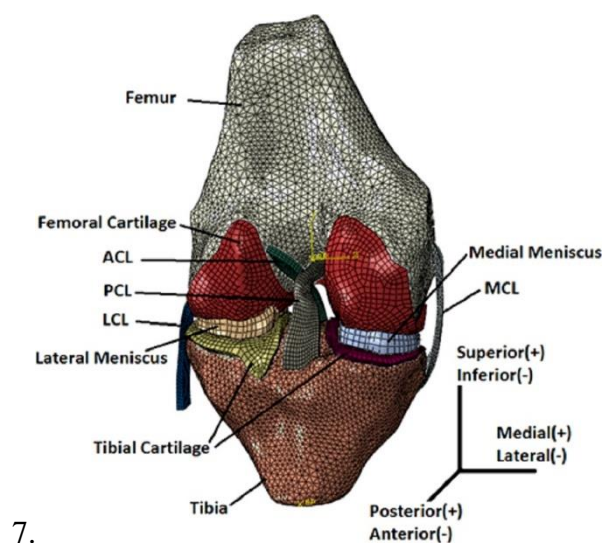
Figure 1.8: An example finite element model of human tibiofemoral joint (Image reused with permission from Beidokhti et al. [82])

Various authors have built FE models of the human tibiofemoral joint to investigate different aspects of the knee joint such as the meniscus, ligaments and articular cartilage. As with most computational experiments, assumptions and simplifications must be made to cut down computational cost and produce a model with a converged solution. Some of these models and the modelling choices made are reviewed in Table 1.6.

The main aspects of these finite element models are discussed below.

1.4.1 Geometry

The geometry of the different tissues in the joint can be represented with varying level of detail depending on the application of the model. Due to importance of the knee geometry on the joint forces, recent FE models use anatomically relevant geometries in their models usually based on computed tomography (CT) or magnetic resonance (MR) imaging. Modelling choices of some image-based FE models are summarised in Table 1.6. Some soft tissue geometry like ligaments may be excluded from the model and their effects accounted for in boundary conditions [83-86]

1.4.2 Material Properties

Many FE models of the knee joint represent the bone of the tibia and femur as rigid bodies. A reason for this is the wide difference between the stiffness of bone and that of articular cartilage and other surrounding soft tissue such as meniscus and collateral ligaments. This modelling choice is often seen in cases where the focus is on the articular cartilage and other soft tissues. A study by Donahue et al compared the contact stresses between two models of the knee [84]. The first modelled the tibia and femur bones as rigid materials while the other modelled the tibia and femur as linearly elastic homogenous materials with orthotropic properties. Results from the FE models showed less than 2% variation in the cartilage contact stresses between rigid and elastic bone and a 50% reduction in computational costs when bone was modelled as rigid bodies. This suggests modelling the tibia and femur as rigid bodies is a reasonable computational assumption when evaluating contact stress.

Bone density and bone volume fraction have been shown to be good indicators of mechanical strength and stiffness [87-90]. With the aid of advanced testing methods such as quantitative computed tomography (QCT) imaging, the density of bone can be mapped and estimated locally based on the brightness or greyscale of voxels.

A typical process for mapping material properties of trabecular bone from CT-image data would involve calibrating the CT density scanner against a phantom of known density prior to bone imaging. To generate the FE model, different techniques have been employed to segment the geometry. FE models can be generated using full range of greyscale values, or by applying a threshold to and processing the images in order to highlight the trabecular architecture in greater detail [91, 92].

After the model has been meshed, material properties can be assigned to each element based on CT density-to-elastic modulus relationships. Theoretical relationships between density and elastic modulus for cortical and trabecular bone have been calculated and reported in literature [93, 94]. Another method of determining element wise elastic modulus values is by comparing the computational stiffness of the FE model to experimental stiffness in a specimen-specific way and optimizing for a conversion factor between CT density and elastic modulus to minimize the error between computational and experimental stiffness [91]. Following the general approach outlined, element wise elastic material properties can be estimated from high resolution CT images. This allows the differences between the cortical and trabecular structures to be captured in image-based FE models.

Venalainen et al [83] studied the effect of different bone properties on the contact pressure and stresses in the knee joint. FE models of the knee were created with the bone was modelled with three different properties; rigid, homogenous elastic and inhomogeneous elastic. Homogeneous elastic bone was modelled with a Poisson's ratio of 0.3 and varying values of Young's modulus between 2 GPa and 15 GPa to match the rigid bone results. Inhomogeneous bone was modelled with the same Poisson's ratio but each trabecula was individually assigned CT-derived elastic modulus. The study found that cartilage-cartilage contact pressures were lower in the inhomogeneous bone models in comparison to the rigid bone models, with a wider variation seen in the medial side of the knee. Although the homogenous and inhomogeneous bone models gave similar cartilage stresses, significant differences of about two-fold magnitude were observed in the stresses at the cartilage-bone interface and in the subchondral bone. This suggests that trabeculae architecture is important in modelling bone especially in cases where the subchondral bone or cartilage-bone interface is of interest.

In the study by Venalainen et al [83] , all the results were compared to the rigid bone as a reference with no experimental validation. It is therefore not possible to determine if the inhomogeneous bone model was truly a more accurate representation of the in-vitro

situation. However, a study of looking at porcine osteochondral bone grafts found very good agreement between experimental and FE results in cases where the bone in the graft and host were modelled using inhomogeneous CT-derived elastic modulus values [78]. Modelling the graft bone as a uniform homogenous material led to poor agreement between FE models and experimental test results. This emphasizes again the importance of capturing trabecular architecture when modelling bone.

In the FE studies summarised in Table 1.6, cartilage and meniscus were mostly modelled as linear elastic materials with widely varied values of elastic modulus and Poisson's ratio usually taken from existing literature. A form of hyperelastic material model was the popular choice for ligaments [82, 95-97].

The choice of material model and properties will depend on existing knowledge of the structure and properties of the tissue, existing theoretical material models and be influenced by existing literature in similar applications.

1.4.3 Boundary Conditions and Loading

Motions may be applied to the FE model directly through the tibia or femur or by using boundary conditions that limit translation or rotation. Most of the studies applied constrains to the femur and tibia in restricting motion in one or more degrees of freedom to mimic a static experimental loading scenario, while applying axial load to the femur. Additional constraints such as springs were used in some cases to capture the function of the collateral ligaments in restricting anterior/posterior and medial/lateral motion [84, 86, 95].

Majority of the models modelled cartilage-to-cartilage interaction properties in a manner that allowed for sliding [84, 86, 95-97] between the two contact surfaces in a frictionless [84, 95-98] or low friction [82] contact. The femur and tibia contact surfaces are non-conforming, allowing sliding between the contact surfaces minimizes the risk of large errors due to change in the path of nodes in one contact surface in relation to the other.

1.4.4 Validation and Verification

In order to gain confidence in computational simulations, models need to be verified and validated. The ASME committee for verification and validation in computational solid mechanics [99] have defined verification as "the process of determining that a computational model accurately represents the underlying mathematical model and its solution". This basically involves testing to assess if solving the mathematical equations

have been solved correctly. While validation is defined as "the process of determining the degree to which a model is an accurate representation of the real world from the perspective of the intended uses of the model". From Table 1.6, it can be seen that different studies have validated FE models using subject-specific in-vitro results, in-vitro results from other cadaveric samples, or results published by other authors. The computational output measures and loading situation should ideally be matched to the experimental or real-life scenario as the validation method imposes limits on the wider application of the models.

Mootanah et al [95] made direct comparisons between a FE model, and a corresponding experimental specimen. The study found less than 10% difference in the peak pressures and force between the FE model and the in-vitro tests with the FE model giving higher values. This shows the possibility of getting good correlation between computational FE and experimental in-vitro tests. The FE model was validated against in-vitro test of the same cadaveric knee tested with equivalent boundary conditions and loading.

Table 1.6: Subject-specific Finite element studies of the natural knee (continued overleaf)

Author	Bone	Articular cartilage	Menisci	Ligaments	Contact interactions	Validation
Guess et al [98]	Elastic isotropic material: E= 20 GPa, v = 0.2	Elastic isotropic material: E= 15 MPa, v = 0.475	Linearly elastic transversely isotropic material: E1 = 150 MPa, E2 & E3 = 20 MPa, v1 = 0.2, v2 & v3 = 0.3	ACL and PCL modelled with springs of 400 N/mm stiffness each	frictionless small sliding interaction	Kinematics validated against Identically loaded cadaveric specimen from different author
Mootanah et al [95]	Elastic isotropic material: E= 1 GPa, v= 0.3	Elastic isotropic material: E= 25 MPa, v = 0.45	linearly elastic, transversely isotropic material: E1 = 120 MPa, E2 & E3 = 20 MPa; G12 & G13 =57.7, G23 = 8.33; v12 & v13 = 0.3, v23 = 0.2;	Neo-Hookean hyperelastic material with ligament tuning	frictionless sliding contact	Intra-articular force and pressure validated against subject-specific cadaveric in-vitro test

		Elastic Isotropic material: E = 5 MPa, v = 0.46	Elastic Isotropic material: E =59 MPa, v = 0.49	Neo-Hookean hyperelastic material	penalty method, friction coefficient = 0.01	
Beidokhti et al [82]	Rigid	Elastic Isotropic material: E = 5 MPa, v = 0.46	Elastic Isotropic material: E =59 MPa, v = 0.49	Neo-Hookean hyperelastic material	penalty method, friction coefficient = 0.01	-
Wang et al [96]	Elastic isotropic material: E= 20 GPa, v= 0.3	Elastic isotropic material: E = 10 MPa, v = 0.05 -0.45	Linearly elastic transversely isotropic material: E1 = 140 MPa, E2 & E3 = 20 MPa, v1 = 0.2, v2 & v3 = 0.3	Ogden hyperelastic material with second-order energy potential	cartilage - bone = tie ligaments - bone = tie, cartilage-menisci = frictionless finite sliding surface-surface contact with hard pressure-overclosure	cartilage stresses validated against other published studies
Venalainen et al [83]	Rigid; Homogeneous elastic isotropic E = 2-15 GPa, v = 0.3; Inhomogeneous elastic CT-derived properties, v= 0.3	fibril-reinforced poroviscoelastic material	linearly elastic transversely isotropic material	-	-	-

Donahue et al [84]	Rigid; linearly elastic isotropic material E = 0.4 GPa, v = 0.3	Elastic isotropic material: E = 15 MPa, v = 0.475	Linearly elastic transversely isotropic material: E1 = 140 MPa, E2 & E3 = 20 MPa, v1 = 0.2, v2 & v3 = 0.3	non-linear springs	frictionless, finite sliding contact with hard pressure-overclosure	-
Shirazi & Shirazi-Adl [85]	Elastic linearly isotropic material: E = 0.3 – 5 GPa, v = 0.3	fibril-reinforced hyperelastic model	fibril-reinforced hyperelastic model	-	-	validated against previous model by same author
Li et al [86]	Rigid	solid deformable	compressive springs	non-linear springs	finite sliding between cartilage-cartilage interactions	joint kinematics validated against subject-specific cadaveric specimen
Pena et al [97]	Rigid	Elastic isotropic material: E = 5 MPa, v = 0.46	Elastic isotropic material: E = 59 MPa, v = 0.49	transversely isotropic hyperelastic material	frictionless finite sliding for all interactions	cartilage stresses validated against experimental obtained by other authors

1.4.5 Modelling Bone-Cement Composite

PMMA bone cement and other bone substitute materials have been used in the orthopaedic industry for the reinforcement of bone as seen in vertebroplasty and also in implant fixation in joint arthroplasties. Large amounts of work have been carried out to understand the mechanical properties of the bone-cement formed especially in how it relates to implant loosening although that is not the focus of this review. The majority of studies have examined the behaviour in tension and shear. However, few studies have investigated the compression behaviour of bone-cement composite.

The procedure for preparation of samples has varied between the different studies. Trabecular bone cores have been extracted from different anatomical locations (tibia, femur, iliac crest, vertebrae) of animal or cadaveric human specimen. After thorough cleaning to remove marrow from the bone, bone-cement composites have been prepared in one of three ways:

(1) cement was applied to the bone core under pressure [100-102]

(2) cement was injected into the bone core until a little overflow occurred [102-104]

(3) bone-cement specimen extracted from in-vitro cemented total hip replacement [105, 106]

In all studies, bone-cement composites were then left to fully cure and thereafter shaped into smaller blocks for mechanical testing and CT imaging. Some studies investigated micro-motion in the composites using digital image correlation [105] or stepwise compression with time-lapsed micro-CT imaging [100]. Other studies investigated the gross mechanical behaviour of the bone-cement composites [102-104]. Finite element models were also created and used to investigate the mechanical behaviour of bone-cement composites [100, 101, 104, 106-109]. The FE models were validated against subject-specific experimental tests or results from experimental tests by other authors.

Experimental tests found the compressive strength and modulus of bone-cement composite to be significantly less than that of cement of alone [103, 105]. Although the studies did not directly measure the compressive mechanical properties of trabecular bone alone, they estimated from published literature, that the compressive moduli and strength of the composite was also much less than that of trabecular bone alone. However, from the rule of mixtures theory, the compressive modulus of the composite is expected to fall between that of the bone and the cement, based on the volume ratio of each component. The low compressive properties of the composite may be due to imperfect bonding

between the bone and cement. Also, the damage to trabecular structure caused by the injection is a likely contributor to the change in compressive properties.

Studies have also found the bone-cement interface to be more compliant than both bone and cement. One study found that up to 95% of the deformation in the bone-cement composite took place in partially-interdigitated regions [100]. These results are in agreement with experimental results by Mann et al [105] which found that 83% of the motion was in the regions of partial interdigitation. This body of work highlights the positive correlation between the level of interdigitation to the strength and elastic modulus of the bone-cement composite.

In terms of damage, a study by Tozzi et al found that the majority of the deformation was in the partially-interdigitated region, which resulted in trabeculae buckling and more volume of the bone being damaged in this zone [100]. In contradiction, other studies have reported more damage in the cement than in the bone with a significant amount of the cracks propagating from pre-existing cracks in the cement [105, 106]. This may be due to residual stresses from shrinkage of cement during curing. Mann et al [105] also found that contact area was positively correlated to the strength of the interface.

To fully consider contact, the influence of the morphology of the individual trabeculae structures must be considered as this would contribute to the strength and compliance at the interface in the partially interdigitated regions. A study by Helgason et al investigated the role of bone morphology in the mechanical properties of the bone-cement composite specifically the modulus of elasticity, yield stress and associated strain [109]. The study considered several morphology parameters but only found a weak correlation between those parameters and the mechanical parameters. However, the anisotropy ratio was significantly correlated (P<0.001) to the modulus of elasticity and yield stress of the bone-cement composite. The contribution of cement properties to the mechanical properties of the bone-cement composite was also tested. Low, medium and high stiffness cements were used to make bone-cement composites using bone from the same bovine tibia. The samples were tested in compression and the results showed that the relative contribution of the cement to the composite strength and stiffness increases with the increase in cement stiffness. A study by Kinzl et al also suggested that the cement bore majority of the load in the bone-cement composite because their results showed that changes in cement properties (cement stiffness) led to corresponding and significant changes in the composite strength and elastic modulus [104]. The study tested the differences between using a standard vertebroplasty cement and a low-modulus cement. Additionally, it found

no significant correlation between bone volume fraction and the strength and stiffness of the bone-cement composite. This is in agreement with other studies which also found no correlation between the bone volume fraction and the strength and stiffness of the bone-cement composite [102, 103, 109].

It is difficult to make direct comparisons between these studies because of the different methods of preparing bone-cement composites and the different anatomical site that the bone was extracted from. Jofe et al showed that different methods of creating the bone-cement composite had a significant impact on the compressive strength and modulus of the composite. Also, the mechanical properties of trabecular bone may differ based on the anatomical site and this may affect the properties of the resulting composite. In the context of subchondroplasty the bone substitute material is injected into the bone in a similar way as vertebroplasty, the resulting composite may behave similarly to composite derived from vertebroplasty [102-104, 109]. However, bone substitute materials used in subchondroplasty are calcium-phosphate based while these studies have used PMMA, the difference in material composition is likely to change the interaction between bone and substitute material.

1.4.5.1 Tissue level models

Looking at the continuum level, a few studies have attempted to model cement augmentation in the human vertebra using specimen-specific image-based FE models validated against experimental tests [91, 110-112]. Despite the complexities of modelling bone-cement composites already discussed, these studies have found very good agreement with experimental studies for apparent stiffness and strength of the vertebral body in augmented and non-augmented models. To achieve very good agreement between FE and experimental results, the following techniques were employed.

(1) Determination of element material properties based on regional bone volume fraction rather than directly from greyscale values.

(2) Creating models of augmented vertebras from a combination of registered non-augmented and augmented image data.

In Section 1.4.2, we have discussed the importance of capturing trabecular architecture in the mechanical response of FE models. This can be done by establishing a linear relationship between image greyscale and elastic modulus for each voxel. More complex relationships, such as relationships based on power law have also been used. However, a different method based of estimating a relationship between the bone volume fraction and elastic material properties have also been used. This bone volume fraction method has been shown to remove effects caused by bone marrow and trabecular spaces. Direct grayscale based models discriminate bone marrow void trabecular spaces from bone marrow filled trabecular spaces thereby altering the derived material properties [113]. Studies that used a linear relationship between greyscale image data, based on the bone volume fraction, and elastic material properties [91, 113] found better agreement between FE and experimental results compared to studies that used a linear relationship between grayscale and elastic material properties [112], or a more complex relationship between greyscale and elastic material properties [110-113].

Finite element models created from CT images of augmented vertebrae alone had very poor agreement with experimental results [91, 112]. Some studies created FE models of augmented specimens by segmenting the cement-bone composite from CT images of the augmented specimens and the rest of the vertebra from CT images of the non-augmented specimens. This method improved the agreement between computational and experimental results [91, 110, 111].

Although subchondroplasty involves a different joint, material and loading conditions to vertebroplasty, these FE studies of vertebroplasty have shown that is possible to achieve very good agreement between FE models and experiments when the focus is on apparent tissue level mechanical properties. The techniques employed in modelling non-augmented and augmented vertebrae may be adapted in modelling non-augmented and non-augmented bone in areas affected by bone marrow lesions.

1.5 Summary of Literature Review

The knee is the most common site for osteoarthritis which causes pain and disability. Osteoarthritis has been shown to cause abnormal bone remodelling and disruptions to the cartilage matrix leading to loss of cartilage height. Osteoarthritis is primarily diagnosed by looking at the joint spacing on radiographs along with clinical symptoms such as pain and loss of functionality. However, radiographs are not able to pick up several bony and soft tissue abnormalities that have been associated with OA such as bone marrow lesions. BMLs have been associated with knee OA symptoms and progression, although it is unclear what role BMLs play in altering the mechanical environment of the joint in OA.

Subchondroplasty is an augmentation technique prescribed for treating BMLs. While some clinical studies have reported early success in terms of pain and function outcomes, there are uncertainties due to the prevalence of BMLs in both symptomatic and asymptomatic knees, concerning defining subsets of patients likely to benefit from this treatment. An understanding of the mechanical effects of BMLs and subsequent augmentation of BML regions will help provide some guidance in this regard.

Finite element modelling techniques have been employed to evaluate structural materials including the knee. Current techniques have made use of in imaging technology, such as CT and MRI to capture the geometry of the bone including the trabecular architecture in good detail. CT images have also been used to map the local material properties of the bone based on voxel intensity. This level of detail in capturing differences in geometry and material properties have been shown to produce reasonable agreement between computational and experimental results when modelled individually. Advanced FE models like this can be used to investigate differences between bone in BML and non-BML regions.

Finite element models have also been used to model augmentation techniques such as vertebroplasty and to the resulting bone-cement composites in great detail. Modelling bone augmentation is complex with particular challenges in modelling the interactions between the cement and trabecular bone struts. However, there are some techniques employed in representing the overall behaviour of augmented specimens that have shown good agreement with experimental tests, which may be adapted for modelling subchondroplasty.

1.6 Aim and Objectives

The aim of this project was to investigate the effect of bone marrow lesions on knee joint mechanics in knee osteoarthritis. To achieve this aim, the following objectives were defined.

1. To develop a generic finite element (FE) model of a natural knee joint with uniform bone properties and to use this model to examine the effect on knee contact mechanics of the inclusion of a BML region with varying size, position and material properties, representing extremes of the lesion or augmentation material behaviour. This is reported in Chapter 2.

2. To develop methodologies for defining the mechanical material properties of small areas of bone using a combination of uniaxial compression testing and image-based finite element methods. This is reported in Chapter 3.

3. To apply methods developed in Objective 2 to samples of human cadaveric bone containing BMLs, and characterize differences between bone affected and unaffected by BMLs. This is reported in Chapter 4.

4. To apply methods and knowledge gained from Objectives 1 and 3 to evaluate the effect of BMLs in specimen-specific models with more realistic, inhomogeneous bone properties and to understand how variations in material property distribution in real knees affect conclusions drawn from Objective 1. This is reported in Chapter 5.

Chapter 2 : Development of Finite Element Models of the Tibiofemoral Joint

2.1 Introduction

This chapter details work carried out to develop finite element models of the tibiofemoral joint to include an idealised representation of a bone marrow lesion. As discussed in Section 1.4 of the literature review, previous models of the natural knee have mostly focussed on the soft tissues with the bone frequently represented as a rigid solid. To investigate underlying bone mechanics and pathology, it is however necessary to incorporate a more realistic and deformable bone behaviour. This study forms the first part of work carried out to achieve the first objective described in Section 1.6, to develop computational finite element models of the natural joint mechanics and the effect of varying sizes and positions of bone marrow lesions.

In this chapter, the development of a baseline model, Model 1 is first described along with some verification and mesh convergence tests to provide confidence in the FE model. Subsequently, a series of parametric studies were carried out where parameters related to the defect were changed and their effect evaluated and discussed. The model was then adapted to include the articular cartilage layers (Model 2) and further sensitivity tests were undertaken). Finally, Model 3 was developed with a hemispherical BML that better represented lesions that are located close to the subchondral bone. The different models created and their key features are described in Table 2.1.

The results and conclusions from this chapter were carried forward to inform subsequent modelling choices in finite element models of the tibiofemoral joint in the next chapters

Table 2.1: Models created and discussed in Chapter 2, key features and comparisons made between models

Name	Bone elastic modulus	Cartilage modelled?	Loading scenario	Comparisons made
Model 1	20 GPa	No	5mm displacement	Theoretical calculation, changes in size, location and elastic modulus of BML
Model 1a	20 GPa	No	2 kN	Model 2
Model 2	20 GPa	Yes	2 kN	Model 1a, Hole BML, Stiff BML, less stiff bone
Model 3	2 GPa	Yes	2 kN	Hemispherical BMLs with varying elastic modulus

2.2 Model 1: A baseline intact bone-only model

An initial finite element model containing a femur and tibia with no soft tissue was developed. The purpose of this model was to undertake a preliminary evaluation of the contact implementation by comparison with the closest theoretical (Hertzian contact) cases and to undertake preliminary sensitivity studies in a case where there were fewer confounding factors, especially due to the presence of cartilage. Parametric studies were performed on the model to determine the effect of elastic material property, size and location of BML on the knee joint. This preliminary work informed subsequent development and incorporation of BMLs in future models.

2.2.1 Model Development

2.2.1.1 Specimen characteristics

Image surface files of the tibia and femur from the Open Knee Generation 1 Specimen 1 [114] were used in this study. The Open Knee specimen is an open-source model developed from the right tibiofemoral joint of a 70-year-old female. The model contains individually segmented image files for the proximal end of the tibia, the distal end of the femur, corresponding cartilage and menisci, and the cruciate and collateral ligaments. The

knee specimen was imaged at the biomechanics laboratory of the Cleveland Clinic using a 1.0 Tesla extremity MRI scanner. The scanning protocol utilized a 3D spoiled gradient echo sequence with fat suppression, repetition time (TR) = 30 milliseconds, echo time (TE) = 6.7 milliseconds and isotropic slice thickness = 1.5 mm.

Image surface files were imported into commercial image processing software Simpleware ScanIP v.2017 (Synopsys, Mountain View, CA, USA) where they were assigned material properties and meshed. Finite element models created in ScanIP were then exported to Abaqus CAE v.2017 (Dassault Systèmes, Velizy-Villacoublay, France). BML representation

A spherical defect was created in ScanIP to represent a BML in the lateral tibia as shown in Figure 2.1.

2.2.1.2 Material properties

The bones were modelled as homogenous linearly elastic isotropic material with elastic modulus of 20 GPa and a Poisson's ratio of 0.3. This elastic modulus is high and akin to what can be expected of healthy cortical bone [96, 115]. Given the limited data available on the material properties of bone affected by BMLs, The BML area was represented in this initial model by a linear elastic isotropic material with a modulus very different to the surrounding bone (E = 200 GPa, v = 0.3).
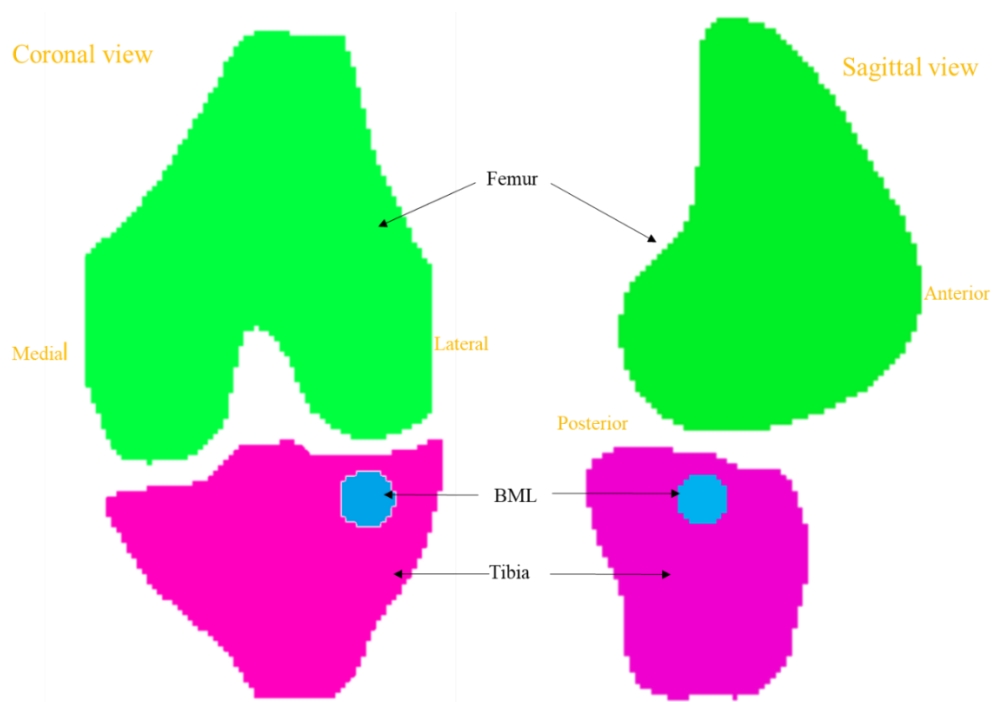
Figure 2.1: A schematic representation of a knee model showing the femur, tibia and a BML from coronal and sagittal planes.

2.2.1.3 Mesh generation

Although hexahedral elements are widely preferred to tetrahedral elements for modelling contact, they can be difficult to implement when meshing complex geometry. Studies have highlighted quadratic tetrahedral elements as good alternatives due to high accuracy and efficiency when compared to hexahedral meshes [116, 117] . Therefore, meshes with quadratic tetrahedral mesh elements were generated. The mesh density was varied as part of a mesh convergence study. Following the mesh convergence study, the same mesh density was used for models with and without BMLs.

2.2.1.4 Contact definition

Surface-to-Surface contact interaction with finite sliding was created between the tibia and the femur, with the femur as the master. The contact between the two surfaces was assumed to be frictionless with a penalty overclosure method to define the normal behaviour of the contact. These interaction properties have been successfully used in the many studies [82, 84, 96], some of which were discussed in Section 1.4.

2.2.1.5 Boundary conditions and loading

The distal end of the tibial bone was constrained for translation and rotation in all directions. A downward axial displacement of 5 mm was applied to the superior end of the femur using a reference point coupled to all the nodes of the femur, and displacement was fixed for all other degrees of freedom. The displacement was applied to close the gap between the femur and the tibia and then apply load to the joint.

2.2.1.6 Output parameters

A primary output of interest from the model was the contact pressure. This variable was used because it gives an indication of how the BML might affect other tissues beyond the bone, especially the cartilage. As discussed in Section 1.3, cartilage degeneration is a significant aspect of osteoarthritis, changes in the distribution of contact pressure in the cartilage can cause adverse loading in the cartilage and accelerate cartilage degeneration. For example, increased contact pressure in areas with thin cartilage may accelerate cartilage degeneration in those areas.

The von Mises stress distribution through the tibia was also recorded to investigate how the presence of the BML affects the distribution of stress through the bone. Von Mises stress is a scalar quantity which represents the equivalent stress state of the material before

the distortional energy reaches its yield point. This parameter is useful to investigate distortion in the bone due to the presence of a BML.

A qualitative assessment of the contact pressure was made and compared between various cases, looking at location and number of contact pressure peaks, the size of the contact area and the general appearance of the contact area. The distribution of von Mises stress through the tibia was also compared between cases. Quantitative comparison of the maximum contact pressure and the maximum von Mises stress was also made between cases.

2.2.2 Mesh Convergence Study

A mesh convergence test was carried out to find the most suitable mesh density. The mesh density was changed by varying the target edge length in ScanIP between 1 mm and 4 mm. The meshes were generated in ScanIP and element sizes were varied using the mesh coarseness function within ScanIP. This led to inconsistent variation in the element size between the cases. However, there is an approximate halving of element edge length between the cases (4 mm, ~ 2 mm, and 1 mm).

The effect of the mesh density on the maximum contact pressure and maximum von Mises stress was investigated.

2.2.3 Theoretical verification: Hertz Theory of Elastic Contact

Hertz theory of elastic contact describes the stresses at contact between two elastic curved bodies under normal displacements [118]. To apply Hertz contact simplifications, the following conditions must be met:

   i. The significant dimensions of the contact area (with radius a) must be small in comparison to the dimensions of each body and the relative radii of curvature (R) of the surfaces in contact

   ii. The surfaces are continuous and non-conforming

   iii. Each solid can be considered as an elastic half-space

   iv. The surfaces are frictionless so that pressure is only transmitted in the normal direction (perpendicular to the interface)

   v. The strains are small (small enough to lie within the scope of linear theory of elasticity)

The geometry of the knee joint is complex therefore the contact surfaces were simplified as a pair of spheres and flat planes. The femoral condyles were represented as spheres and the tibia plateaus as flat planes as shown in Figure 2.2. The widest distance in the sagittal plane of each condyle was measured from the FE model and the largest used in the theoretical calculations. Due to the small strain requirement of Hertzian contact theory, it is only applicable to make this theoretical comparison in a case where the cartilage layer is not present and the bones have a high modulus (20 GPa in this case).
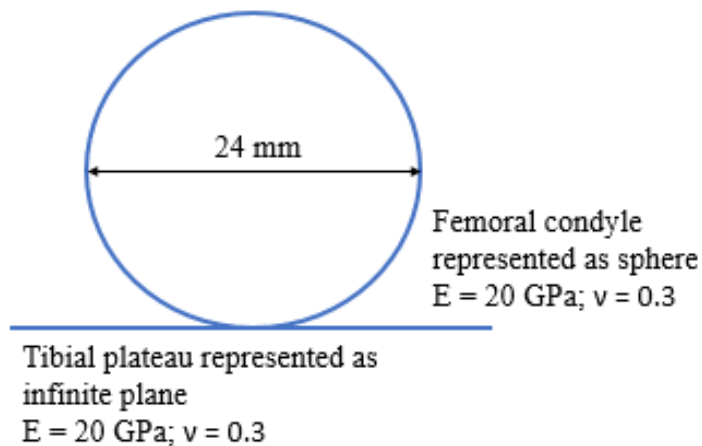
Figure 2.2: A simplified representation of the femoral condyle and tibial plateau.

The maximum contact pressure p_0 derived from Hertzian contact theory [118] is given by:

$$p_0 = \frac{3P}{2\pi a^2}$$

Equation 2.1

Where P is the total load compressing the bodies and

a is the radius of the contact area defined as:

$$a = \left(\frac{3PR}{4E^*}\right)^{1/3}$$

Equation 2.2

Where P is the total load compressing the bodies

R is the relative radii of the two bodies,

$$\frac{1}{R} = \frac{1}{R_{femur}} + \frac{1}{R_{tibia}}$$

<div align="right">**Equation 2.3**</div>

E* is the combined modulus of the two bodies,

$$\frac{1}{E^*} = \frac{1 - v_{femur}^2}{E_{femur}} + \frac{1 - v_{tibia}^2}{E_{tibia}}$$

<div align="right">**Equation 2.4**</div>

Using the dimensions from gotten from the FE models in equations defined, the contact pressure and the contact radius was compared to the results from Model 1.

2.2.4 Parametric studies on baseline Model 1

Parametric studies were carried out to investigate the effect of material property, size and location of a BML.

2.2.4.1 Change in lateral location of BML

Three models were created to investigate the effect of the lateral position of the BML on the output parameters. Each model had a 6 mm radius BML and was located 2 mm below the surface of the tibia as shown in Figure 2.3. In the first instance, the BML was aligned with the centre of contact. The BML was moved medially by 6 mm and 12 mm.
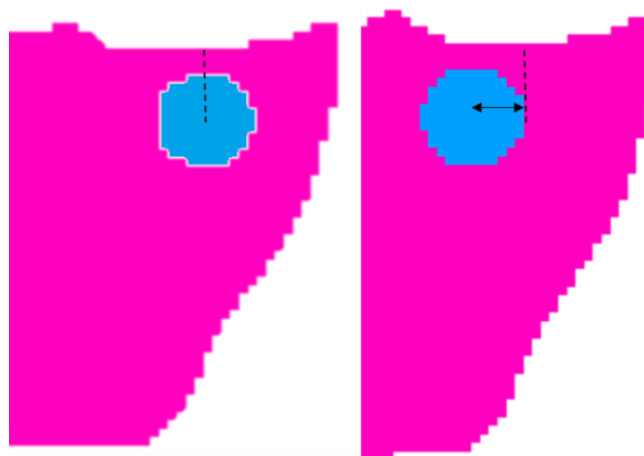
Figure 2.3: (From left to right) BML aligned with centre of contact of the tibia and BML moved by 6 mm medially.

2.2.4.2 Change in distal location of BML

Three sets of models were created to investigate the effect of increasing distance of BMLs from the tibia surface on the output parameters. A 6 mm radius BML, aligned with the centre of contact was moved distally in the tibia from 2 mm below the tibia surface to 6 mm as shown in Figure 2.4. A model was also created with the BML located 4 mm below the tibia surface.
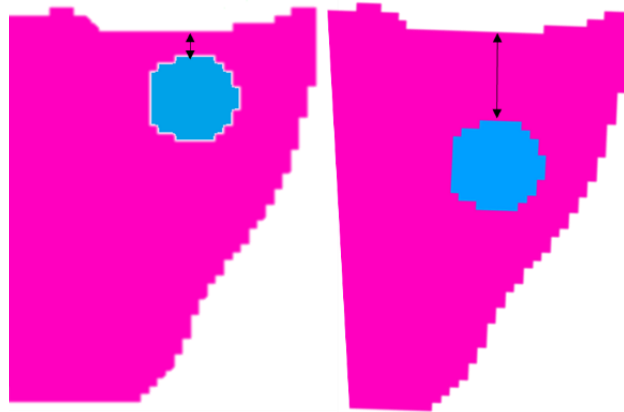
Figure 2.4: (From left to right) a schematic of a tibia showing a BML located 2 mm below the tibia surface and 6 mm below the tibia surface.

2.2.4.3 Change in size of BML

FE models were created to investigate the effect of increasing BML radius on the maximum contact pressure and distribution of von Mises stress in the knee joint. The BMLs were located 2 mm below the surface of the tibia and aligned with the centre of contact. The BML radius was varied from 2 mm to 8 mm in increments of 2 mm. These cases were selected to cover small incremental increase in the size of the BML up to the 8mm radius case where the BML diameter is similar to the width of the contact area.

2.2.4.4 Change in material property of BML

Signal alterations in MR images of BMLs are suggested to be indicative of hyperactivity and abnormal bone remodelling but little is known about mechanical properties of the bone contained in these regions. Micro-CT investigations have reported reduced tissue mineral density in comparison to subchondral bone from unaffected regions which is suggestive of reduced stiffness [59]. However, the literature also suggests increased remodelling, evidenced by increased trabecular thickness and higher bone volume fraction, which might be suggestive of higher modulus in some regions of the affected bone.

Using a model with a 6 mm radius BML located 2 mm below the tibia surface and aligned with the centre of contact, the elastic material property of the BML area was varied between a hole (an extreme case where BML provides no mechanical support) to 200 GPa (10 times the modulus of the surrounding bone) in 20 GPa increments to investigate the effect of the material property of the BML on the knee joint contact mechanics. The Hole case was created by removing the elements of the BML from the model.

In the clinical situation, the material properties of the BML and of any augmentation material are very likely to be different from the extreme cases used in these models, but these initial tests were undertaken to indicate how a range of properties might affect the surrounding structures.

2.2.5 Results

2.2.5.1 Mesh Convergence Results

Details of the element size and corresponding number of nodes and the model runtimes are shown in Table 2.2.

Table 2.2: Details of models in mesh convergence test.

Target minimum element edge length (mm)	Number of nodes	Runtime (Hours:Minutes:Seconds)
4	20307	00:00:26
1.9	31928	00:00:39
1.2	123383	00:03:37
1	236078	00:13:18

The results of the mesh convergence tests are shown in Figure 2.5 and Figure 2.6.

There is a 10 % difference in the maximum contact pressure when the element edge length is approximately halved from 4 mm to 1.9 mm. A further halving of the element edge length from 1.9 mm to 1 mm causes only 0.6 % difference in the maximum contact pressure. This reduction in the difference cases shows that the mesh is converging.

Results from Figure 2.6 show that there is a 16 % difference in the maximum von Mises stress when the element edge length is approximately halved from 4 mm to 1.9 mm. A further reduction in the element edge length from 1.9 mm to 1.2 mm also shows a 15 % difference in the von Mises stress results.

There was over a 260% increase in the runtime between the most dense and next dense mesh. However, the runtime of the highest density mesh was only 13 minutes. Therefore, the most dense mesh with element edge length of 1 mm (highlighted in Figure 2.5 and Figure 2.6) was used in the subsequent models.
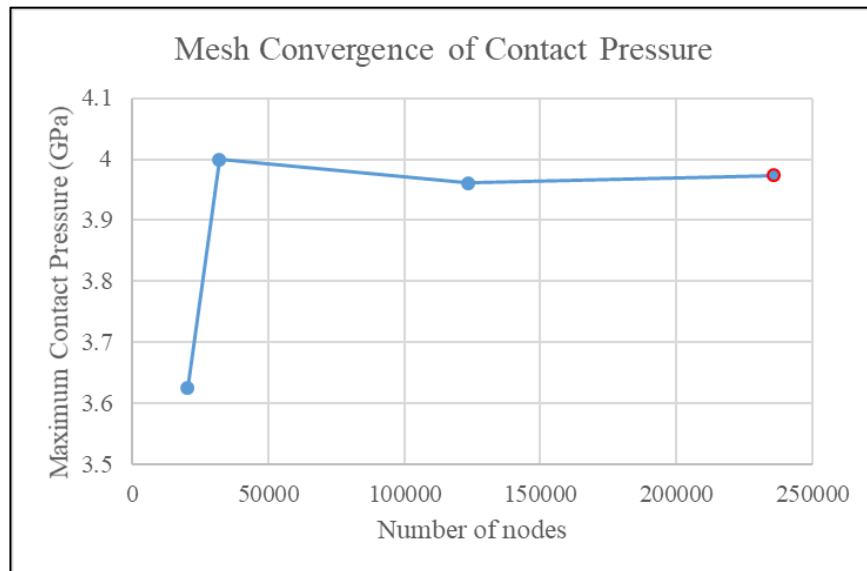
Figure 2.5: Maximum contact pressure plotted against number of nodes. The chosen mesh is highlighted in red
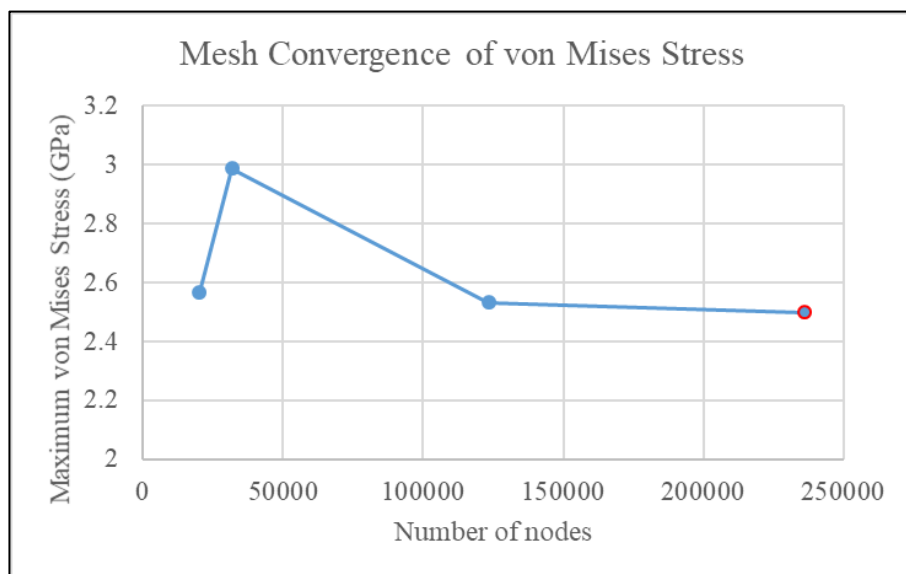
Figure 2.6: Maximum von Mises stress plotted against number of nodes. The chosen mesh is highlighted in red

2.2.5.2 Model 1: Intact Model

The maximum contact pressure and the maximum von Mises stress results from Model 1 are presented in Table 2.3.

Table 2.3: Results from Model 1

Maximum Contact Pressure (GPa)	Maximum von Mises Stress (GPa)	Contact radius (mm)	Reaction Force (kN)
3.97	2.49	5.09	156.3

2.2.5.3 Theoretical Verification

The tibia plateau is represented as a flat plane with infinite radius as seen in Figure 2.2 therefore, from Equation 2.3

$$\frac{1}{R} = \frac{1}{R_{femur}}$$

$$R = 12 \ mm$$

And using the same material properties used for the tibia and femur in the FE model, from Equation 2.4

$$E_{femur}, E_{tibia} = 20 \ GPa; \ v_{femur}, v_{tibia} = 0.3$$

$$E^* = 10.99 \ GPa$$

Inserting the reaction force from the model P = 156.3 kN into Equation 2.2,

$$a = \left(\frac{3PR}{4E^*}\right)^{1/3}$$

$$a = 7.22 \ mm$$

Inserting a into Equation 2.1: $p_0 = \frac{3P}{2\pi a^2}$

$$p_0 = 5.04 \ GPa$$

Comparing Model 1 to the theoretical calculations with idealized shape, there is a 21% difference in the maximum contact pressure and 29% difference in the contact area for the same reaction force.

2.2.5.4 Change in lateral location of BML

The effect of changing lateral distance on the maximum contact pressure and maximum von Mises stress is shown in Figure 2.7 and Figure 2.8 respectively. The results show that the further the BML was from the centre of contact, the lower the effect on the maximum contact pressure in the cartilage and the maximum von Mises stress in the surrounding bone compared to the baseline Model 1.
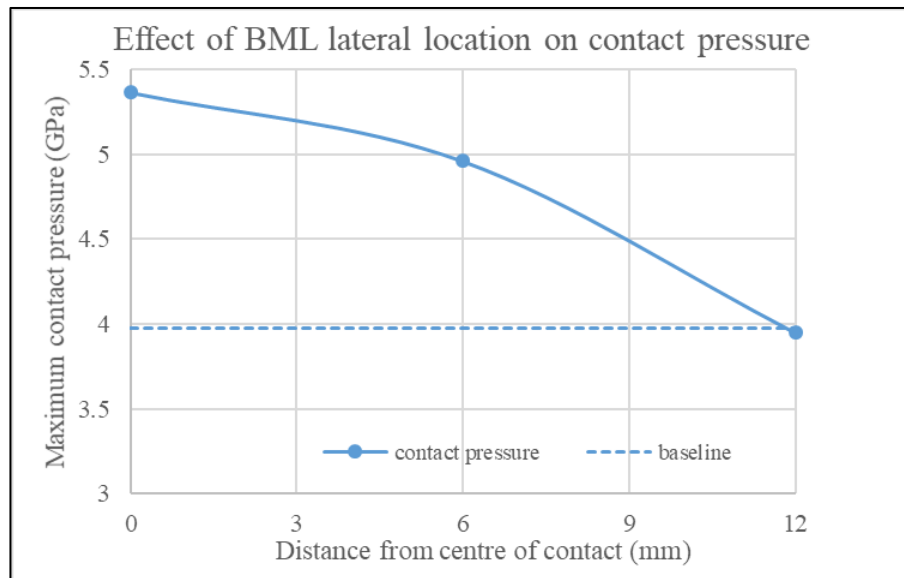
Figure 2.7: The maximum contact pressure for three different locations of BML.
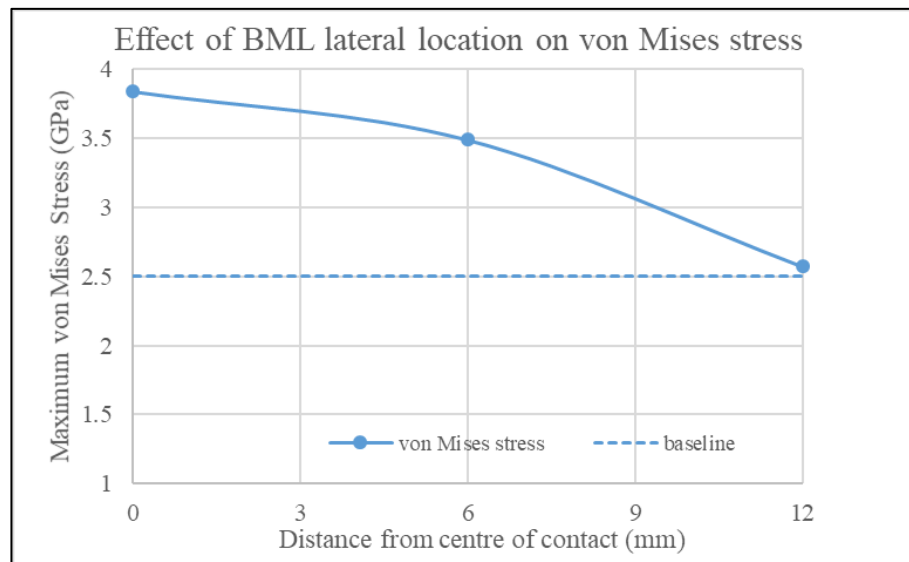
Figure 2.8: The maximum von Mises stress for three different locations of BML.

The von Mises stress distribution in the tibia and BML for the three different BML locations is shown in Figure 2.9. The BML aligned with the centre of contact (Figure 2.9b) was found to contribute most to the change in stress distribution in the tibia compared to the other scenarios (Figure 2.9c and Figure 2.9d).
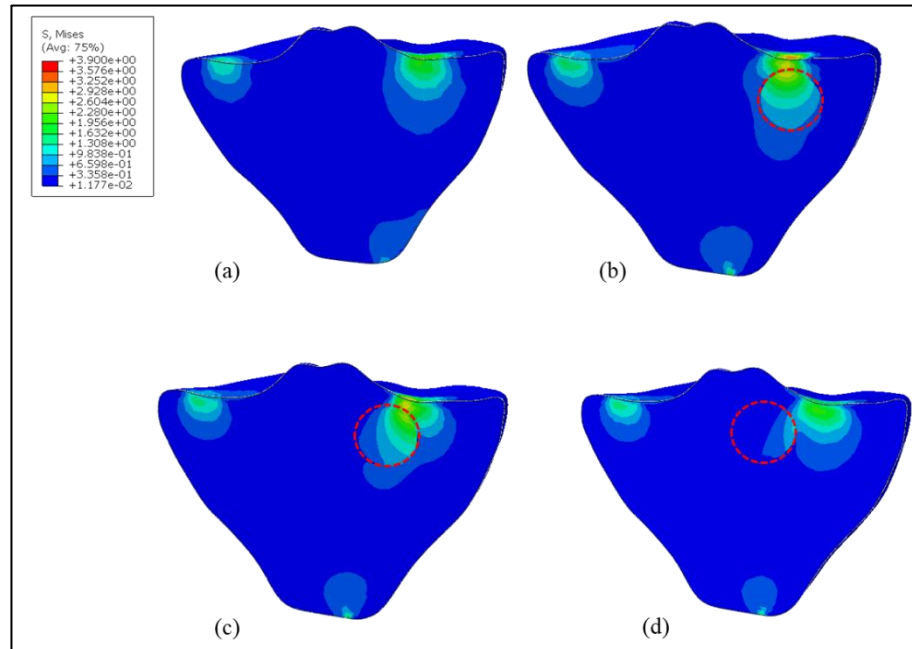
Figure 2.9: von Mises stress distribution in models (a) baseline model (b) BML aligned with centre of contact (c) BML 6 mm away from centre of contact (d) centre of BML 12 mm from centre of contact. The BML region is shown by the red dashed circle.

2.2.5.5 Change in size and distal location of BML

As shown in Figure 2.10, increasing the size of the BML generally led to an increase in the maximum contact pressure. This trend is most obvious in cases with BML located 2mm distally from the tibia surface. Also, the farther away distally the BML is from the contact surface, the less its effect on the maximum contact pressure.

A similar trend is seen in Figure 2.11, a general trend of increasing von Mises stress is seen when the BML size is increased. An increase in the distal distance of the BML from the tibia surface led to a decrease in the max von Mises stress.
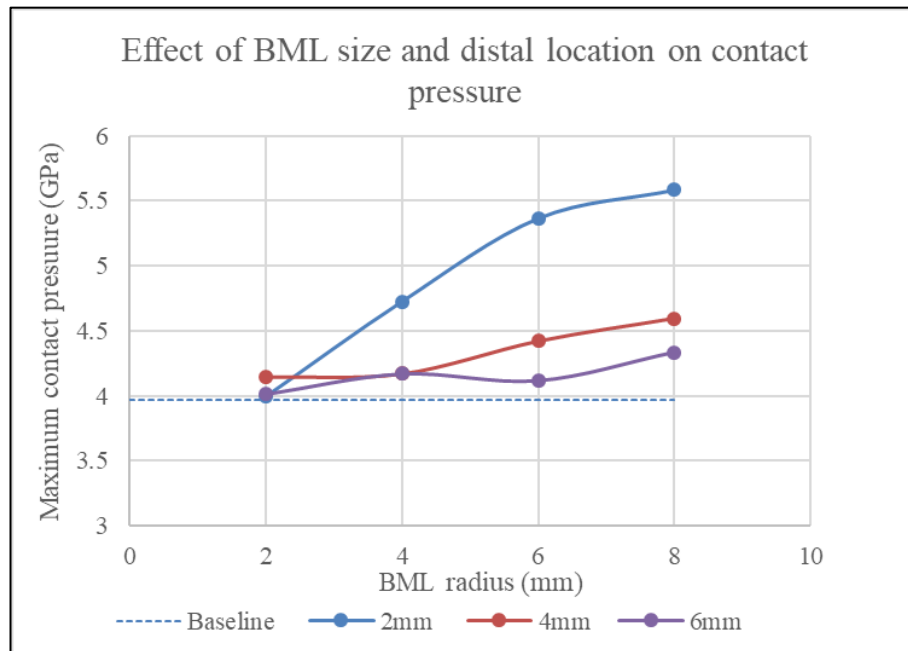
Figure 2.10: Maximum contact pressure plotted against BML radius for different sizes and distal locations of BML.
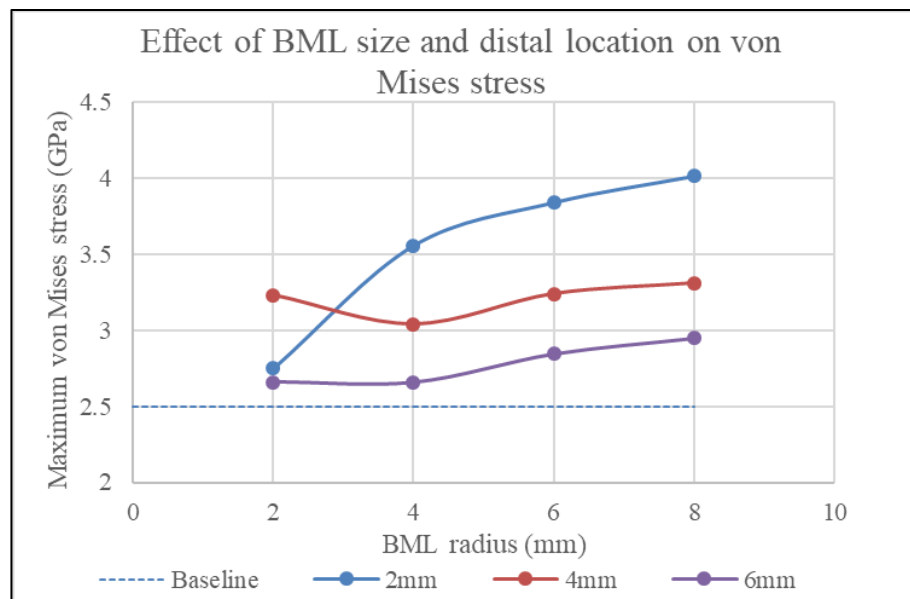
Figure 2.11: Maximum von Mises stress plotted against BML radius for different sizes and distal locations of BML.

2.2.5.6 Change in material property

An increase in the Young's modulus of the BML generally led to an increase in the maximum contact pressure and maximum von Mises stress as shown in Figure 2.12 and Figure 2.13 respectively.

A 1.8% difference was seen in the maximum contact pressure between the case with a 20 GPa BML and the baseline – which is a model with no BML, and bones with 20 GPa elastic modulus. A 5.1% difference was seen in the maximum von Mises Stress.

Having a BML with an elastic modulus less than that of the surrounding bone resulted in maximum contact pressure and von Mises stress less than the baseline model with no BML. In the hole case (plotted as 0 GPa in Figure 2.13), the maximum von Mises stress was higher than in the 10 GPa case, this may be due to high stress concentrations in the unsupported elements due to the presence of a hole.
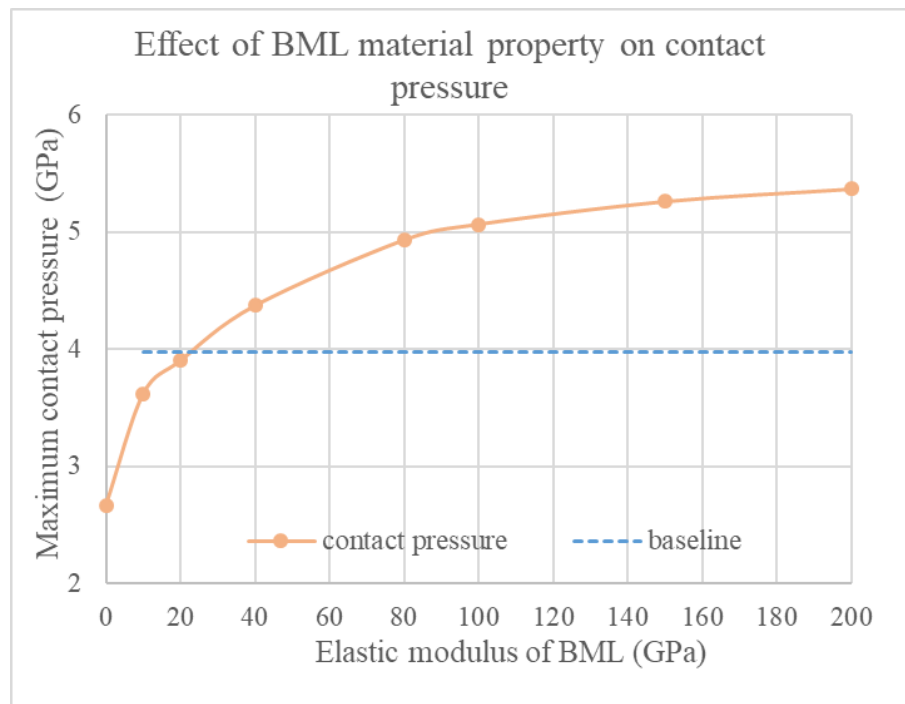
Figure 2.12: Maximum contact pressure for different elastic modulus of BML.
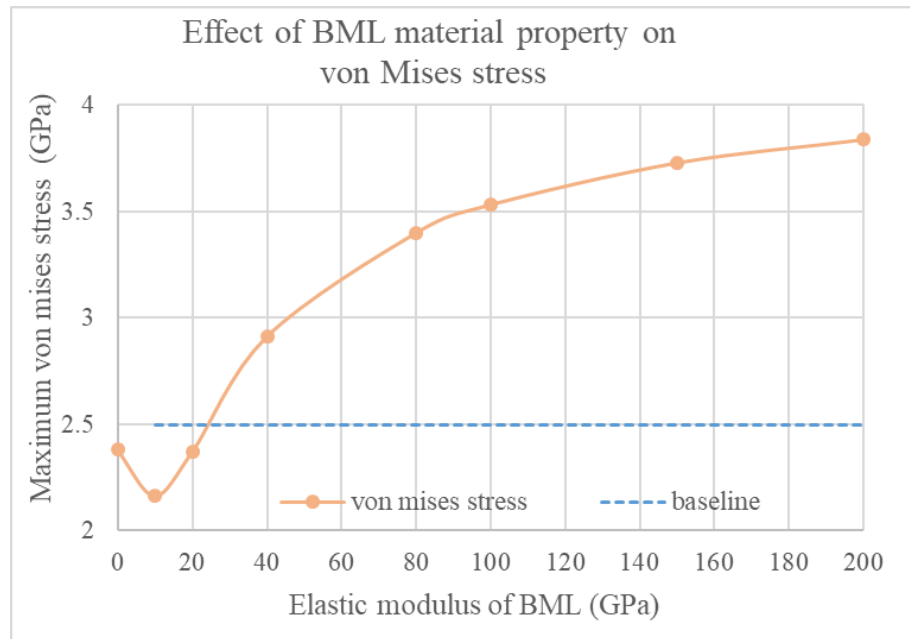
Figure 2.13: Maximum von Mises pressure for different elastic modulus of BML.

2.2.6 Discussion of Model 1

Although there are big differences between the contact pressure (21%) and contact radius (29%) calculated using Hertzian contact theory and those obtained from Model 1, the results are within the same order of magnitude. This provides a level of confidence in the model. However, a more robust validation would require experimental measurement data due to the complex shapes and materials involved (including cartilage), which is explored in Chapter 5 of this thesis.

In Model 1 the surfaces are continuous and non-conforming which satisfies the second assumption of Hertzian contact theory in Section 2.2.3. The femur and tibia are modelled as elastic solids and a frictionless interaction was applied in Model 1 which satisfies the third and fourth assumptions. The contact radius in Model 1 was 5.09 mm, which is smaller than the radius of the idealised representation of the femur (24 mm) but does not fully satisfy the first assumption of a much smaller contact radius as it is not orders of magnitude smaller. The assumption of small strain is also not met as the maximum strain in the model is greater than 1%. Also, the femur is not an ideal sphere and tibia plateau is not an ideal plane, these limitations account for the differences between the results obtained from the model and the contact theory results.

The results from the parametric studies show, as expected, that small BMLs farther away from the tibia surface distally are less likely to have significant effects on the contact pressure and the stress in the surrounding bone. From Figure 2.11, looking at the cases with BML located 4 mm below the surface of the tibia, it can be seen that there is a drop in von Mises stress between the 2 mm radius BML and 4 mm radius BML before a rise with increasing BML radius. This may be because the mesh was optimised for using a no-BML case and may not be fully converged in this case. The location of the maximum von Mises stress is localized around the BML, and may be influenced by element size in this area.

The results in Figure 2.7, Figure 2.8 and Figure 2.9 show that BMLs farther away from the centre of contact have less effect on the contact pressure and von Mises stress compared to BMLs aligned with the centre of contact. While there have been no studies simulating BML size and location in this way, some studies with simulated spherical subchondral cysts have found positive correlations between cyst size and increase in stress in the surrounding bone [119, 120]. Anwar et al [120] also investigated the effect of the distal distance of the cyst and found that cysts closer to the surface led to a larger increase in the von Mises stress in the surrounding bone than cysts farther away from the surface. In both studies the cysts were located in the weight bearing region of the joint and modelled with elastic modulus much smaller than surrounding bone.

Bowes et al [62] made a distinction between OA BMLs and ligamentous BMLs, in this study OA BML were distinct from ligamentous BMLs based on the location of BML and presence of overlapping ligament or meniscal attachments. These BMLs with soft tissue associated have also been referred to as trauma-associated BMLs [62, 121]. OA BMLs were found to collocate with areas of cartilage degeneration which were predominantly confined to the central region on the medial and tibia. These central regions are likely to see the greatest contact pressures for the largest portions of time (standing and some parts of the stance phase of the gait cycle) therefore, it is not surprising that from the parametric studies of Model 1, a BML in this region and closer to the surface of the tibia has more of an effect than one located further away from this region.

The results also show the sensitivity of the contact pressure and von Mises stress to the elastic modulus of the BML. A localized change in material property can have whole joint effects. The results highlight the importance of having more accurate information on the mechanical properties of bone in BML regions to properly define them in FE models.

There are small differences in the results for a case with a BML of 20 GPa (same elastic modulus as surrounding bone) and the baseline (which is a model with no BML and bones at 20 GPa), although in both cases all the components of the model have the same elastic modulus. These differences may be due to small differences in the mesh shape between the two models.

A limitation of this model was the absence of cartilage. This was done to enable theoretical verification, and to allow the preliminary sensitivity study which focussed only on the bone without any confounding factors due to the cartilage. Another limitation of this model was that it was controlled by applying a displacement which was easy to implement and run to a converged solution. However, a load-driven approach would be

a better alternative because physiologically relevant loads can be derived from in vivo measurements and can be applied consistently to all cases, whereas the displacement to achieve a certain load will differ from specimen to specimen.

In Model 1, bone was modelled with a high elastic modulus of 20 GPa. This is within the range of elastic modulus reported for cortical bone in literature. However, the femur and tibia are made up of both cortical and trabecular bone which would result in a structure with different elastic modulus than that of just cortical bone.

2.3 Model 2: Intact model including cartilage

This aim of this study was to generate a more physiologically relevant model by adding cartilage and more representative loading.

2.3.1 Model Development

Segmented image files for the femur cartilage and medial and lateral tibial cartilage were taken from the open knee specimen and added to the FE model described Section 2.2.1.

Mesh generation

The same mesh element size used in Model 1 (element edge length = 1 mm) was used for the bones in this model. The cartilage was also meshed using quadratic tetrahedral mesh elements and a mesh convergence study was performed where the element size of the cartilage was varied.

Material properties

The cartilage was modelled as a hyperelastic neo-hookean material with a bulk modulus, K = 41.7 MPa and shear modulus, G = 3.4 MPa. In the FE models discussed in Section 1.4 of the literature review, cartilage was modelled with elastic modulus within the range 5 - 15 MPa and a Poisson's ratio of 0.45 – 0.475 [82, 84, 95-98]. Based on Equation 2.5 and Equation 2.6, the bulk and shear modulus used were based on an equivalent elastic modulus, E = 10 MPa, and Poisson's ratio v = 0.46.

$$G = \frac{E}{(2(1 + v))}$$

Equation 2.5

$$K = \frac{E}{(2(1 - 2v))}$$

Equation 2.6

The cartilage here was modelled as a homogenous cartilage. It was discussed in Section 1.2.1 that articular cartilage is made up of different layers with different biomechanical properties. However, cartilage was modelled here as one homogenous layer of material to capture the bulk compressive behaviour and to simplify the model.

Contact definition

The cartilage layers were tied to their respective bone surfaces and surface-to-surface contact was defined between the femur cartilage and the tibia cartilage. A coefficient of friction of 0.05 was applied between the contact surfaces and a penalty overclosure method was defined. A low coefficient of friction was chosen because cartilage is a low friction material as discussed in Section 1.2.1., the value was chosen to be between frictionless [82, 84, 95, 97, 98] and 0.1 [78, 79] which have been frequently used in other finite element modelling studies in literature.

Boundary conditions and loading

The tibia was fully constrained for all translations and rotations as shown in Figure 2.14 and an initial axial displacement of 1.7 mm was applied to the femur to initiate contact between the cartilage surfaces. A load of 2 kN was then applied to the top of the femur while translations and rotations were constrained for all other directions except the axial displacement. This was done to act as an extra boundary condition to prevent excessive motion of the femur. The load applied is within the range of expected peak loads in the stance phase of the gait cycle [25], where it has been reported that the joint force is within 2 - 4 times the body weight. Loading corresponding to the stance phase was used as it was deemed most appropriate for use in quasi-static loading scenario such as in the models described in this chapter. This allows the models to be loaded in a more physiologically relevant manner in comparison to displacement control described in Model 1.
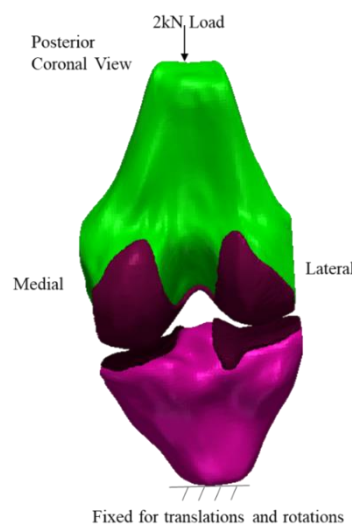
Figure 2.14: A schematic representation of Model 2 showing the loading scenario from the posterio coronal plane.

2.3.2 Mesh convergence study on cartilage

A mesh convergence study was carried out on the cartilage. The mesh density of the femoral, lateral tibial and medial tibial cartilage was changed by varying the target edge length in ScanIP between 4 mm and 0.85 mm. The meshes were generated in ScanIP and element sizes were varied using the mesh coarseness function within ScanIP. This led to inconsistent variation in the element size between the cases. However, there is an approximate halving of element edge length between the cases (4 mm, ~ 2 mm, and 0.85 mm). Halving the element edge length ensures that the number of elements across the thickness of the cartilage is increasing.

The effect of the mesh density of the cartilage on the maximum contact pressure and maximum von Mises stress were investigated.

2.3.3 Comparison of models with the same loading

To make comparisons with Model 2, the contact interactions, boundary conditions, and loading scenario in Model 1 were adjusted to create Model 1a. The results were compared between Model 1a and Model 2.

2.3.4 Parametric Studies on Model 2

2.3.4.1 Effect of BML elastic property

The results from Model 1 discussed in Section 2.2.6, show that larger BMLs had larger effects on the output parameter than smaller ones. Also, a BML aligned with the centre of contact led to an increase in the von Mises stress in the bone surrounding the BML area while a BML farther away from the centre of contact did not affect the von Mises stress distribution in the tibia. A BML size and location likely to have an effect on the output parameters was chosen. Therefore, an 8 mm radius BML was created 2 mm below the centre of contact in the tibia.

Three cases were created:

1. A model with no BML
2. A model with BML modelled as a hole to represent an extreme diseased case where the bone in the BML region is completely absent.
3. A model with BML modelled with a stiff material (E = 200 GPa) to represent an extreme augmentation case with very stiff material.

2.3.4.2 Effect of bone elastic property

To create a less stiff representation of bone and to investigate the effect of changing the elastic property of bone, another case was created. The bones were modelled with an elastic modulus of 2 GPa. All other properties of Model 2 were maintained. The contact pressure and von Mises stress results were compared to Model 2.

2.3.5 Results

The results of the mesh convergence study and the different cases considered for Model 2 are presented in this section.

2.3.5.1 Mesh Convergence Results

The details of the element sizes considered in the mesh convergence test, corresponding number of nodes and the model runtimes are shown in Table 2.4.

Table 2.4: Details of models in mesh convergence test.

Target minimum element edge length (mm)	Number of nodes	Runtime (Hours:Minutes:Seconds)
4	43534	01:05:37
1.9	67703	01:22:40
1.2	87795	01:30:36
0.85	136437	01:40:32

The results of the mesh convergence study are shown in Figure 2.15 and Figure 2.16. There is a 2 % difference in the maximum contact pressure when the element edge length is approximately halved from 4 mm to 1.9 mm. A further halving of the element edge length from 1.9 mm to 0.85 mm led to only a 1 % difference in the maximum contact pressure. This reduction in the difference cases shows that the mesh is converging.

Results from Figure 2.16 show that there is a 0.3 % difference in the maximum von Mises stress when the element edge length is approximately halved from 4 mm to 1.9 mm. A further reduction in the element edge length from 1.9 mm to 0.85 mm also shows a 0.4 % difference in the von Mises stress results. Although the results do not appear to be converging, the differences in the von Mises stress results between the cases are small compared to the differences in contact pressure results. Also, the average cartilage thickness of the femur and tibia cartilages in the model was 1.71 – 2.55 mm. An element edge length of 0.85 mm would ensure that there is more than one mesh element across the thickness of the cartilage. Therefore, the mesh with 0.85 mm element edge length and ~136,000 nodes was selected.
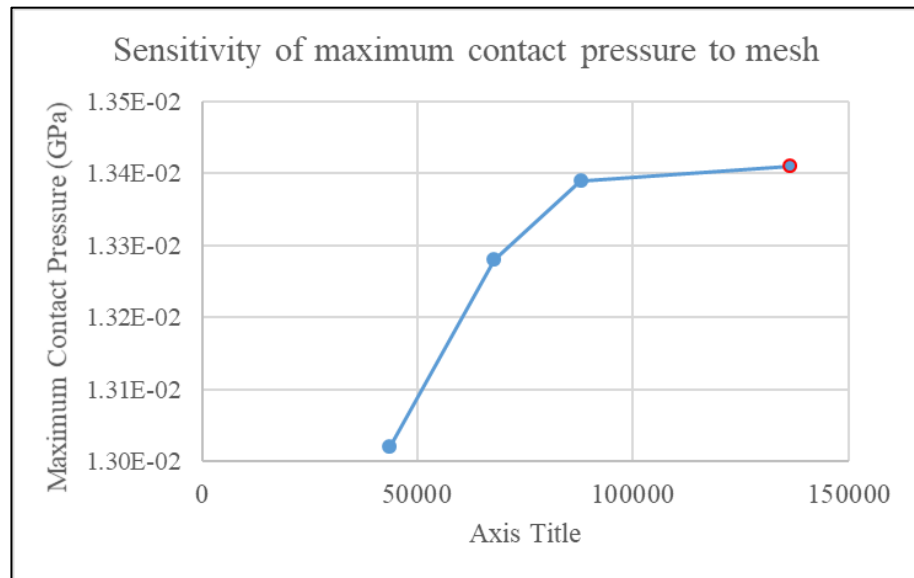
Figure 2.15: Maximum contact pressure plotted against number of nodes. The most chosen mesh is highlighted in red.
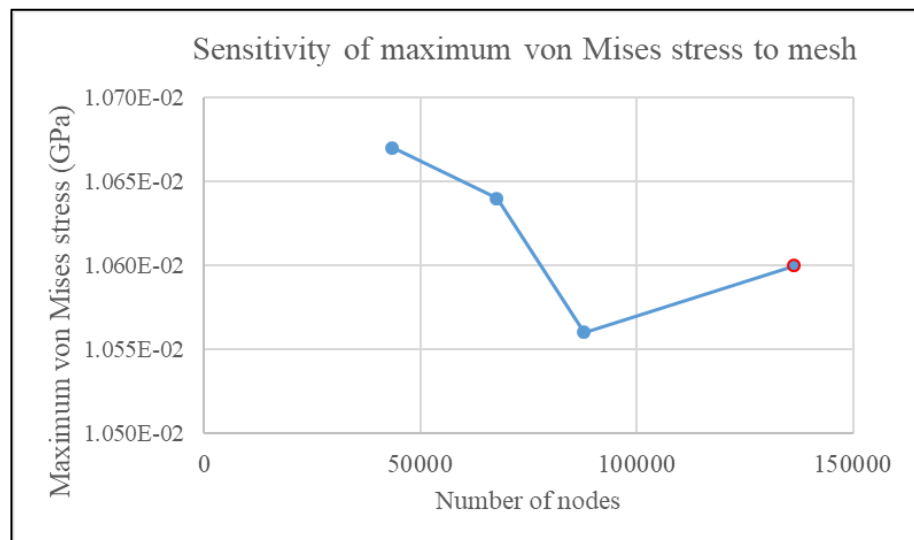
Figure 2.16: Maximum von Mises stress in tibial cartilage plotted against number of nodes. The most chosen mesh is highlighted in red.

2.3.5.2 Comparison of models with the same loading

The Model 1 loading scenario was altered to create Model 1a. When the results of Model 1a and Model 2 were compared, it was seen that the presence of cartilage reduced the maximum contact pressure from 0.624 GPa to 0.0134 GPa as shown in the contour plots Figure 2.17. The maximum von Mises stress also reduced from 0.839 GPa to 0.083 GPa.
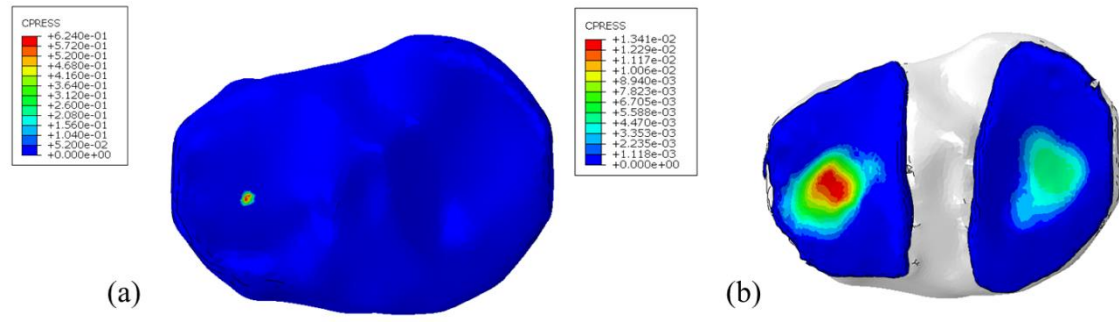
Figure 2.17: Contact pressure contour plots for (a) adjusted Model 1 and (b) Model 2.

Comparing the contact pressure contour plots in Figure 2.17, it can be seen that in the presence of cartilage not only reduces the maximum contact pressure but also increases the contact area to produce a more physiological distribution of stress in the bone.

2.3.5.3 Effect of BML elastic property

The contact pressure and von Mises stress distribution in the tibial cartilage, and the minimum principal strain in the tibia were compared for the different cases and shown in Figure 2.18.

Very little difference is seen in the distribution of contact and pressure and von Mises stress in the tibial cartilage between the cases. Looking at the minimum principal strain distribution in the tibia bone for the Hole case, it can be seen that there are lager compressive strains in the bone surrounding the hole compared to Model 2. In the stiff BML case, there is also a small change in the distribution of compressive strains in the BML region.

When comparing the minimum principal strain results, a region of interest was used to eliminate the visible boundary effect seen in Figure 2.18, caused by the application of a fixed boundary conditions to all the nodes at the bottom of the tibia.
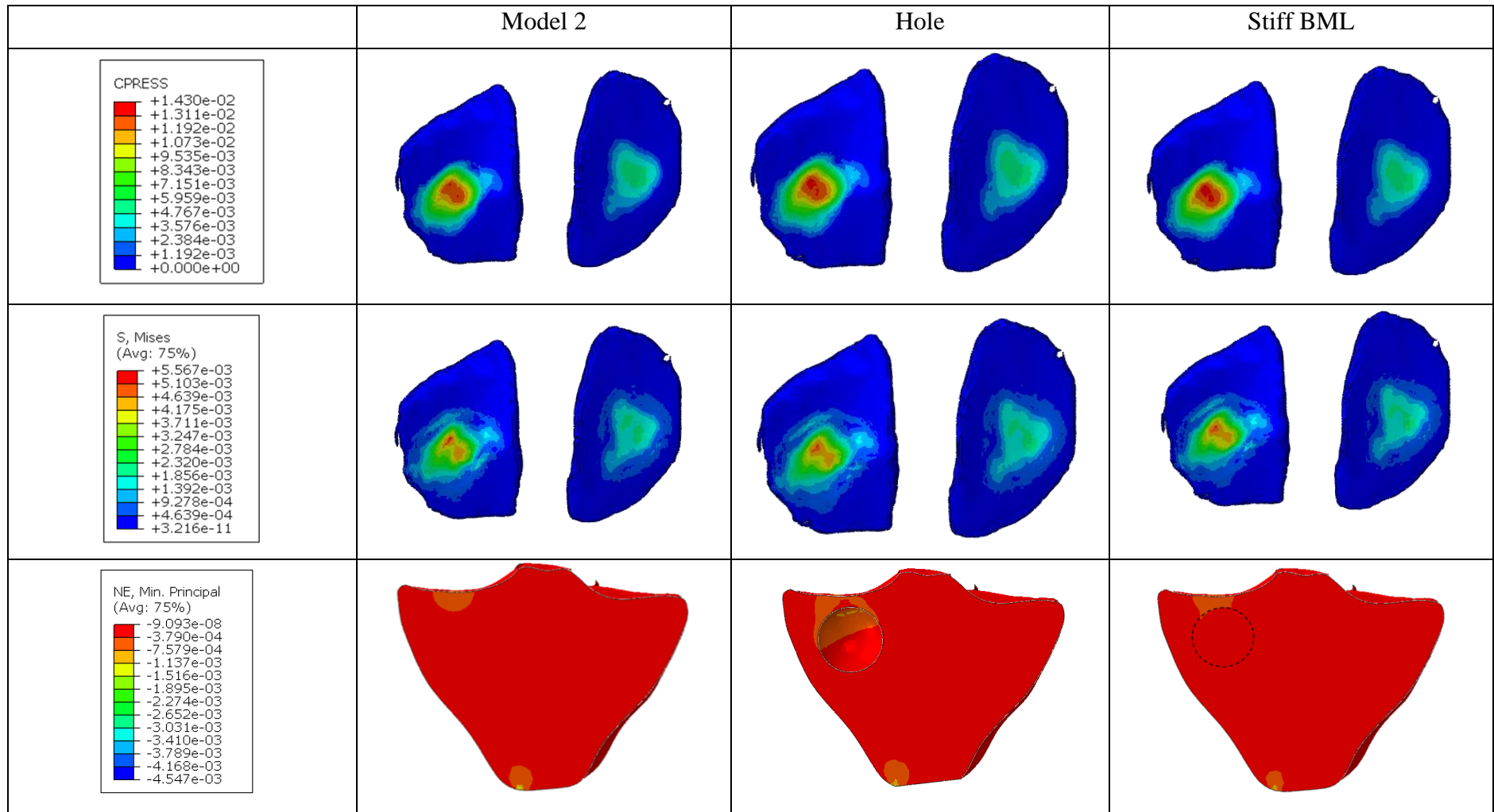
Figure 2.18: The distribution of contact pressure, von Mises stress and minimum principal strain for Model 2, Hole BML and Stiff BML cases

2.3.5.4 Effect of less stiff bone
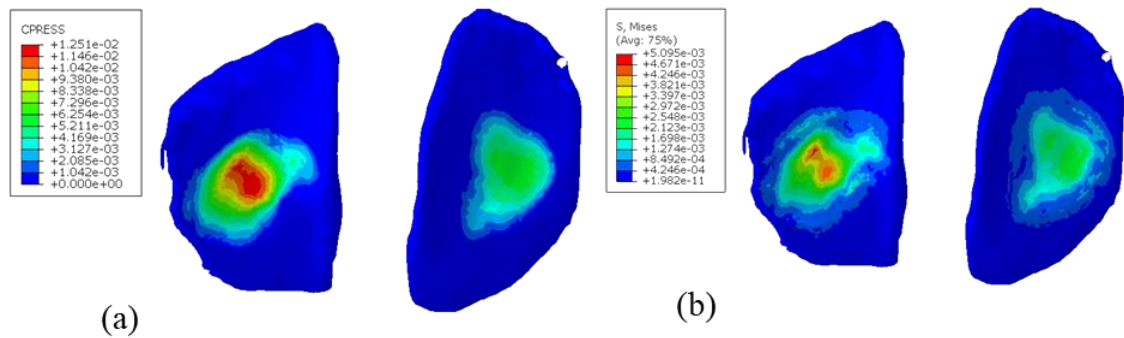
Figure 2.19: Contour plots of the tibial cartilage surfaces for the case with less stiff bone showing (a) contact pressure (b) von Mises stress.

By comparing Figure 2.18 and Figure 2.19, there is a decrease in the maximum contact pressure and maximum von Mises stress in the model with less stiff bone compared to Model 2. However, the differences are small despite the order of magnitude difference in the elastic modulus of bone in the two models. Also, there is an 8% difference between the maximum von Mises stress in the bone between the two cases, although the distribution of the stress in the bone is identical. There is also an order of magnitude difference between the minimum compressive strains in the tibia, although the distribution of the strains is identical and the strains remain less than 1%.

2.3.6 Discussion of Model 2

Comparing the results from Model 1a and Model 2, shown in Figure 2.17, the presence of cartilage led to a wider distribution of contact pressure and von Mises stress in the surface of the cartilage leading to a more physiological distribution of stress in the bone. However, while the contact area and contact pressure might have changed in the cartilage models, the trends with BML sizes and location most likely remain although less pronounced due to the less localized stress distribution in the surrounding bone.

The results of the parametric study of BML material property using Model 2 show small differences between the output parameters for the different cases because of the presence of cartilage. The contact pressure and stress are less localized than Model 1 so the changes due to the material property of the BML is less pronounced. In the BML modelled in this study is located 2 mm below the surface of the tibia, therefore there is a small area of bone above the BML with the same properties as unaffected 'healthy' bone. According to Compagnoni et al [68], these can be classified as distal BMLs. The results of this study suggest that distal BMLs may not have the most significant mechanical effects. It would be useful to consider other shapes of BMLs which extend to the tibia surface like the articular BMLs in the Compagnoni classification.

A reduction in the elastic modulus of the bone did not have a substantial effect on the contact pressure and von Mises stress distribution in the tibial cartilage or the distribution of compressive strains in the tibia. The inclusion of cartilage in the model had a much bigger effect on the contact parameters than the material property of the bone. While changing the elastic modulus of the whole bone did not have much of an effect, this is still a simplification to real bone which has a varying density (and hence material properties) from location to location.

2.4 Model 3: Model with cartilage and a hemispherical BML:

The BML classification systems described in Section 1.3.2.3 of the literature review classify BMLs according to their size, however the results from the parametric study on Model 1 in Section 2.2.5.4 show that the location of the BML plays an important role in how it impacts knee joint mechanics.

Based on the topographical classification system described by Compagnoni et al [68], discussed in Section 1.3.2.3, the BMLs modelled in Model 1 and 2 are most like distal BMLs. The purpose of this study was to investigate a different type of BML, the articular BML which are more likely to disrupt the joint contact mechanics.

2.4.1 Model Development

Finite element models were created to incorporate an 8 mm radius hemispherical BML to represent an articular BML shown in Figure 1.6a. the BML was located right at the centre of contact and tibial surface as shown in Figure 2.20.
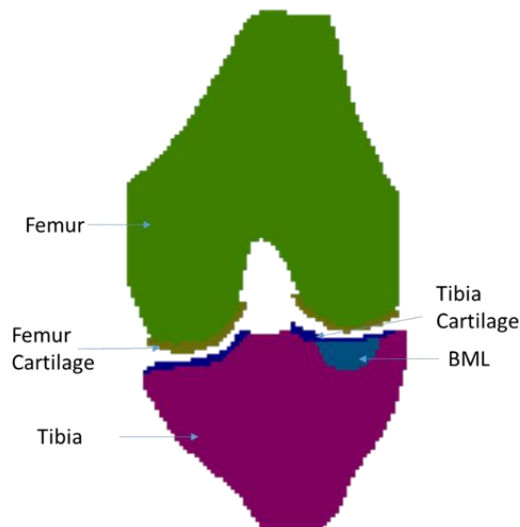
Figure 2.20: A schematic representation of Model 3 showing the bones, corresponding cartilage, and a hemispherical BML.

A sensitivity study was undertaken in which the BML region was represented in different ways:

1. BML modelled as a hole.
2. BML modelled with elastic modulus of 5 MPa.
3. BML modelled with elastic modulus of 10 MPa
4. BML modelled with elastic modulus of 1 GPa
5. BML modelled with elastic modulus of 20 GPa (10 times surrounding bone).

In all cases where the BML was represented as a solid, it was assigned a Poisson's ratio of 0.3. The bones were modelled as homogenous linearly elastic isotropic material with elastic modulus of 2 GPa and a Poisson's ratio of 0.3. The cartilage was modelled as a hyperelastic neo-hookean material with the same properties as Model 2.

The element type and size, contact definition, boundary conditions and loading scenario were the same as was used in Model 2 in Section 2.3.1.

The contact pressure and von Mises stress in tibial cartilages were compared between the different cases and the minimum principal strain distribution in the tibia was also compared for all cases.

2.4.2 Results

The distribution of contact pressure and von Mises stress in the tibial cartilage for the different cases are shown in Figure 2.21 and Figure 2.22 respectively.

From Figure 2.21, it can be seen that the distribution of contact pressure in the cartilage is distinctly different in the Hole and less stiff BML cases (5 MPa and 10 MPa) compared to the Baseline and higher BML stiffness (1 GPa and 20 GPa). In the Hole and lower BML stiffness cases, there is low contact pressure in the middle of the contact patch directly overlaying the middle of the BML. The location of the maximum contact pressure shifted to the area outside the BML. This effect is most pronounced in the Hole case. The same trend is seen in the von Mises stress distribution in the cartilage shown in Figure 2.22.

A small increase is seen in the maximum contact pressure (2.6%) and maximum von Mises stress (3.4%) in the tibia cartilage between the 1 GPa and 20 GPa cases despite the large difference in the BML stiffness.

The distribution of minimum principal strain in the tibia for all cases is shown in Figure 2.23. Comparing the Baseline and Hole cases, using Scale Bar A, there is an increase in the compressive strains in the areas just surrounding the hole. The presence of the hole also caused increased compressive strains in the other compartment. Progressive decrease in the elastic modulus of the BML area led to an increase in the compressive strains in the BML areas (up to 41% strain in the 5 MPa case). Comparing the Baseline and 20 GPa cases, it can be seen that a tenfold increase in the elastic modulus in the BML led to a small increase in the minimum principal strains in the BML region but with little effect to the surrounding bone and adjacent compartment.
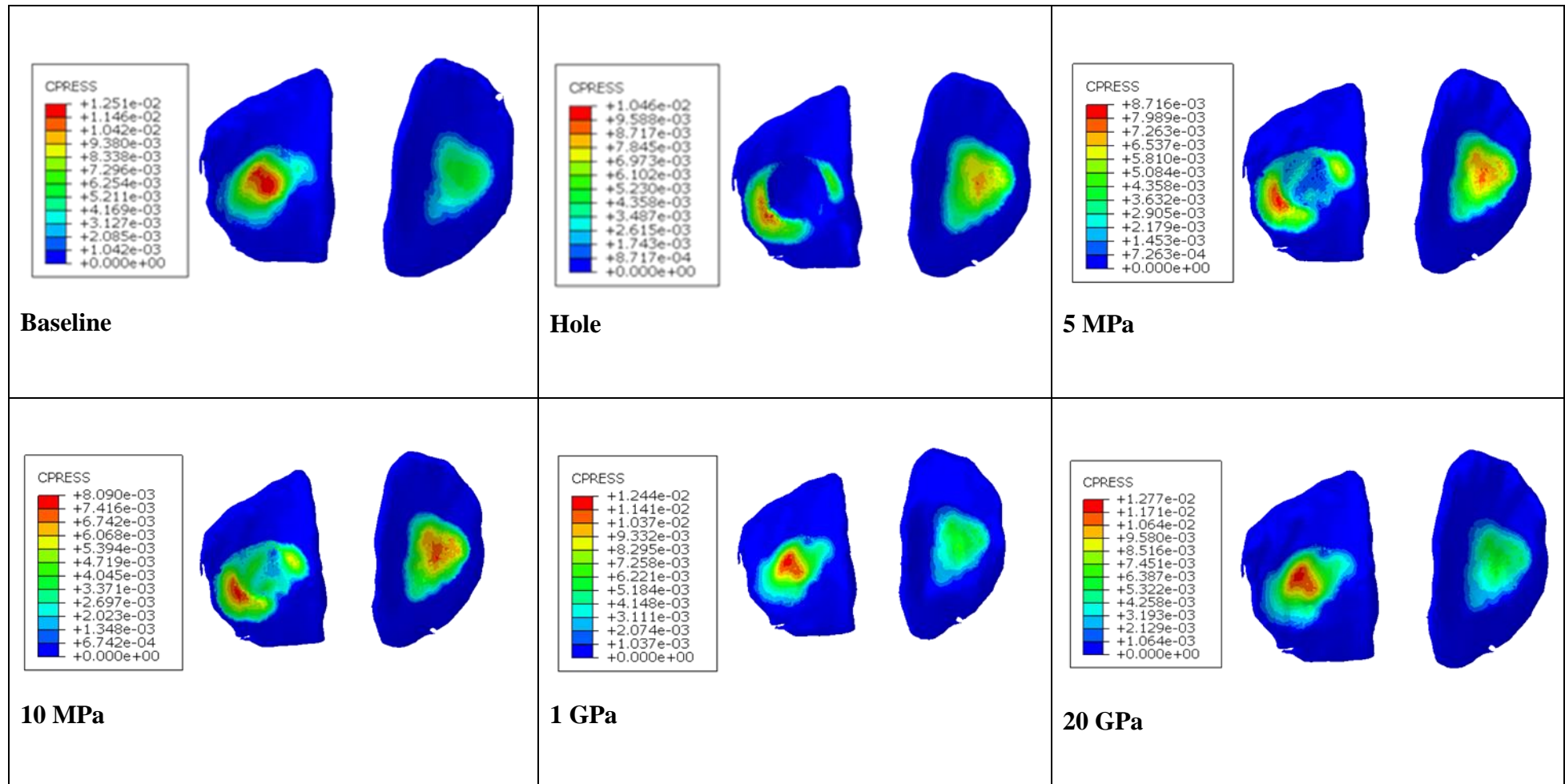
Figure 2.21: Contour plots of contact pressure distribution in the tibial cartilage for halfmoon BML cases with different elastic modulus
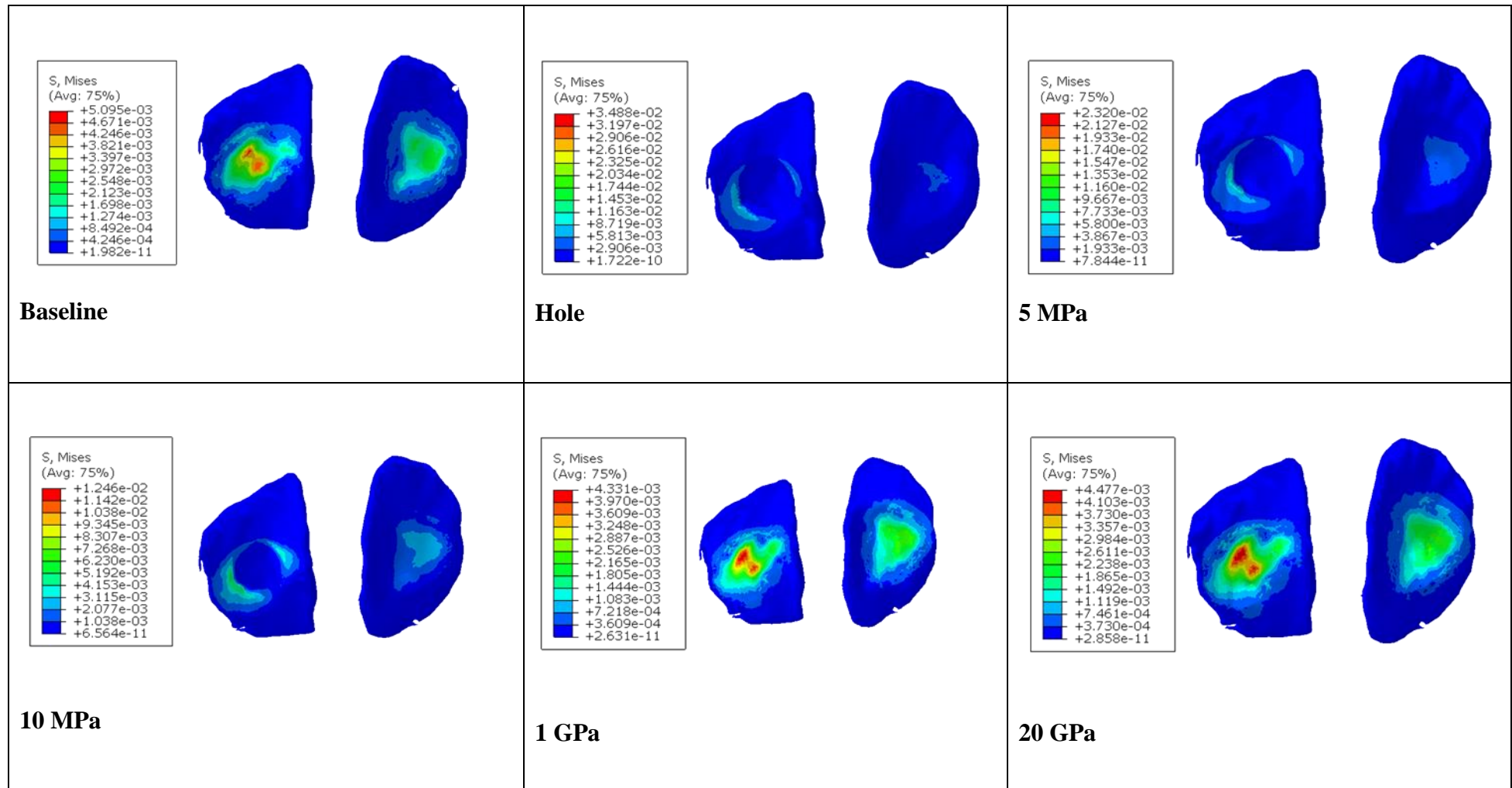
Figure 2.22 Contour plots of von Mises stress distribution in the tibial cartilage for halfmoon BML cases with different elastic modulus
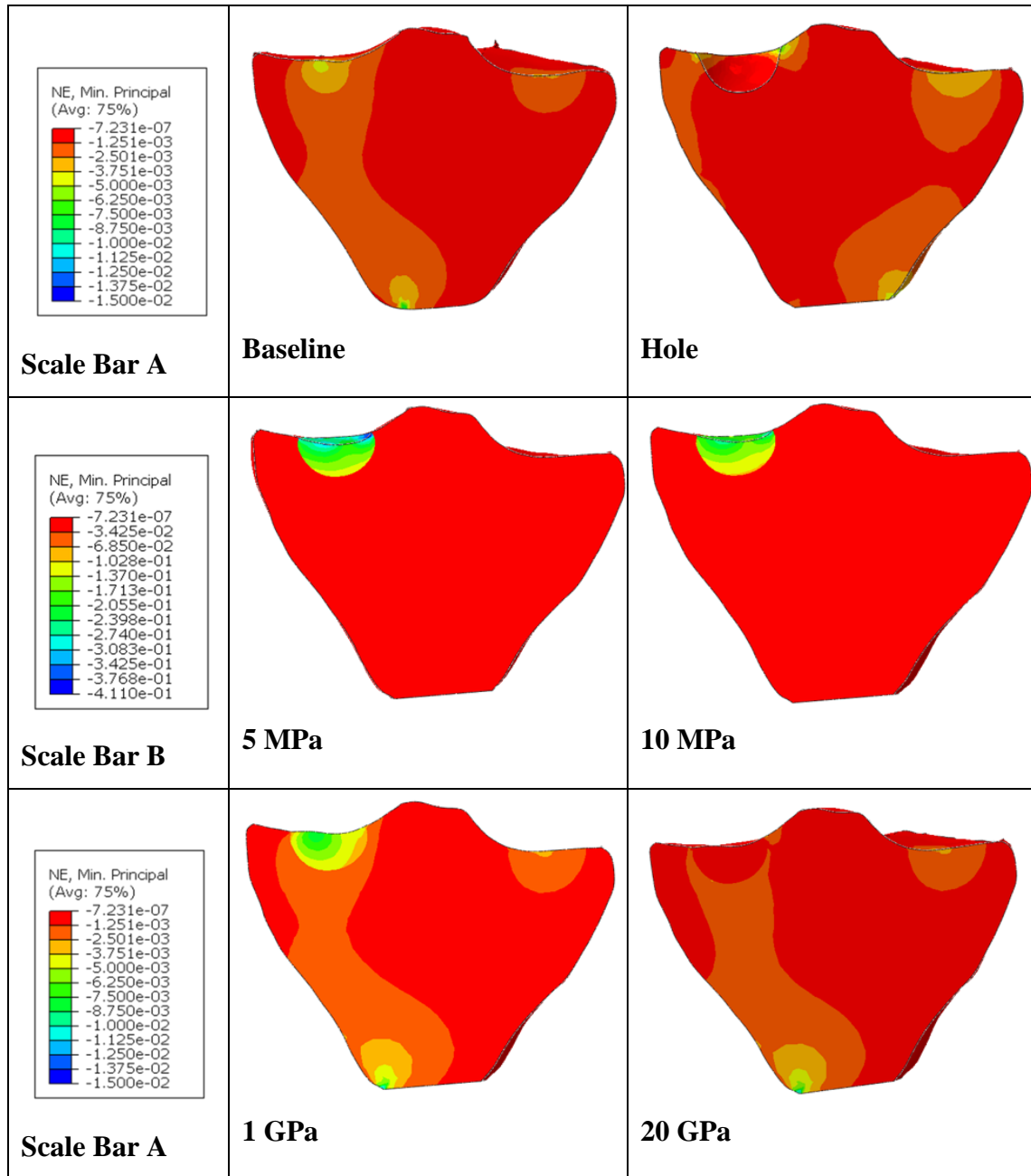
Figure 2.23: Contour plots of the minimum principal strain distribution in the tibia for halfmoon BML cases with different elastic modulus. Scale Bar is for Baseline, Hole, 1 GPa and 20 GPa cases. Scale Bar B is for 5 MPa and 10 MPa cases.

When comparing the minimum principal strain results, a region of interest was used to eliminate the visible boundary effect seen in Figure 2.23, caused by the application of a fixed boundary conditions to all the nodes at the bottom of the tibia.

2.4.3 Discussion of Model 3

In the Hole and low BML stiffness cases, the contact pressure and von Mises stress distribution in the cartilage was very different compared to the baseline and high stiffness cases as seen in Figure 2.21 and Figure 2.22 respectively. There is low contact pressure and von Mises stress in the areas of cartilage overlying the BML. Due to the low stiffness of the BML, the elements in those areas are unable to support as much load as the surrounding areas leading increasing compressive strains in the BML areas shown in Figure 2.23. An increase the elastic modulus of the BML compared to surrounding bone led to much less observable differences in the distribution of compressive strains in the tibia.

Baseline and high stiffness BMLs do not show a similar trend to the low stiffness BML cases. Increasing the stiffness of the BML from baseline to 20 GPa caused only a small increase in the maximum contact pressure and maximum von Mises stress with the distribution of contact pressure and von Mises in the tibial cartilage remaining very similar. This is consistent with results from Model 2 which show very little difference in the contact pressure and von Mises stress distribution in the tibial cartilage between a baseline model with no BML and a BML case with much higher elastic modulus than surrounding bone. The results suggest that for articular BMLs, altered loading of the knee is more likely to be seen in cases where the BML area consists of less stiff bone in comparison to the surrounding bone. For both distal and articular BMLs, very little effect is seen when the BML area consists of bone stiffer than the surrounding bone.

2.5 Overall Discussion of FE methods

The results from the parametric studies conducted in the different models in this chapter show that the size, location and material property of the BML have varying effects on the contact pressure and von Mises stress in the knee. The closer a distal BML is to the surface and the centre of contact, the bigger the effect seen on the contact pressure and von Mises stress in the tibial cartilage. Also, the biggest BMLs had the largest effect on both contact pressure and von Mises stress.

The results from Model 2 show that the presence of cartilage distributes the load over a larger area leading to a reduction in the maximum contact pressure and von Mises stress in the model. Also, the effects of the BML seen in Model 1 became less pronounced.

In Model 3, a different type of BML was considered. There results from distal BMLs in Model 2 and the articular BMLs in Model 3 show that stiffer bone in the BML area compared to surrounding bone is less likely to have an effect an effect on the joint contact mechanics compared to BML containing less stiff bone than surrounding bone. The mechanical effects of less stiff bone in BML regions to contact pressure and von Mises stress distribution in the tibial cartilage is more pronounced in articular BMLs than in distal BMLs due to the involvement of the tibia surface. articular BMLs containing less stiff bone may benefit more from augmentation than distal BMLs with less stiff bone. In this chapter, we have only considered BMLs classed as distal and articular according to Compagnoni et al [68]. Other types of BMLs may have differing effects on joint contact mechanics. It would be interesting to see clinical data on outcomes of subchondroplasty based on this topographical BML classification, but that does not currently exist most likely due to how recent this classification system is.

Results from Model 3 and Model 1 show a range of potential effects depending on the material property of the BML. The material property of the bone in BML areas is unknown and this chapter highlights the need to derive material properties for BML affected bone. The experience gained and methodology for creating finite element models using ScanIP and Abaqus will be taken forward into subsequent chapters.

Also, the use of a homogenous elastic modulus does not accurately represent the differences in material properties between less stiff trabecular bone and stiffer cortical bone. As discussed in Section 1.4.2, there are advantages to capturing the trabecular architecture using a relationship between CT image data and elastic material properties. Although there was very little effect seen in changing the elastic modulus of all the bone,

it would be useful to represent the inhomogeneities in the bone, especially when altering one region of bone to model a BML.

In summary, finite element models of the tibiofemoral joint were developed to perform parametric tests on the effects of size, shape, location and elastic modulus of BMLs on the contact pressure and von Mises stress in the joint. The results show that the size, shape, location and elastic modulus of the BML all have an effect especially when the BML region is less stiff than surrounding bone and located in the loaded regions of the joint. More information about likely material properties of bone in BML regions is required to investigate further.

The experience gained and lesson learned on how simulating a BML in a tibiofemoral joint using ScanIP and Abaqus were carried on to subsequent finite element modelling work reported in Chapter 5.

Chapter 3 : Derivation of Bone Material Properties - A Porcine Study

3.1 Introduction

This chapter describes the experimental methods developed to investigate the mechanical properties of bone marrow lesions in the knee. The aim was to develop a method of establishing greyscale-derived mechanical elastic material properties for porcine bone using a joint experimental and computational approach. This involved the use of micro computed tomography (microCT) imaging techniques, uniaxial compression testing and specimen-specific finite element models.

The method developed and discussed in this chapter was subsequently translated to bone from cadaveric human knees to determine the material properties of areas of bone affected by BMLs reported in Chapter 4.

3.2 Method

The flowchart shown in Figure 3.1 details the methods employed in this study and how the experimental and computational aspects of the method were combined. The finite element models were created based on individual specimen geometry and the material properties were derived from the image data. The elastic modulus was related to image data using the bone volume fraction method briefly described in Section 1.4.5.1. The computational results gotten from the finite element models are compared against the experimental results to give an optimized relationship between greyscale image data and elastic modulus. The bone volume fraction method was used because it has been shown to produce better agreement between computational and experimental results than a direct greyscale method [91].
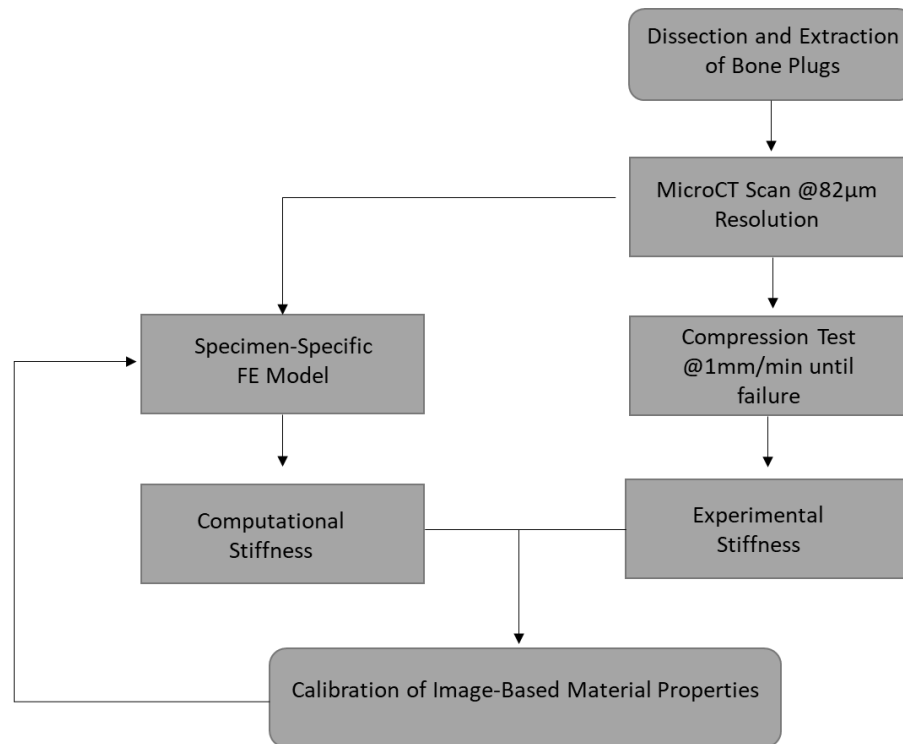
Figure 3.1: Flowchart showing the work flow of the combined experimental and computational method used to derive material properties of bone specimens

3.2.1 Specimen characteristics and preparation.

Three right hind porcine legs were procured from a local abattoir (J. Penny and Sons, Leeds, UK) as a by-product of the food supply chain. The pigs are slaughtered at approximately six months of age.

The legs were dissected and osteochondral plugs were extracted from the femurs using an 8.5 mm diameter surgical corer (Acufex, Smith and Nephew, MA, USA) and a mallet. One plug was taken from the centre of each femoral condyle; these are the flattest areas and were selected to aid the extraction of straight osteochondral plugs with perpendicular ends. The cartilage layer was removed from the bone plugs using a surgical blade and the bone plugs were trimmed to a height of 10 mm using a small bone saw, leaving the subchondral plate intact. Each bone plug was filed to ensure it had flat ends. A length of 10mm was selected because it was found to be difficult to consistently obtain longer bone plugs due to the presence of the growth plate in the skeletally immature porcine legs as shown in Figure 3.2(b).
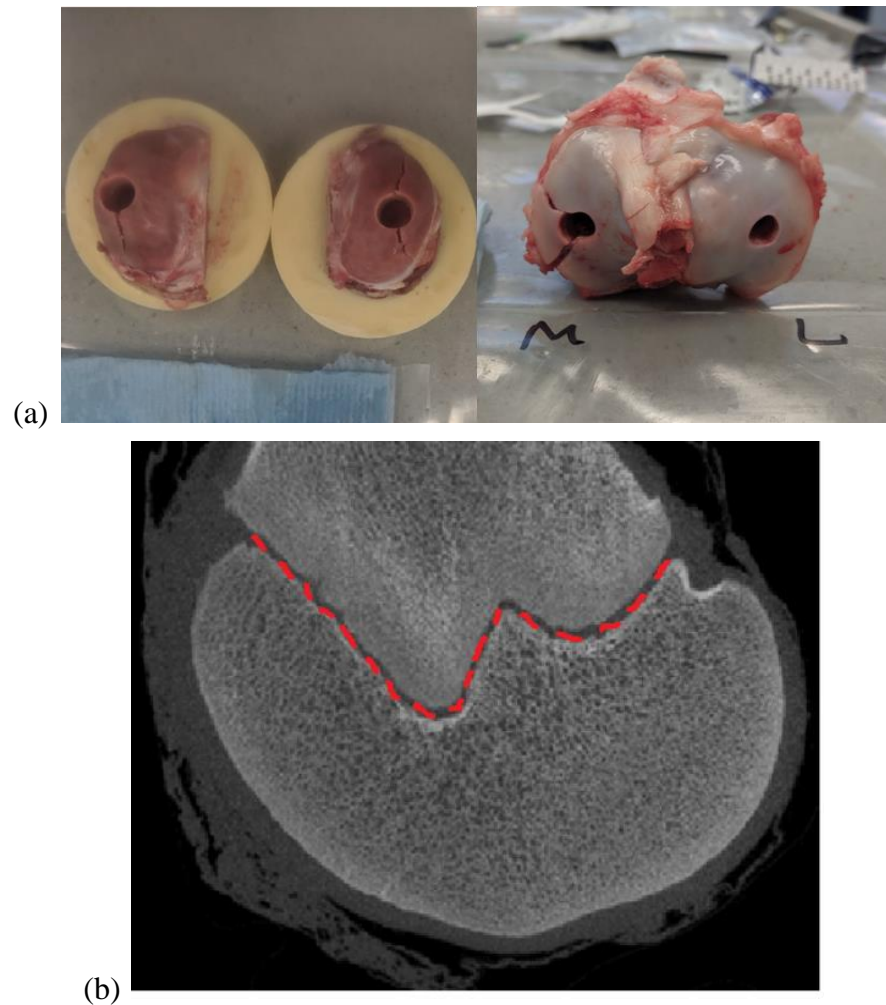
Figure 3.2: (a) location of bone plugs on femoral condyle and tibial plateau. (b) Example CT image of femur showing growth plate (red dashed line).

Bone plugs were also taken from the centre of the tibial plateau of each leg using a 6.5mm diameter surgical corer following the same process. This was done to investigate the possible effect of different aspect ratios of bone plugs. Each bone specimen was wrapped in phosphate buffered saline (PBS) soaked paper towel, to prevent drying of the bone plugs, and stored in a refrigerator at 4°C until further testing.

3.2.2 Micro-CT Imaging

Conventional radiographs are created when x-rays pass through the body to project an image of the body with its internal organs, skeleton and air spaces onto a sheet film. A major limitation with this technique is that 3D objects are projected onto a 2D plane, hence depth information is lost. In computed tomography however, the X ray source and detection plate are simultaneously moved such that many projections are taken in different planes, these projections can then be reconstructed into a 3D representation of the object [122].

Typical clinical CT images have resolutions between 500μm - 2000μm which is insufficient to capture trabecular architecture, as the trabeculae can be smaller than 150μm in diameter [26]. Micro-CT however can provide images with much higher resolution, in some cases down to single micrometre level. Micro-CT imaging is therefore able to provide non-destructive, high-resolution information on hard tissues.

Micro-CT scans of bone plugs were captured using a high resolution peripheral quantitative computed tomography (HR-pQCT), (XtremeCT, Scanco Medical AG, Switzerland). The bone plugs were kept in individual compartments of a plastic bag to maintain hydration and scanned together. Consistent scanner settings (Table 3.1) were used throughout all the imaging and the scanner calibration was checked weekly.

Table 3.1: MicroCT Scanner Settings

Voxel size	Current	Energy	Exposure
82 µm	900 mA	60 kVp	300 ms

The images produced were exported in the standard DICOM format.

3.2.3 Compression Testing

The bone plugs were press fit into cylindrical Delrin endcaps which contained a circular recess of depth 0.5 mm and diameter of either 8.5 mm (for femoral specimens) or 6.5 mm (for tibial specimens). Each specimen was tested under axial compression in a material testing machine (Instron 3365 with 1 kN load cell, Instron Ltd, UK), as shown in Figure 3.3. Each sample was tested with 5 pre-load cycles of 50 N at a displacement rate of 1mm/ min to ensure the bone embedded into the endcaps properly. A final compressive force was then applied at a displacement rate of 1mm/min until the ultimate compressive strength was exceeded. This was indicated by a consistent downward turn of the load-displacement graph after the peak. Load- displacement data was recorded for each sample.
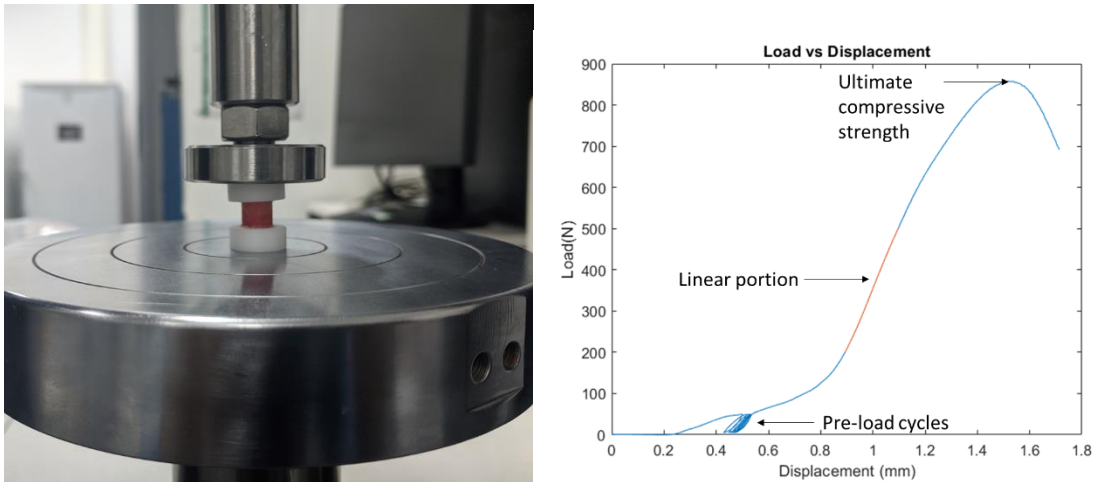
Figure 3.3: (left to right) experimental set up showing bone plug and endcaps in compression. Example load/displacement curve showing pre-load cycles, linear portion and location of ultimate compressive strength.

For each bone plug, the stiffness was calculated from the load-displacement graph using a custom script (MATLAB R2018a, The Mathworks Inc, Natick, MA, USA). The gradient was found by fitting a linear polynomial to the line between 200 N < load ≤ 400 N, which was found to be the most linear portion of the load-displacement graph for all the bone plugs as shown in Figure 3.3.

3.2.4 Finite Element Modelling

In this section, the development of a baseline finite element model is first described, followed by a description of the optimisation process used to derive the bone material properties, and finally a series of sensitivity tests where individual parameters were varied to assess their effect.

Image to model process

DICOM images from the µCT scans were imported into Simpleware ScanIP v.2017 (Synopsys, Mountain View, CA, USA) where the 3D images for each bone plug were cropped and processed. The images were then down-sampled from 82 µm to 164 µm for ease of manipulation and to reduce the processing time and computational cost.

For each bone plug, the images were adjusted and aligned in the x-y direction to correct for any tilting during scanning and to ensure that all bone plugs were aligned in the same direction. A mask was created to capture the full specimen geometry (Figure 3.4(b)). A consistent lower threshold (900 HU, range 0 – 2564 HU) for the voxel intensity value, determined by iterative visual comparison between different specimens, was applied to

images to segment the trabecular architecture alone (Figure 3.4(c)). The image containing the trabecular architecture (bone volume mask) was binarized, exported and re-imported as a background for the total volume mask (Figure 3.4(e)), this enabled the subsequent assignment of properties to the FE models to be proportional to the bone volume fraction in the given element region. Therefore, each voxel of the total volume mask is assigned a greyscale value proportional to the bone volume fraction of the area captured by that voxel.
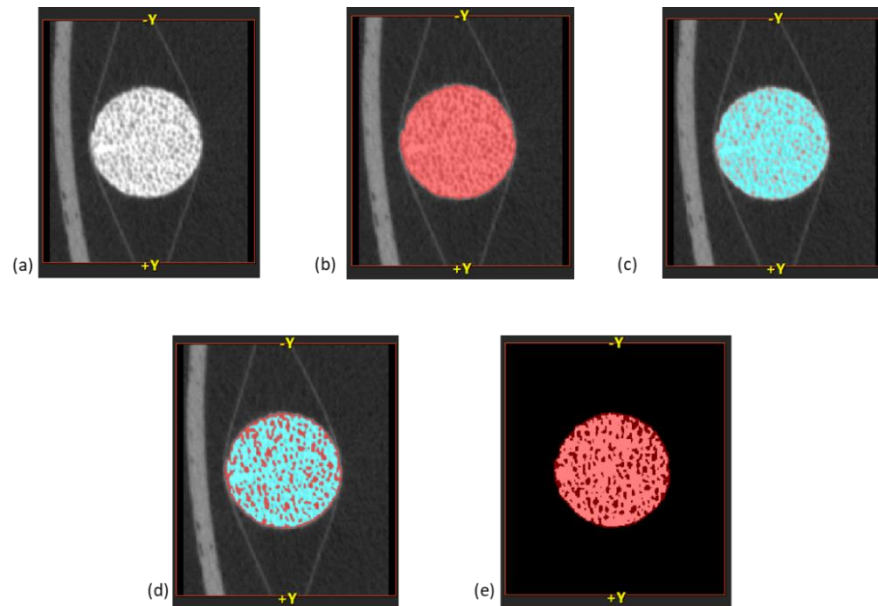
Figure 3.4: (a) greyscale image of bone plug; (b) greyscale image of bone plug with the whole plug highlighted (total volume); (c) greyscale image of bone plug with highlighted trabecular architecture (bone volume); (d) bone volume and total volume overlaid; (e) total volume mask with bone volume as new background.

The surface geometry of the endcaps used in the experimental testing were imported into ScanIP. Using the position and orientation tool, the endcaps were positioned above and below the bone plugs as in the experimental set-up. The endcap surfaces were then converted to masks. Using the Boolean tool, the intersection between bone and endcaps were converted to endcap, this was done to ensure a flat and consistent contact between bone and Delrin endcaps as shown in Figure 3.5.
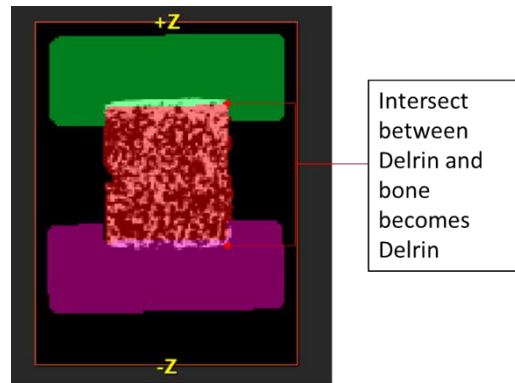
Figure 3.5: Trimming of bone plugs to create consistent flat contact between bone and Delrin endcaps.

Material properties

Isotropic elastic material properties were applied for the endcaps according to the manufacturer's information for Delrin (Young's Modulus = 3.3 GPa, Poisson's ratio = 0.3). Greyscale-based material properties were applied for the bone with 255 steps based on 8-bit resampled image with a 1-to-1 conversion factor (i.e., 0 where there was no bone and 255 where the element was completely bone tissue) such that:

$$Young's\ Modulus_{bone\ element} = Conversion\ factor\ (\alpha) \times BV/TV$$

Equation 3.1

and,

$$BV/TV = Greyscale_{bone\ element}/255$$

Equation 3.2

The conversion factor was calibrated to give the best agreement between FE model and experiments through an iterative process.

The FE model was imported into Abaqus CAE v.2017 (Dassault Systemes, Velizy-Villacoublay, France).

Mesh generation

The bone modulus optimization method, compares computational stiffness from the FE model to the experimental stiffness value. An inappropriate mesh may overestimate or underestimate the computational stiffness in the FE model. The error due to the mesh is then carried on to the bone modulus optimization. To minimize the error due to the mesh, a mesh sensitivity study was carried out on one bone plug and the effect of the mesh on the computational stiffness and subsequent bone modulus conversion factor was investigated. Ideally, the effect of the mesh would be investigated using all the bone plugs bone plugs as the point of interest is the conversion factor for the group not individual bone plugs but bone modulus optimization is a lengthy process even for one bone plug. The result from one bone plug is useful to minimize the error in the computational stiffness due to the mesh even if the effect on the resultant group conversion factor is not investigated.

Cases were created by varying the element edge length from 2 mm to 0.4 mm with an approximate halving of element edge length between cases. The details of the cases tested in the mesh sensitivity test are presented in Table 3.2

Table 3.2: Details of mesh sensitivity test cases

Target minimum element edge length (mm)	Number of elements
2.0	2788
1.0	19306
0.7	21214
0.4	32326

Based on the mesh sensitivity test, models were meshed using quadratic tetrahedral elements (C3D10 in ABAQUS) of target edge length of 0.7 mm for the bone, which was also used by Day et al in a body of work to establish a relationship between CT image data and elastic modulus using a similar bone volume fraction method [78]. The endcaps were modelled using the same type of elements with a target edge length of 0.35 mm.

Interactions and boundary conditions

Apart from the mesh, errors between computational and experimental results can be due to FE model not accurately representing the experimental set up. The frictional interaction between the bone plugs and Delrin endcaps is difficult to measure experimentally however, it is important that the computational model adequately captures the interaction between the bone plug and Delrin endcaps. Therefore, another sensitivity test was carried out on one plug to investigate the effect of the frictional interaction properties between bone plug and endcaps on the computational stiffness output from the model.

The following cases were tested:

- Frictionless interaction between bone plug and endcaps
- Friction coefficient of 0.1 between bone plug and endcaps
- Friction coefficient 0.2 between bone plug and endcaps
- Tied interaction between bone plug and endcaps

Following the sensitivity test, Node-to-Surface contact interactions with small sliding were created between the bone plug and the endcaps with the bone plug as the master surface. A friction coefficient of 0.1 was applied and a penalty overclosure method was used to define the normal behaviour of the contact.

The bottom endcap was constrained for translation and rotation in all directions to replicate the experimental set-up. In the experimental set up, the endcap is constrained from sliding by the friction between the endcap and the stainless-steel fixture as shown in Figure 3.3. Downward axial displacement of 0.5 mm was applied to the top endcap using a reference point coupled to nodes at the top surface of the top endcap. Displacement was constrained in all the other directions, effectively acting as extra boundary conditions to prevent the upper endcap from other translation or rotational motions, matching the experimental set-up.

3.2.5   Bone Modulus Optimization

Elastic material properties for the bone tissue were derived from the average greyscale value for each bone element (and hence to the BV/TV as explained in Section 3.2.4) based on a conversion factor. A golden section search optimisation process using the Brent method within the opti4Abq toolbox [123] was used to calibrate the conversion factor, α.

The opti4Abq toolbox makes use of specimen-specific finite element models created in Section 3.2.4 and corresponding experimental stiffness values calculated from the

experimental load-displacement graphs in Section 3.2.3 to produce a conversion factor with a minimised root means square error. Within the toolbox, the following user set parameters were assigned: the minimum and maximum values allowed for the conversion factor: 0.1 MPa, 100 MPa, the maximum number of iterations the optimisation can take: 40, the tolerances for the function being minimised: 10% and for the gradient: 1e-05. The optimisation is done in an iterative root-finding process starting with an inputted initial value. The output of the toolbox is the optimised conversion factor and corresponding root mean square error between the computational and experimental results.

The optimisation was carried out on all the bone plugs (pooled), as well as separately on one set containing bone plugs taken from femoral condyles (8.5 mm diameter) and another set containing bone plugs taken from tibial plateaus (6.5 mm diameter).

3.3 Results

3.3.1 Sensitivity tests

The results of the mesh sensitivity test are presented in Figure 3.6. It shows that halving the element edge length from 2 mm (~ 2800 elements) to 1 mm (~19000 elements) led to a 0.9% difference in the computational stiffness and a 1.1% difference in the conversion factor between experimental and computational stiffness. A further approximate halving of the element edge length from 1 mm (~ 19000 elements) to 0.4 mm (~ 32000 elements) shows a 0.3% difference in the computational stiffness and a resultant 0.5% difference in the conversion factor. It can be seen that the percentage difference in the outputs between cases is reducing as the element edge length is halved. This shows that mesh is converging.

There is only a small difference between the computational stiffness (0.08% difference) and conversion factor (0.1% difference) results between the mesh with element edge length of 0.4 mm and the mesh with 0.7 mm element edge length. Given that the optimization process takes approximately 30 minutes to complete for one bone plug, the additional computational cost of using elements with edge length 0.4 mm over elements with edge length 0.7 mm is not justified. Therefore, the mesh with element edge length of 0.7 mm and ~21000 elements was selected.
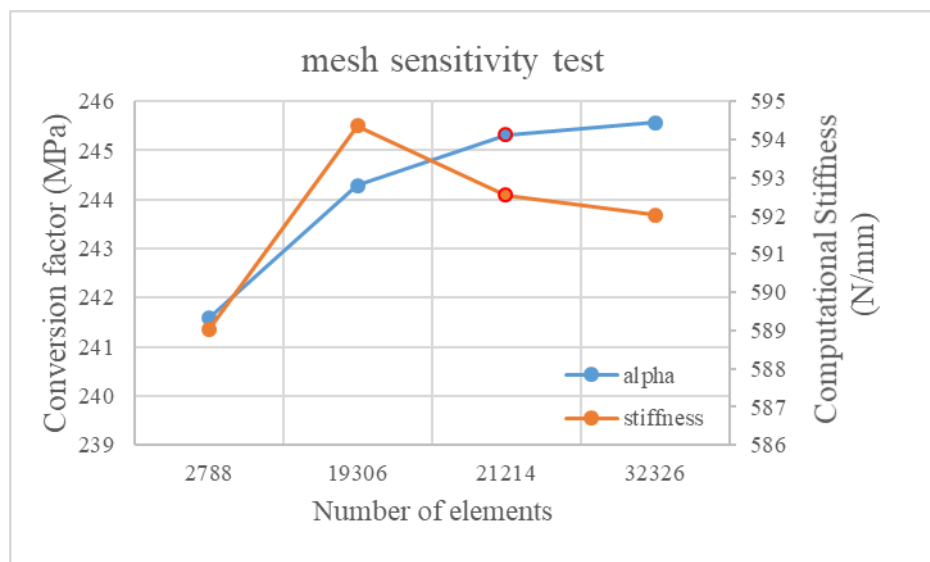
Figure 3.6: Graph showing the sensitivity of the computational stiffness and optimized conversion factor to changes in the number of elements for one model. The chosen mesh is highlighted in red

From the friction sensitivity test results presented in Table 3.3, it can be seen that the computational stiffness increased from frictionless to tied interaction properties. The biggest difference was seen between frictionless and tied interactions (7.7%). This shows that using a different friction interaction in the models would give different stiffness values and potentially different optimized conversion factor between experimental and computational models.

Table 3.3: Results for sensitivity to friction interaction

Interaction	Computational Stiffness (N/mm)	% Difference (compared to frictionless)
frictionless	583.6	
friction coefficient 0.1	588.6	0.8
friction coefficient 0.2	592.0	1.4
bone tied to endcap	628.6	7.7

3.3.2 Bone Modulus Optimization

The optimized values of the conversion factor (α), resulting RMS errors and the numbers of iterations required are shown in Table 3.4. An optimized conversion factor was found for the bone plugs after 16 iterations but due to the high overall error, the tibial and femoral models were separately optimized. The results showed different conversion factors for the 8.5 mm diameter bone plugs taken from the femur and the 6.5 mm diameter bone plugs taken from the tibia with a lower root means square error between the computational and experimental stiffness in the femur bone plug set compared to the tibia bone plug set.

Table 3.4: Optimized conversion factors with associated RMS errors for different sets of bone plugs.

	Conversion Factor α (MPa)	RMS Error (%)	Iterations
All plugs	297.6	41	16
Femur (8.5 mm ø)	502.6	15.9	9
Tibia (6.5 mm ø)	241.5	33.5	7

The relationship between the stiffness derived from experiments and the corresponding values from the computational models following optimization for all bone plugs, femoral and tibial plugs are shown in Figure 3.7, Figure 3.8 and Figure 3.9 respectively.
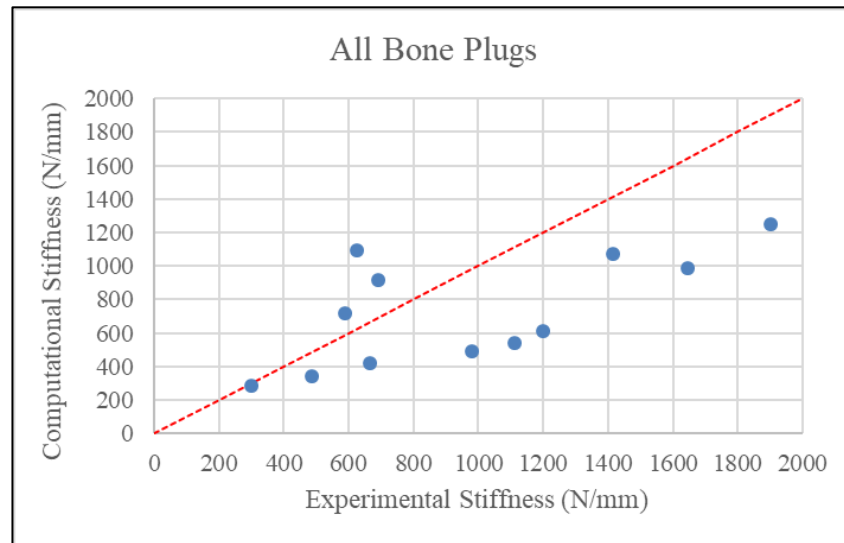
Figure 3.7: Experimental stiffness plotted against computational stiffness for all bone plugs following optimisation of the conversion factor α. The red dotted line represents a perfect agreement.
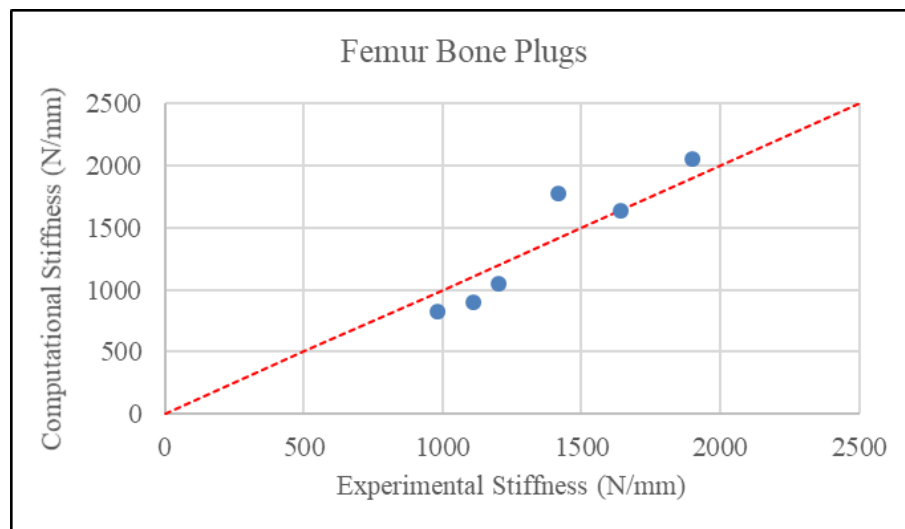
Figure 3.8: Experimental stiffness plotted against computational stiffness for femur bone plugs following optimisation of the conversion factor α. The red dotted line represents a perfect agreement.
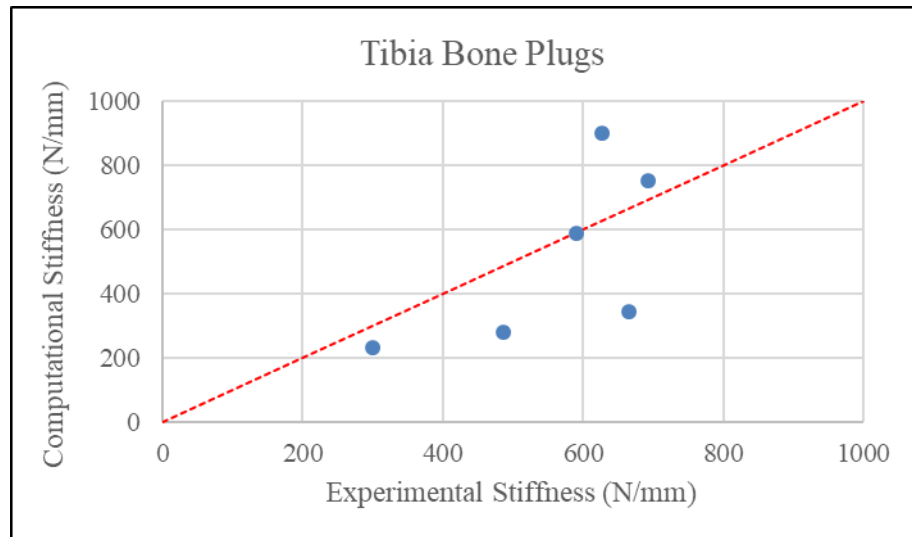
Figure 3.9: Experimental stiffness plotted against computational stiffness for tibia bone plugs following optimisation of the conversion factor α. The red dotted line represents a perfect agreement.

Looking at the experimental stiffness values for femur bone plugs shown in Figure 3.8, it can be seen that there is a wide range of experimental stiffness values within the group (~ 1000 N/mm – 2000 N/mm). The range of experimental stiffness values for the Tibia bone plugs, shown Figure 3.9, is smaller (~ 200 N/mm -700 N/mm). The bone plugs taken from the tibia are less stiff than those taken from the femur. This is intuitive given that the bone plugs taken from the tibia are thinner than those taken from the femur.

From Figure 3.9, it can also be seen that the computational models seem to underestimate the stiffness of the bone plugs, as 3 out of 6 data points lie below the line of perfect agreement.

3.4 Discussion

There have been numerous studies on the derivation of tissue level elastic properties of bone. In many cases, experimental tests have been used in combination with high-resolution subject specific FE models derived from micro-CT images to increase the accuracy of the results [124]. This chapter establishes a method for defining a relationship between element bone volume fraction and elastic modulus for using simple compression tests and subject-specific CT image-based FE models. The results of this study are discussed here.

Mesh sensitivity

From the mesh sensitivity results shown in Figure 3.6, a trend towards convergence can be seen in the computational stiffness and optimized conversion factor as the number of elements in the mesh increase. A 52% increase in the number of elements from ~21000 to ~32000 led to only a 0.1% increase in the conversion factor. While the computational time for running at the finest mesh was only 30 minutes, this was for optimizing one plug only. The optimization process for all the bone plugs took over 48 hours to complete using the mesh with element edge length 0.7 mm and ~21000 elements, a much longer runtime would be expected for the finest mesh (element edge length 0.7 mm and ~32000 elements). Therefore, it was concluded that the mesh with ~21000 elements (target element edge length = 0.7 mm) had minimal errors due to the mesh and will be used in the subsequent chapters.

The imaging sequence and settings used in this study have been used successfully by other researchers in the group for both large animal and human bone tissue. The images produced have been shown to be of sufficient resolution for building finite element models in general and also specifically for greyscale optimization [91, 112, 125-127].

Modelling interaction properties

In many studies, compression tests have been carried out with the specimen placed between two flat steel plates which have been associated with structural end effects [128] causing relatively high localised deformations where the specimen interfaces with the plates. Structural end effects have been minimized by using end caps. Jacobs et al [129], showed statistically significant reduction in error between FE predicted Young's Modulus and experimentally measured values with endcaps compared to specimens without endcaps. The endcaps were glued to the specimen in the experimental setup. The interaction between the specimen and the endcap was modelled using a tied interaction in

the FE models, assuming perfect bonding between the specimen and endcaps. In this chapter, the specimen was press fit into a 0.5 mm recess in the endcap and was modelled with an assumed friction coefficient of 0.1. The results from the friction sensitivity tests showed only a 7.7% difference in the computational stiffness reported using frictionless and tied interaction properties. A 0.8% difference was seen between frictionless and a friction coefficient of 0.1. The overall contribution of friction interaction properties to the computational stiffness is estimated to be between 1% and 8%.

The output compared in the friction sensitivity test was computational stiffness which is different from the primary output of interest in this chapter (conversion factor). However, the conversion factor is dependent on the FE model's boundary conditions, mesh and interaction properties therefore any changes which affect the computational stiffness in the FE models will have similar effect on the conversion factor.

A study investigating bone-implant interface in total hip replacements, showed that agreement between FE models predicted micro-motion and experimental values was based on a combination of the coefficient of friction and the contact element type [130]. In cases with node-to-face elements, a friction coefficient of 0.1 gave the best agreement between FE and experimental results. This study uses node-to-surface contact elements which is the Abaqus equivalent of node-to-face, therefore the interaction properties used in the FE models are reasonable and fitting and will be carried forward to the human bone tissue work.

Bone Modulus Optimization

In this study, an RMS error of 44.7% was found between the optimised computational stiffness and experimental stiffness for all the bone plugs. When the bone plugs were separated according to size of bone plug (8.5 mm diameter taken from the femur vs 6.5mm diameter taken from the tibia), different conversion factors were found for each group and the RMS error improved for both groups compared to the pooled case. Better agreement between computational and experimental stiffness (RMS error 15.9%) was achieved with the bone plugs taken from the femur using an 8.5 mm diameter surgical corer. The RMS error for bone plugs taken from the tibia using a 6.5mm diameter surgical corer was 33.5%.

The 8.5 mm bone plugs taken from the femur had an aspect ratio of 1.2:1 while the 6.5 mm bone plugs from the tibia had an average aspect ratio of 1.5:1. In a study investigating the role of specimen geometry on trabecular modulus and strength [131],

Keaveney et al found excellent correlations between apparent density and modulus, and, apparent density and strength using 2:1 aspect ratio cylinders in uniaxial compression tests. The authors suggested a 2:1 aspect ratio cylinder be used as the standard specimen in uniaxial compression testing of trabecular bone. A more recent study [132] comparing cylindrical porcine trabecular of different aspect ratios (1:1, 2:1 and 3:1) also found higher coefficients of determination for both density-modulus and density-strength for 2:1 aspect ratio cylinders. Therefore, the 6.5 mm diameter bone plugs would be expected to show better agreement to with experimental results after optimization. However, although 2:1 cylinder is the suggested specimen standard for experimental compressive testing, these studies do not take into account the trabecular architecture. Trabecular bone is made up of connected struts of individual trabeculae which contribute to its strength. Interruptions to these connections will reduce specimen stiffness and load-bearing capacity. Bone plugs with a 6.5 mm diameter have less total volume and therefore less connected trabeculae compared to an 8.5 mm diameter bone plug of the same length. So, while the unconnected regions may have high greyscale intensity, they are not able to bear as much load because they are not connected to other trabeculae and this may account for the variation in the error between computational and experimental stiffness for the two groups.

Another likely contributor to the differences between the two groups is anatomic location. Inter-site differences in trabecular bone architecture and tissue modulus have been well documented in literature [37, 93, 133], this may mean that different CT greyscale-stiffness relationships need to be established for different anatomical sites. A study by Morgan et al showed different apparent density-elastic modulus relationships for bone from different anatomical sites (vertebra, proximal tibia, greater trochanter, femoral head) [93]. Results from the study showed that ignoring anatomical site-dependence led to errors in predicted modulus of up to 60%. This suggests that differences in anatomic site could have a large effect on the agreement between computational and experimental results and justifies the derivation of different CT greyscale-elastic modulus conversion factors for the two groups of bone plugs.

Limitations

Due to the manual nature of the bone plug extraction, it was important to keep the surgical corer straight throughout the extraction process to avoid having bone plugs with non-perpendicular ends and sides. These imperfectly shaped bone plugs would result in changes in the angle of loading within the bone plugs. An alternative to the manual surgical corer and mallet method could be using a motorised drill but this could lead to damage to the trabeculae around the bone plug edges due to high shear. However, because subject-specific finite element models were created from CT images of individual bone plugs, any bend in the plug is captured in the FE model. Any altered loading of the bone plug is also replicated in the FE model by ensuring that all bone plugs are aligned in the x-y axis.

Another potential source of error between the in-silico and in-vitro models may be the trimming of the bone plugs in ScanIP to create a flat surface to interface the endcaps. This was done to achieve good contact between the bone plugs and the endcaps. However, in the experimental setup, the plugs were press fit into the endcaps and five preload cycles were applied which would have a similar effect of creating good contact between the bone plug and endcaps.

This study could have been extended by including a separate validation set however, the aim of this study which was to develop a method for deriving bone properties which can be translated to human cadaveric bone, were met without the validation set.

To conclude, a method was described for characterizing the elastic material properties of bone plugs using a combination of experimental stiffness results from uniaxial compression tests and specimen-specific image-based FE models. The optimization of the relationship between bone volume fraction and Young's modulus was also described. The methods developed in this chapter was applied to bone plugs taken from non-BML and BML regions of cadaveric human patella and reported in Chapter 4.

Chapter 4 : Characterization of material properties of bone in BML and non-BML areas using human bone tissue

4.1 Introduction

Bone marrow lesions are a form of subchondral bone damage associated with osteoarthritis. As discussed in Section 1.3.2.3, a small number of histological studies and several clinical studies have been carried out to investigate BMLs and their association with pain and osteoarthritis progression. However, no studies have investigated how the elastic mechanical properties of bone in BML areas might differ from surrounding unaffected bone.

The work presented in this chapter aims to fill a gap in the literature by providing important information on the mechanical properties of bone in BML areas and how it might differ from bone in unaffected areas. This will also aid a more accurate representation of BMLs in finite element models.

The method developed in the porcine pilot study was applied to human bone specimens in this chapter. Due to the limited supply of human femur and tibia tissue with substantial areas of BMLs and the prevalence of BMLs found in harvested cadaveric patellae, the method of extracting bone plugs described in Chapter 3.2 was adapted for patellae. As discussed in Section 1.3.4, BMLs commonly occur in patellae as well as the femur and tibia, and have been treated using subchondroplasty in the same way as BMLs found in the femur and tibia. Therefore, the available patellae with BMLs were used in this study.

In this study, CT greyscale-Young's modulus relationships were derived for bone in BML and non-BML areas and the differences in the bone morphology were also investigated.

4.2 Method

4.2.1 Sample preparation and characteristics

The human tissue used in this study was obtained from a tissue bank (MedCure Inc, USA) following National Research Ethics Committee (NREC) approval (reference 18/EM/0224). This study was part of a wider programme of work in which whole cadaveric human knees were imaged using MRI and used in experimental and computational tests. A list of the University of Leeds archive codes for the human tissue samples used in this thesis can be found in Appendix A. MR imaging and scoring was carried out by Dr Nagitha Wijayathunga. Fat suppressed T2 weighted sequence was used to identify BMLs. Patellae that were identified on MRI as having BML regions were selected for this study.

Six cadaveric human patellae from six donors were dissected. The donor details including height, weight and cause of death are described in Table 4.1. To aid the extraction of bone plugs, the patellae were potted with the posterior end embedded in PMMA, as shown in Figure 4.1.

Table 4.1: Specimen characteristics of cadaveric human patella.

Name	Age	Sex	Left/Right	Height (m)	Weight (kg)	BMI (kg/m^2)	Cause of Death
P1	61	M	L	1.83	60	18	Acute respiratory failure
P2	57	M	R	1.75	116	38	Cardio-pulmonary arrest
P3	76	M	R	1.98	102	26	Cerebro-vascular Accident (CVA)
P4	63	M	L	1.78	66	21	Lung cancer
P5	61	M	R	1.88	88	25	CVA
P6	56	F	R	1.78	67.6	21.3	Alzheimer/ Dementia
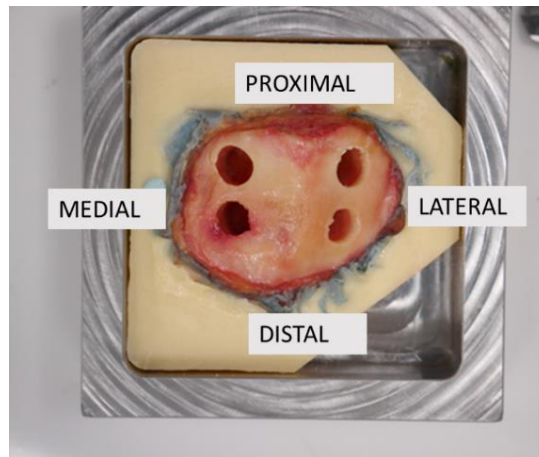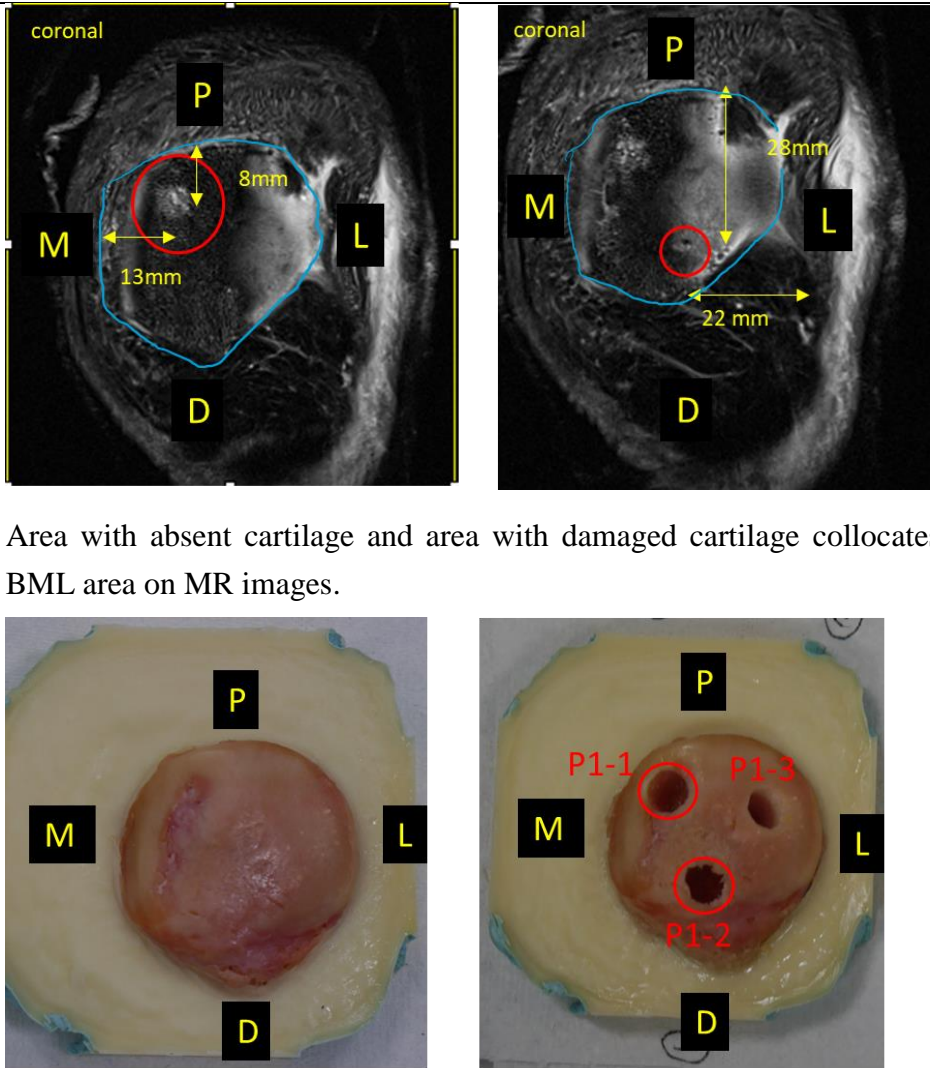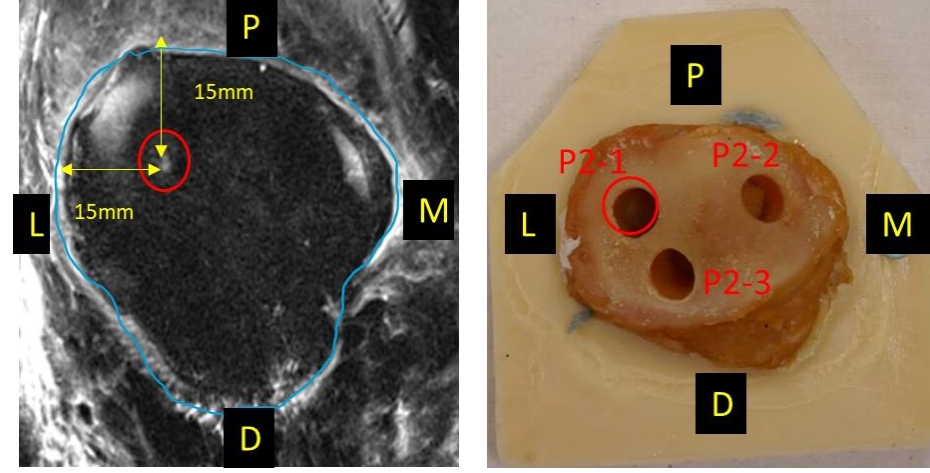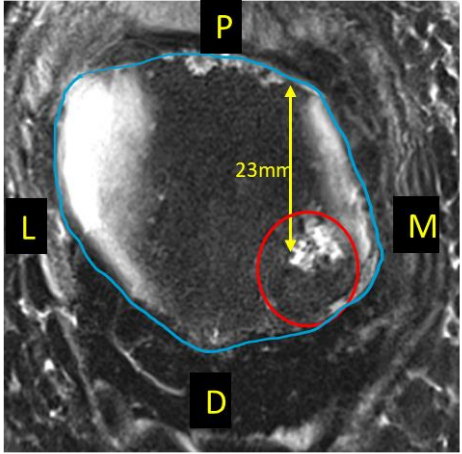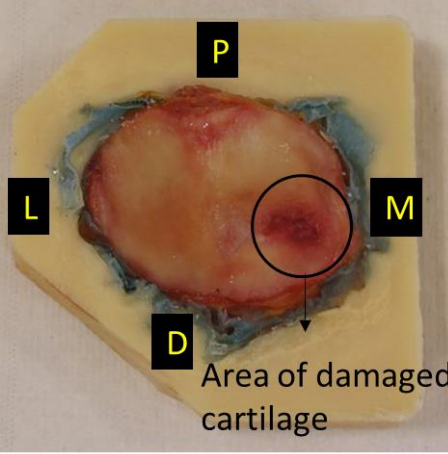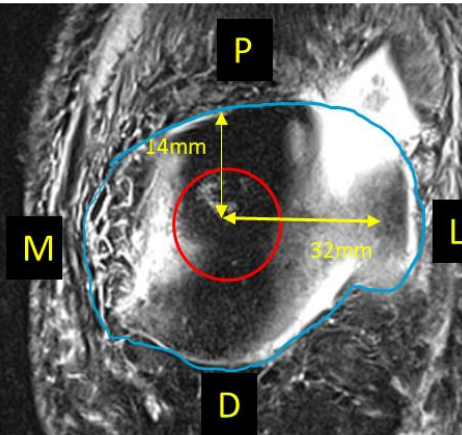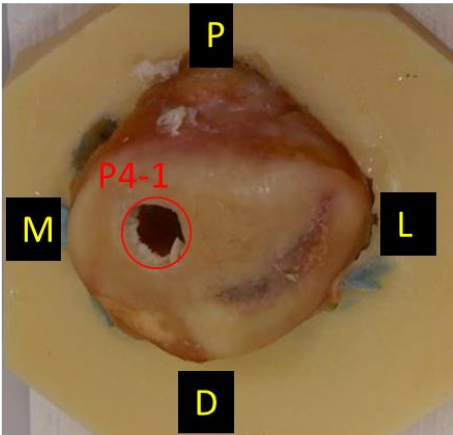
Figure 4.1: A right patella potted in PMMA, showing four extraction locations of bone plugs.
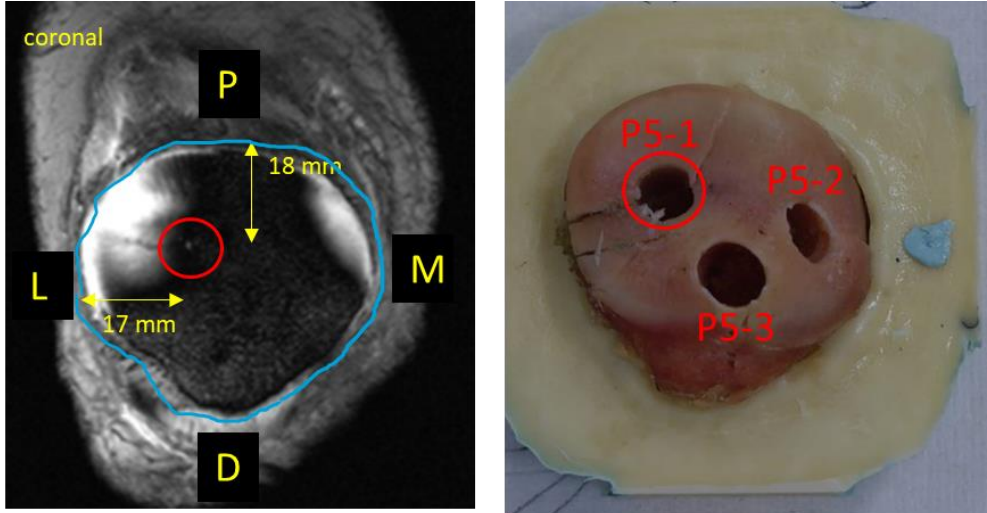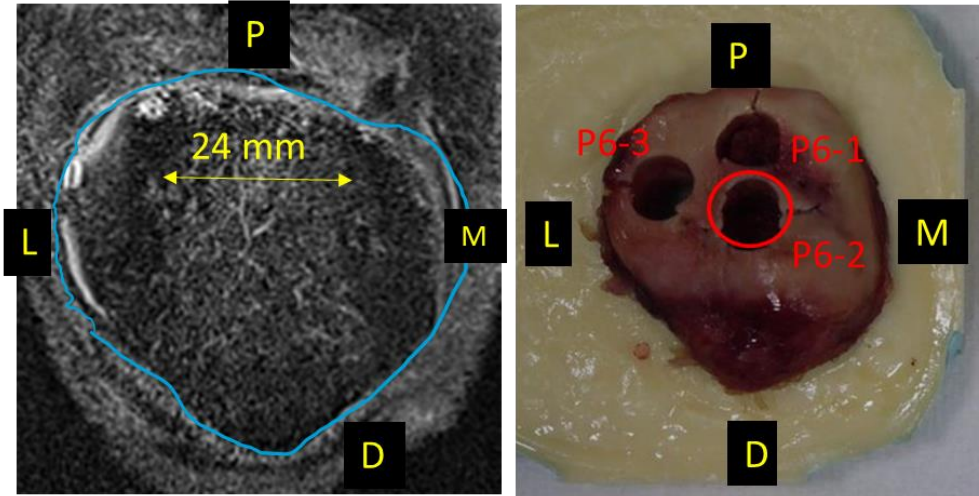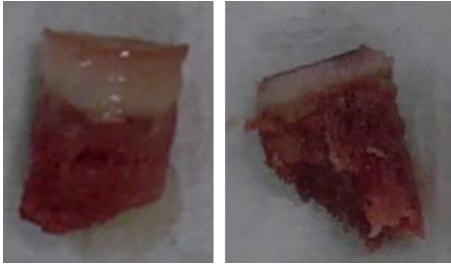
With guidance from MRI scans, osteochondral bone plugs were taken from regions of BML and regions without BMLs using 8.5 mm diameter surgical corer and a mallet as described in Chapter 3.2.1. As many bone plugs as could be extracted were taken from each patella. Patellae P4 and P5 had very dense bone which made extracting bone plugs very difficult. In the case of P4, it was not possible to extract more than one bone plug. The patella and bone plugs extracted are described in Table 4.2. Upon physical examination, it was noted that areas of damaged cartilage collocated with underlying BML areas.

The cartilage layers were taken off using a surgical blade and the bone plugs were trimmed to create a flat surface on bottom end as well. It was not possible to achieve bone plugs of a consistent height. Particularly, the bone quality in P6 was very poor and two out of the three bone plugs extracted from P6 disintegrated within the surgical corer.

Table 4.2: Descriptions of patella samples and locations of BMLs within them. The Patella is outlined in blue on the MR image to aid visualization. (M = medial, L = lateral, P = proximal, D = distal). Table continued overleaf

P1	Area with absent cartilage and area with damaged cartilage collocates with BML area on MR images.
P2	Area of damaged cartilage collocates with BML location

Area of damaged cartilage collocates with BML location

P4

BML collocates with damaged cartilage

Very dense bone therefore could only get one bone plug out.

P5	Small BML area. BML collocates with area of damaged cartilage Very dense bone made bone plug extraction difficult. patella was sawed to get P5-1 out.
P6	BML collocates with areas of cartilage damage. Cracks in patella happened while wiggling the corer out. P6-1 and P6-3 broke apart and were not tested

Seven bone plugs were extracted from BML areas and eight from non-BML areas. The bone plugs extracted are described in Table 4.3

Table 4.3: Descriptions of all bone plugs (diameter 8.5mm) extracted

Name	BML/ Non BML	Location in patella	Length (mm)
P1-1	BML	Medial	10
P1-2	BML	Ridge	12
P1-3	Non BML	Lateral	7
P2-1	BML	Lateral	10.4
P2-2	Non BML	Medial	8
P2-3	Non BML	Lateral	10.4
P3-1	BML	Medial	10
P3-2	Non BML	Lateral	10
P3-3	Non BML	Lateral	9
P3-4	Non BML	Medial	9
P4-1	BML	Medial	10
P5-1	BML	Lateral	9
P5-2	Non BML	Medial	6.5
P5-3	Non BML	Lateral	10
P6-2	BML	Ridge	10

Upon physical examination, two specimens (P2-2 and P5-3) were observed to not be straight, with non-parallel ends. Non parallel ends would lead to uneven loading of the bone plugs; therefore, these bone plugs were excluded from further testing.

4.2.2 Imaging and Testing

The bone plugs were imaged using the same settings described in Chapter 3.2.2, and tested under simple compression loading described same as in Chapter 3.2.3. Finite element models were created for each bone plug using the same method as Chapter 3.2.4.

The optimisation of the greyscale-to-elastic modulus relationship, described in Chapter 3.2.5, was carried out on three sets of bone plugs (BML group, non-BML group, all bone plugs group). The optimisation process was also run on each individual BML bone plug specimen to assess the variability from specimen to specimen.

The CT images were also processed using the BoneJ plugin [134] in ImageJ (ImageJ2, [135]) to obtain morphological measurements such as bone volume fraction (BV/TV), trabecular thickness (Tb.Th), trabecular spacing (Tb.Sp), and degree of anisotropy (DA). Trabecular thickness is a measure of the average thickness of individual trabeculae while trabecular spacing measure the average local distance between individual trabeculae. The DA is a measure of how highly oriented the trabeculae are, with DA 0 = isotropic and 1= a perfect alignment in one direction.

Simple compression tests were carried out on the bone plugs using the same method described in Section 3.2.3. Experimental stiffness and apparent modulus of elasticity was calculated from the force-displacement data recorded. Apparent modulus of elasticity is the ratio between stress and the strain in the elastic region.

Using IBM SPSS Statistics software (v25, IBM Corporation, Chicago, USA), the mean and standard deviation were calculated for each morphometric parameter for BML and non-BML groups. Due to the small sample size, a non-parametric test, Independent-Samples Kruskal-Wallis test was used to compare the distribution of the morphometric parameters between the two groups. Pearson's correlation was used to determine the correlation between bone volume fraction and apparent modulus measured in the experimental tests.

Concordance correlation was used to quantify the agreement between experimental and computational stiffness results for both groups. Concordance correlation coefficient (CCC) is a measure of agreement between two variables described by Lin [136]. It quantifies the departure from perfect agreement between two variables

4.3 Results

The results of the experimental stiffness calculated for all the bone plugs are plotted in Figure 4.2. There is a wide variation between the experimental stiffness across the bone plugs. A similar trend is seen when the experimental stiffness was normalised for bone plug length. There is also a wide range of variation between the bone plugs taken from the same patella irrespective of BML grouping. The experimental stiffness of P2-2 and P5-3 were low compared to other non-BML bone plugs from the same patella, which was expected based on the visual inspection and confirmed that these bone plugs be excluded from further testing.

The morphometric parameters measured are presented in Table 4.4 and Table 4.5. The average trabecular thickness was higher for the BML group (0.88, SD 0.11) compared to the non-BML group (0.71, SD 0.32) although the differences in the means were not significant ($P > 0.10$). The average trabecular spacing was lower in the BML group (2.58, SD 0.32) compared to the non-BML group (3.47, SD 1.49), although again the differences were not significant ($P > 0.10$). The average degree of anisotropy was also higher in the BML group (0.44, SD 0.14) compared with the non-BML group (0.35, SD 0.07), again the differences are not significant ($P > 0.10$).
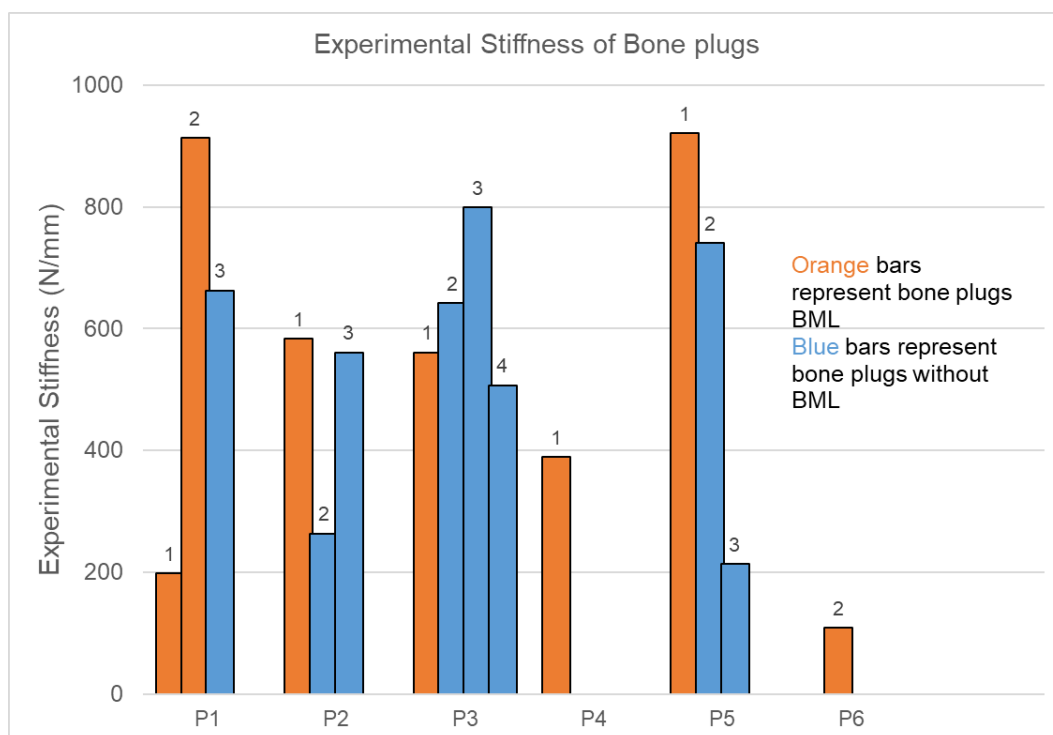
Figure 4.2: Bar chart showing the experimental stiffness for each bone plug. Data labels indicate bone plug number within patella group.

Table 4.4: Morphometric measurements for the non-BML group

	Tb.Th Mean (mm)	Tb.Th Std Dev (mm)	Tb.Sp Mean (mm)	Tb.Sp Std Dev (mm)	Degree of anisotropy (DA)
P2-3	0.60	0.32	2.33	1.82	0.34
P3-2	0.73	0.40	2.45	1.74	0.27
P3-3	0.79	0.37	3.61	2.07	0.39
P3-4	0.66	0.31	2.89	1.99	0.29
P1-3	0.60	0.26	6.36	3.17	0.33
P5-2	0.89	0.58	3.18	1.89	0.46

Table 4.5: Morphometric measurements for the BML group

	Tb.Th Mean (mm)	Tb.Th Std Dev (mm)	Tb.Sp Mean (mm)	Tb.Sp Std Dev (mm)	Degree of anisotropy (DA)
P4-1	1.55	1.07	2.11	1.50	0.19
P2-1	0.82	0.33	2.74	1.75	0.39
P3-1	0.51	0.158	2.68	1.99	0.48
P1-1	0.69	0.34	2.51	1.77	0.56
P1-2	0.82	0.67	2.45	1.80	0.64
P6-2	0.83	0.59	3.15	2.24	0.45
P5-1	0.91	0.65	2.43	1.69	0.40

Bone volume fraction was plotted against experimental apparent modulus for both non-BML and BML groups and shown in Figure 4.3 and Figure 4.4 respectively. There was moderate Pearson's correlation between BV/TV and apparent modulus in the non-BML group (Pearson's correlation coefficient, $r = 0.57$) and no correlation between in the BML group (Pearson's correlation coefficient, $r = -0.03$).

The range of the apparent modulus values is 80 – 127 MPa (mean 98 MPa) for the non-BML group and 19 - 193 MPa (mean 95 MPa) for the BML group. BV/TV values were in the range 0.18 - 0.44 (mean 0.35) for the non-BML group and 0.25 - 0.44 (mean 0.36) for the BML group.
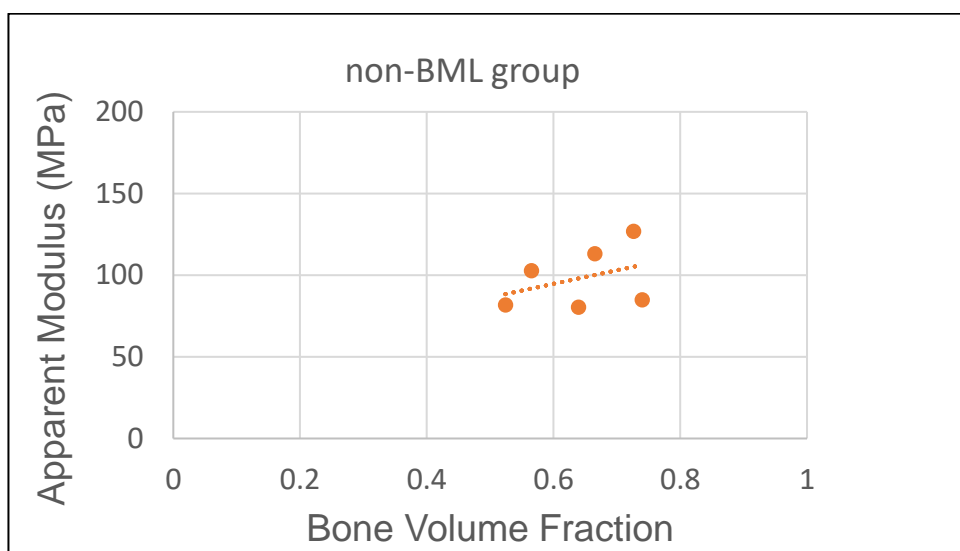
Figure 4.3: Bone volume fraction against apparent modulus for non-BML group
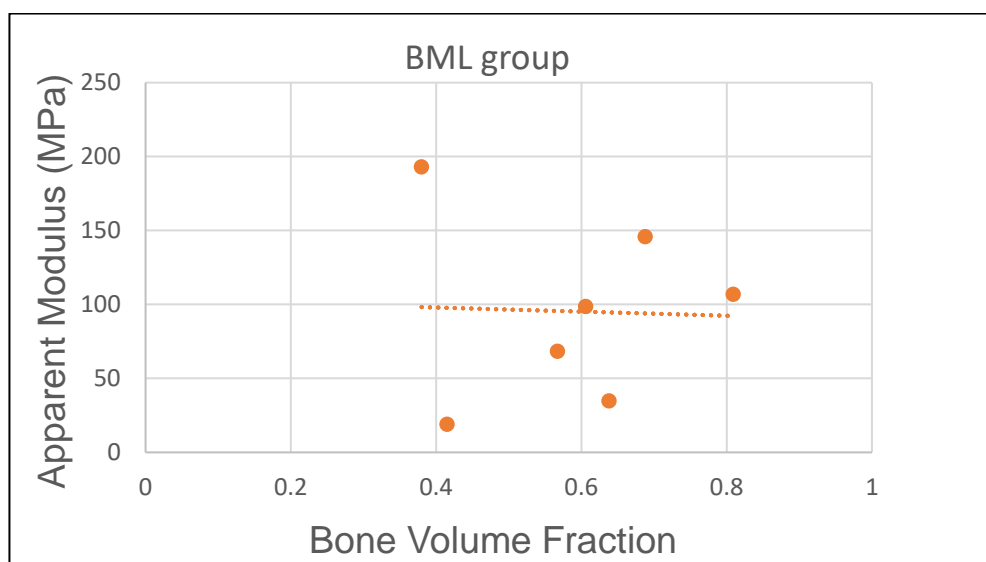
Figure 4.4: Bone volume fraction against apparent modulus for BML group.

The optimized conversion factor between bone volume fraction (BV/TV) and the young's modulus (E) of each bone element were obtained for all bone plugs, the BML group and non-BML group and presented in Table 4.6. The related root means square error (RMSE) and the concordance correlation coefficient (CCC) of the experimental and computational results were also presented. Both the RMSE and CCC are measures of the agreement between the experimental and computational results. The set containing all the bone plugs had RMSE of 51.7% and CCC of 0.04 which is a poor, separating the non-BML and BML groups gave different conversion factors and improved the agreement between experimental and computational results for the non-BML group. Although the RMSE and CCC are much poorer for the BML group.

Table 4.6: Optimized conversion factor and associated errors for different set of bone plugs. (*) represents sets with outliers included.

	Conversion factor (MPa) $$E_{bone\ element} = Conversion\ factor \times BV/TV$$	RMS error (%)	CCC
All Bone plugs	110	51.7	0.04
Non-BML	177	24.7	0.33
BML	92	55.6	0.04

The relationship between experimental stiffness and optimized computational stiffness for the non-BML is presented in Figure 4.5. The relationship between experimental stiffness and optimized computational stiffness for the BML group is shown in Figure 4.6. From the figures, it can be seen that most of the points lie below the perfect agreement line which means that most of the computational predicted stiffness are lower than the experimental stiffness.
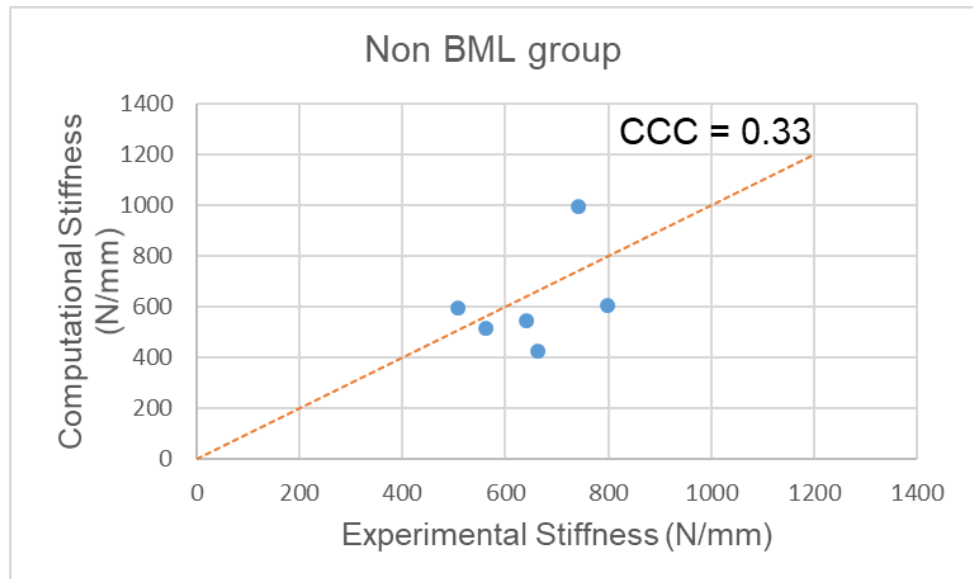
Figure 4.5: Experimental stiffness plotted against computational stiffness for non-BML bone plugs without outliers. The red dotted line represents a perfect agreement.
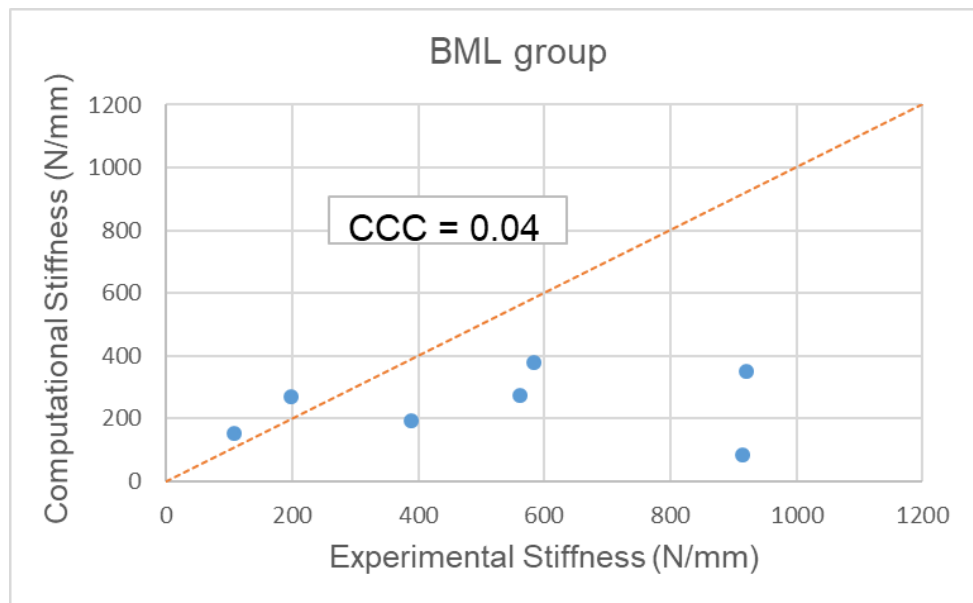
Figure 4.6: Experimental stiffness plotted against computational stiffness for BML bone plugs. The red dotted line represents a perfect agreement.

The optimisation terminated without convergence of the error (set at 10%) for any of the groups. Instead, it converged for the gradient tolerance, (set at 1e-05). This means that where there is less than 1e-5 change in the error between one iteration and the next, the optimisation terminates, however large the error.

The results presented in Table 4.7 show the optimized conversion factor and related RMSE for individual bone plug. The optimisation for individual bone plugs converged with errors less than value set (10%) which confirmed that the bone modulus optimization process was successful.

Table 4.7: Group and Individual optimisation results for all bone plugs.

Specimen Name	Group	Conversion value (group) (MPa)	RMS error (group) (%)	Conversion value (individual) (MPa)	RMS error (individual) (%)
P1-3	Non BML	177	44.8	277.9	0.12
P2-2				119.8	0.10
P2-3				193.8	0.28
P3-2				209.1	0.15
P3-3				234.6	0.02
P3-4				150.4	0.08
P5-2				130.0	0.10
P5-3				63.75	0.61
P4-1	BML	92	55.6	188.7	0.20
P1-1				66.3	0.35
P1-2				1027.6	0.03
P2-1				142.8	0.53
P3-1				191.2	0.07
P6-2				63.7	0.08
P5-1				249.9	0.02

4.4 Discussion

In this chapter, cadaveric human patellar bone plugs were tested under axial compression to derive apparent elastic modulus for plugs with and without BMLs. Moderate correlations between apparent modulus and bone volume fraction were found for the non-BML group but were non-existent for the BML group. While the elastic modulus of trabecular bone, derived from experimental tests, in other anatomical locations have been reported extensively in literature, very little has been published on human patella bone. Townsend et al carried out multi-axial compression tests on trabecular bone cubes taken from different locations on human cadaveric patella with no recorded bone pathologies [137]. The bone plugs were taken in alignment with the articular surface in the same way as in this study. The results showed apparent elastic moduli between 336 - 457 MPa in the direction normal to the articular surface. An indentation study on whole patella samples found average apparent moduli of ~200 MPa and ~320 MPa for human cadaveric patella using two different indenter sizes [138]. The range of apparent moduli reported in this study for non-BML samples (80 – 127 MPa) are lower than the reported literature values, this may be because the samples used in this study showed definite bone pathology associated with osteoarthritis.

Studies [139, 140] investigating the correlation between morphological and mechanical properties, using trabecular bone from healthy proximal femurs, found BV/TV to be the best determinant of stiffness and yield strength accounting for 89% of the variance in stiffness and yield strength, with improvements reported up to 98% when anisotropy was also taken into account. The results of this study show a moderate correlation between BV/TV and apparent modulus in the non-BML group (r = 0.57) and no correlation in the BML group (r = -0.03). Compared to literature, the correlation between BV/TV and apparent modulus is poor for the non-BML group. In a study comparing normal, metastatic and osteoporotic bone in the spine and femur, it was found that BV/TV accounted for 79% of apparent modulus regardless of pathology [141]. Although lower than the correlation reported by Musy et al and Maquer et al [139, 140], this is still a high correlation. However, a study looking at early arthritic trabecular bone from the proximal tibia found higher BV/TV but reduced bone tissue modulus in areas with overlying cartilage damage compared with unaffected areas [55]. This suggests changes to the tissue structure-elastic property relationship in arthritic bone and may account for the poor correlation between BV/TV and apparent modulus seen in our results.

Micro-CT investigations of bone cores taken from the proximal tibias of postmenopausal women undergoing knee replacement found statistically significant increase in bone volume fraction and trabecular thickness in areas with BMLs compared to unaffected areas [59], while the results from this study found no significant differences in the same parameters for the two groups. Hunter et al also reported change in trabecular architecture, with BML areas having more plate-like structure than unaffected areas.

From Table 4.6, it can be seen that different conversion factors were obtained for the BML and non-BML groups. The RMSE improved for the non-BML group by separating them from the BML group, but the agreement between experimental and computational models is still poor. While there is published literature on CT greyscale –elastic modulus relationships for human patella bone, studies which have derived CT greyscale – elastic modulus relationships using a similar method for porcine ankles [127] and human vertebra [91] have found much better agreement (CCC = 0.66, RMSE = 17% and CCC = 0.86, RMSE = 15.3% respectively). From Figure 4.5 and Figure 4.6, it can be seen that majority of the optimized FE models underestimate the stiffness of the bone plugs in the both BML and non-BML groups. The optimization was run for individual bone plugs for further investigation. Individual bone plug optimization gave a wide range of conversion factor values with very small RMS errors which suggests that large errors in the group optimizations is due to the large tissue-level variability between the specimens in the groups.

Raux et al [142], described the predominant trabecular structure in the patella to be sheets of hard tissue connected by rods with the sheets arranged in varying orientations. As shown in Figure 4.7, the sheets are vertical and arranged perpendicular to the articular surface in the proximal and mid lateral regions and the mid-crest region. While in the medial side, the sheets are horizontal and run perpendicular to the articular surface. The proximal and distal crest have trabeculae of mixed orientation. Other studies in the patella have adapted the same model [137, 138, 143].

Townsend et al reported nearly identical stiffness in the proximal and mid lateral regions and a reduced stiffness in the distal lateral region. The crest was found to be the stiffest region of the patella, with decreasing stiffness from proximal to distal. In the medial side, the middle region was found to be the stiffest region. The intra-specimen variability in the stiffness of trabecular bone in the different regions of the patella due to orientation adds a layer of complexity in making comparisons between BML and non-BML regions even within the same specimen. For example, a BML bone plug taken from the crest may

be stiffer than a non-BML bone plug taken from other areas of the same patella. This may account for the large range of stiffness values seen within the two groups. To avoid errors due to intra-specimen variability in trabecular orientation, BML and non-BML plugs taken from the same regions of the patella should be compared. This will require a much larger sample size than was used in this study. High resolution images of the patella prior to bone plug extraction could also help to identify the trabecular orientation and determine best locations for bone plug extraction.
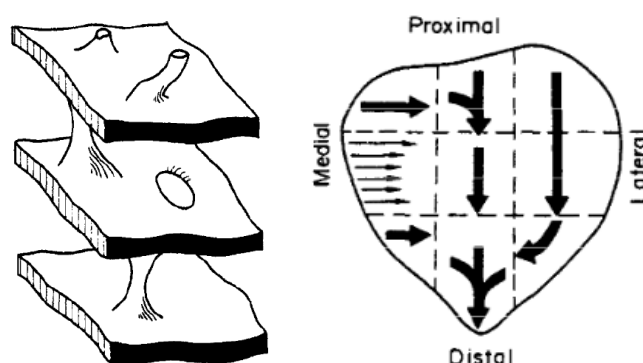
Figure 4.7: (left to right) model schematic of patella trabecular structure. Orientation of trabecular sheets in anatomical locations of the patella. (image reused from Raux et al [142] with permission)

The patellae used in this study were described in Table 4.1, and from the images, it can be seen that different specimen had BMLs of varying sizes. For example, P6 contained a large area of BML compared to P2 which contained a small BML. Therefore, bone plugs in the BML group contain fractions of BML and non-BML bone. This varying volume of BML in each bone plug would have contributed to the intra-specimen variability within the BML group. Although the bone plugs were scanned using microCT before they were tested, BMLs were not identifiable in microCT images. The location of the bone plugs extracted from patella P3 and an MR image showing the location of a BML in patella, is shown in Figure 4.8. From the cross-sectional CT images, P3-1 and P3-4 look quite similar although P3-1 contains a BML and P3-4 does not. Although MR images were used to identify the location of BMLs for plug extraction, it was not possible to define the precise extent of the BMLs from MR images due to the lower resolution of clinical MRI. Therefore, the volume of BML in each bone plug could not be accurately estimated.

Importantly, bone plugs from large BML areas (P6-1 and P6-3) fell apart and therefore were not tested. It is likely that bone in large BML areas have worse properties than the derived values for the BML group.
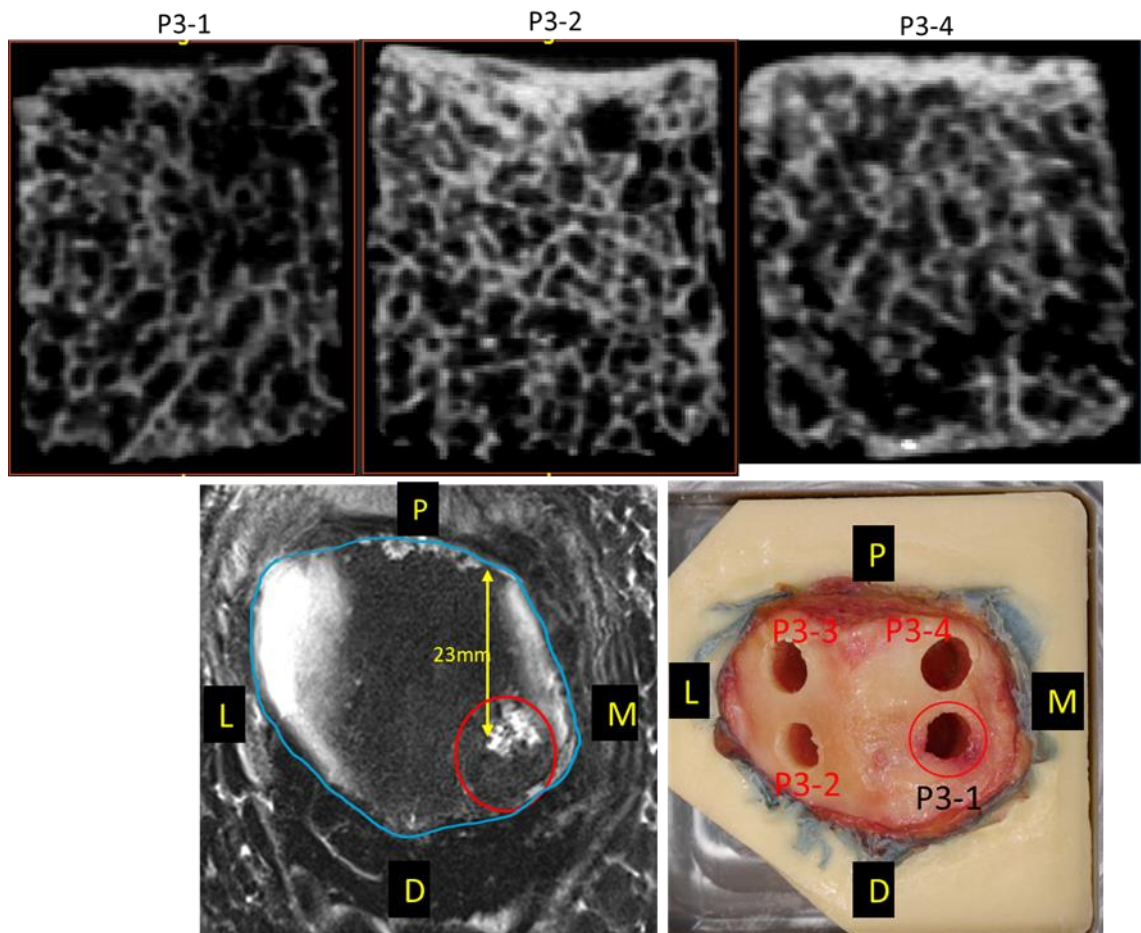
Figure 4.8: Figure shows mid-coronal CT cross sections for P3-1, P3-2 and P3-4; MR image of P3 showing the location of the BML; and potted patella P3 showing location of bone plugs. (L = lateral, M = medial, P = proximal, D = distal).

4.4.1 Summary of key points

- The bone in BML regions appear to be highly variable, with no correlation found between BV/TV and apparent modulus for these specimens although there is a moderate correlation for non-BML specimens

- Different conversion factors were derived for BML and non-BML groups indicating the bone in BML and non-BML areas are different in some way.

- Some of the BML specimens collapsed and were not tested therefore, the derived modulus was only from a subset of the specimens that could be tested.

- The agreement between the computational and experimental models was poor for both groups but poorer for the BML group. Despite this limitation, the derived conversion factors provide a way to incorporate material properties for BML regions in FE models

Chapter 5 : Assessment of the mechanical effects of BMLs in specimen-specific FE models.

5.1 Introduction

In Chapter 2, methods were developed to model tibiofemoral joints with BMLs. The results from Chapter 2 showed that a localized change in material property of bone compared to surrounding bone can affect the contact mechanics of the knee. The results also highlighted the importance of having more accurate information on the mechanical properties of bone in BML regions to properly define them in FE models. From the results presented in Chapter 4, different conversion factors were derived for BML and non-BML groups indicating that the material properties of the bone in BML areas were different to the bone in non-BML areas. The evidence from Chapter 4 has provided new data on the mechanical properties of the bone in BML regions.

The purpose of the work in this chapter was to combine the FE models developed in Chapter 2 with the material property data derived in Chapter 4 to address the last objective of this PhD project. Some improvements were made to the models developed in Chapter 2 to address some of the limitations such as the omission of cartilage and the representation of the bone. The results from Chapter 2 suggested that if bone was represented as a single material property, its value had a very small effect on contact mechanics. However, the models incorporating BML regions with different material properties to the surrounding bone showed that localized variations in material properties do have an effect on joint contact mechanics. Therefore, to represent a more realistic situation, it is also necessary to model the spatial variation of the material properties of the surrounding bone as well as the BML region. The FE models developed in this chapter incorporate inhomogeneous greyscale-based material properties for both BML regions and surrounding bone.

FE models of Knees 1-5 were created with simulated BMLs were created and compared to models without BMLs to investigate how BMLs affect joint mechanics in representations of real knees with realistic material properties (for bone in and outside BML regions) and tested under physiologically relevant loading scenarios.

Cases were created for Knees 1 and 6 with a large simulated BML with homogenous material property to investigate the effect of the elastic property of a large BML on the knee joint mechanics. These cases also serve as an investigation of possible augmentation

scenarios, as the bone substitute material is likely to have homogenous material properties.

The specimen-specific FE models developed in this chapter were validated by comparing experimental contact mechanics test results to FE model results in a similar test up. Additionally, the influence of boundary constraints on the match between experimental and FE results was also considered using one case (Knee 3). Validation of FE models in this way show that the model is able to adequately represent the experimental set up and provides confidence in the results and conclusions drawn from the FE models.

5.2 Methods

5.2.1 Specimen characteristics

Six cadaveric human knees (specimen details presented in Table 5.1) were used in this study. Three of the Knees (Knee 1-3) were dissected, tested, and segmented by Dr Gavin Day and Dr Robert Cooper, University of Leeds, as part of a previous study. The remaining three were dissected and potted by Dr Gavin Day at the University of Leeds, and tested and modelled by the author. All of the specimens were obtained as part of a larger programme of research from a tissue bank (MedCure Inc, USA) following National Research Ethics Committee (NREC) approval (reference 18/EM/0224).

Table 5.1: Donor characteristics

Specimen	Age	Sex	Left/Right Knee	Height (m)	Weight (kg)	BMI	Cause of Death
Knee 1	81	M	L	1.75	72.6	23.7	Myelodysplastic syndrome
Knee 2	61	M	L	1.83	60.3	18.0	Acute respiratory failure
Knee 3	57	M	R	1.75	116.6	38.0	Cardio-pulmonary arrest
Knee 4	89	M	L	1.73	75.7	25.4	Malignant lung neoplasm
Knee 5	83	F	R	1.50	30.8	13.7	Metastatic rectal cancer
Knee 6	58	F	L	1.83	84.4	25.2	Pancreatic cancer

All of the specimens were prepared and tested in the same way. All soft tissue, including ligaments and menisci, were removed except cartilage and the specimen were potted in PMMA with the femur at neutral extension position. To maintain neutral position of the knee, a brace was applied, following methods described by Cooper et al [79] to the femur and tibia after minimal dissection of soft tissue to expose the bone. This kept the position of the femur and tibia while other soft tissues were removed. The femur was potted in PMMA using a custom mounting rig shown in Figure 5.1. The location of centre of rotation pins, shown in Figure 5.1, were determined from the femoral insertion points of the collateral ligaments and were used to specify a centre of rotation for the femur in

alignment to the flexion-extension axis of the contact mechanics test rig. After the femur cement was fully cured, the tibia was fixed in PMMA using the same mounting rig before the braces were removed.
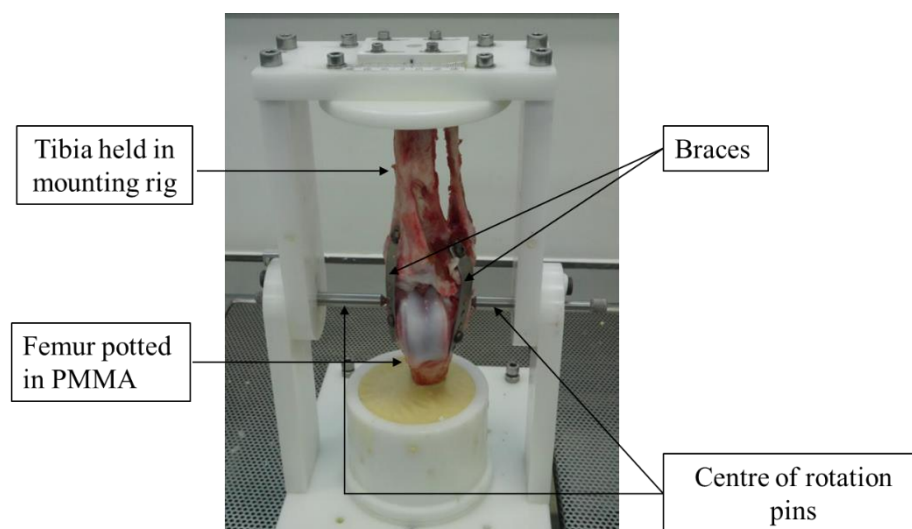
Figure 5.1: An example image showing a femur potted in PMMA using the custom mounting rig.

5.2.2 Contact Mechanics Test

The contact mechanics test was carried out using a custom testing rig developed by Dr Aiqin Liu at the University of Leeds [79]. The rig, shown in Figure 5.2, was made up of the femoral bracket, which allows the femur to be mounted at various degrees of flexion (0°– 60°), and the tibia base which can be fixed or freed in four degrees of freedom: abduction/adduction, internal/external rotation, anterior/posterior displacement, and medial/lateral displacement. In this experimental setup, the tibia was fixed in the four degrees of freedom and the knee was tested at 0°, 10°, 20° and 30° of femoral flexion.

The contact mechanics tests were carried out in a material testing machine (Instron 3365 with 5 kN load cell, Instron Ltd, UK). A compressive load of 500 N, axial to the femur, was applied to the femur at 1 mm/minute until the maximum was reached and held for 150 seconds as described by Cooper et al [79]. Contact pressure measurements were recorded for the 150 seconds the load was held using pressure sensors (Tekscan Pressure Mapping Sensor Model 400, Tekscan Inc, Boston, MA, USA) placed on the tibial cartilages and fixed using pins as shown in Figure 5.2. Prior to testing, the pressure sensors were calibrated according to the manufacturer instructions. Using the last frame of the contact pressure readings, a pressure map was produced and scaled to the load applied.
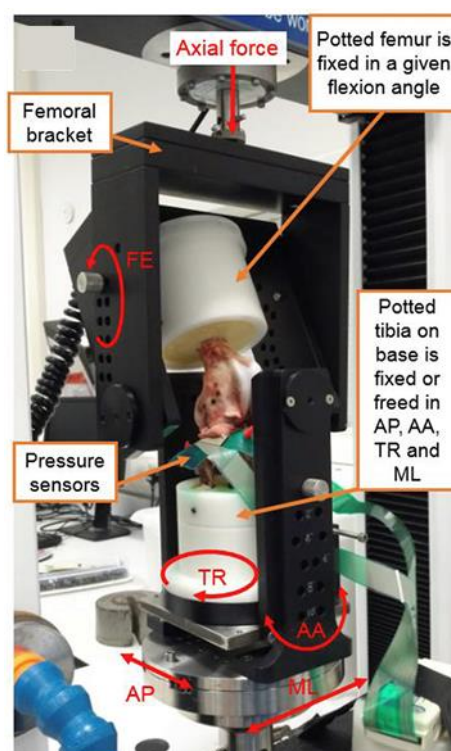
Figure 5.2: Contact mechanics test rig with loaded specimen showing the different degrees of freedom. FE = flexion/extension; TR = tibial internal/ external rotation; AA = abduction/adduction; AP = anterior/posterior displacement; ML = medial/lateral displacement. (image was adapted from Cooper et al [79])

5.2.3 MicroCT Imaging

Before mechanical testing, high resolution CT images of the potted specimens were captured at 82 µm isotropic resolution using the same scanner and scan characteristics as Chapter 4.2.2. The images produced were exported in DICOM format.

5.2.4 Finite Element Modelling

DICOM files of the specimen were imported to Simpleware ScanIP v.2019 (Synopsys, Mountain View, CA, USA). Following a similar process to Chapter 3.2.4, the images were downsampled from 82 µm to 164 µm. Using a threshold greyscale value of 478 HU (image histogram range: 0 – 4000 HU), a mask was created to capture the trabecular architecture of the bone. Another mask was created to capture the gross geometry of the bone. Using the 'flood fill' and 'inverse flood fill' tools the masks of the femur and tibia were separated. Masks were created for the femur cartilage, medial tibial and lateral tibial cartilage by highlighting the cartilage on each image slice using the paint tool. To generate smooth surfaces for meshing purposes, a recursive Gaussian smoothing filter of 5 pixels

was used. Where necessary, the masks surfaces were dilated by 2 pixels before applying the smoothing filter of to prevent over-smoothening of the surfaces and thereby prevent loss of cartilage geometry or holes in the cartilage.

Once segmented, the image containing the trabecular architecture (bone volume mask) was binarized, exported and re-imported as a background for the femur and tibia as described in Chapter 3.2.4. The background image is used in ScanIP to assign material properties to the elements. This step therefore enabled the subsequent assignment of properties to the elements to be proportional to the bone volume fraction in the given element region.

5.2.4.1 Material properties

Greyscale-based material properties were applied to the femur and the tibia with 255 increments based on 8-bit resampled image using the conversion factor between bone volume fraction and elastic modulus (177 MPa) that was derived for non-BML bone in Chapter 4.3.

The cartilage was modelled as a hyperelastic neo-hookean material with coefficients C_{10}=0.7705 MPa and D_1 =0.1067 MPa^{-1} corresponding to a bulk modulus, K, of 18.75 MPa and shear modulus, G, of 1.54 MPa. This gives an equivalent linear modulus of 4.5 MPa and Poisson's ratio v, of 0.46. These material properties come from a separate optimisation of cartilage properties in human knees carried in parallel by Dr Robert Cooper.

5.2.4.2 Mesh generation

Both bone and cartilage were meshed using linear tetrahedral C3D4 mesh elements with 0.7 mm edge length, the same edge length was used in the FE models used in Sections 3.2.4 and 4.2.2. Linear tetrahedral elements were used in this case to save computational cost as a model with quadratic tetrahedral elements took 11.5 hours to run on a high-performance computer with 32 logical processors compared to 1 hour using linear tetrahedral elements run on a computer with 8 logical processors. Both quadratic and linear tetrahedral elements gave similar results for contact pressure distribution in the tibial cartilage with only ~7% increase in the maximum contact pressure when using quadratic tetrahedral elements.

5.2.4.3 Contact definition

Surface-to-Surface contact interactions with finite sliding were created between the femur cartilage and the tibial medial and lateral cartilage. A friction coefficient of 0.1, same as used in similar studies [78, 79] was assumed between the contact surfaces and an overclosure method was used to define the normal behaviour of the contact surfaces.

5.2.4.4 Boundary conditions and loading

The distal end of the tibia was constrained for translation and rotation in all directions. A small downward axial displacement was applied to the superior end of the femur, using a reference point coupled to the nodes at the top of the femur, to produce an initial contact pressure of approximately 1 MPa. Initializing contact in this way avoids issues that may arise due to sudden non-linearity when contact happens. The displacement was constrained in all the other directions to prevent the femur from translation or rotation in the other axes. A load of 500N was then applied the femur, replicating the experimental test setup.

5.2.4.5 Output parameters

In the same manner as the finite element models of the tibiofemoral joints describes in section 2.2.1.6, the contact pressure and the von Mises stress in the tibial cartilage and bone were assessed for the different cases. The distribution of contact pressure and von Mises stress in the tibial cartilage was compared qualitatively between different cases, looking specifically at the location and number of peaks. The values of the maximum contact pressure and von Mises stress in the tibial cartilage and bone was also compared.

The distribution of minimum principal strain in the tibia bone was compared finite element model cases. Minimum principal strain is a measure of the compressive strains acting in the normal direction (direction of gravity). The distribution of minimum principal strain in the bone gives an indication of how the bone struts are bending especially in the BML regions. A qualitative assessment of the minimum principal strain in the tibia bone was made between cases with and without BMLs.

5.2.5 Validation of FE model against contact mechanics test

Contact pressure maps of FE model and experimental results were compared for each specimen. The force in each compartment, was also compared between the FE model and experimental results.

5.2.5.1 Fixed vs Free Tibia

Another case was tested for one knee (Knee 3) in the experimental set up, with the tibia freed in three degrees of freedom (anterior/posterior displacement, abduction/adduction and internal/external rotation). FE models were created for the freed and fixed tibia cases replicating the experimental scenario. The purpose of this was to examine the influence of boundary conditions on the contact mechanics both in the experimental and computational set up. Additionally, it allowed an investigation into the capability of the model to adequately represent the differences in the boundary conditions.

For this comparison, to reduce computational cost, the bones in both the fixed and free cases were modelled as homogeneous isotropic elastic materials with elastic modulus of 2 GPa and Poisson's ratio 0.3, rather than heterogeneous individual element material properties. The tibia and femur cartilage were modelled using the same material properties as Section 5.2.4.1.

Modelling the different degrees of freedom at the same time was difficult to achieve in the FE model, therefore the model was run in six steps using a method developed internally at the University of Leeds (private communication with Dr Alison Jones). In the first step, the tibia was fixed while a small displacement was applied to the femur to initiate contact between the femur and tibia cartilage surfaces. In the following steps, while a load of 500N was applied to the femur, constraints were released in one degree of freedom per step (first abduction/adduction followed by anterior/posterior displacement, then internal/external). In the final step, the tibia was allowed some abduction/adduction. The medial/lateral displacement was always constrained.

The contact pressure distributions on the tibial cartilage obtained for the fixed and free cases were compared between the experimental and computational models.

5.2.6 Modelling BML cases in specimens without BMLs

Five of the specimens (Knee 1-5) did not exhibit any naturally occurring BML therefore, a hemispherical BML with 8 mm radius was created in the medial tibia of each of those specimens using ScanIP. The BML was aligned with the centre of contact for each specimen. This was done because, as discussed in Chapter 2.2.6, BMLs at this location are likely to lead to the biggest changes in the contact pressure and von Mises stress in the cartilage.

Greyscale-based material properties were applied to the BML region using the conversion factor between bone volume fraction and elastic modulus (92 MPa) that was optimised for BML bone in Chapter 4.3. The rest of the bone was assigned properties using the conversion factor derived for non-BML bone (177 MPa). The BML was meshed with the same element type and mesh size as the bone and cartilage described in Chapter 5.2.4.2.

Finite element models were created for each specimen and tested under the same conditions as Section 5.2.4. For each specimen, the results were compared for a non-BML and BML case.

5.2.7 Effect of a large BML and its stiffness properties

Knee 6 contained a large hemispherical BML in the medial tibia, which had a primary diameter of approximately 32 mm, and extended 7.5 mm from the tibial plateau as shown in MRI images, Figure 5.3.
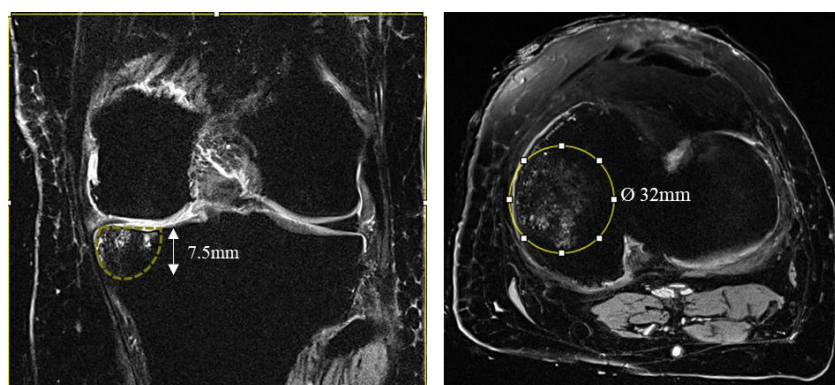
Figure 5.3: Fat suppressed T2-weighted MR images of Knee 6 showing location of BML from the coronal and axial planes.

Finite element models were created from segmented images of the specimen and set up in the same way as the models in Section 5.2.4. To capture the BML area, a hemisphere with a diameter of 28 mm was created in the medial compartment using the information from MR images about the location of the BML, as shown in Figure 5.4. The diameter of the simulated BML was less than the diameter measured from MR images because it was difficult to position a bigger idealised hemisphere within the medial compartment.
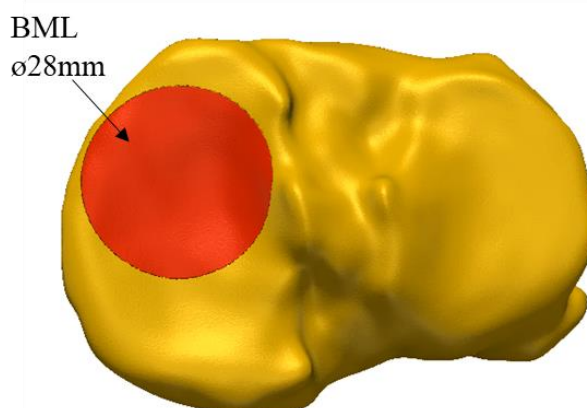
Figure 5.4: Schematic showing location and size of BML in the tibia of Knee 6 FE Model.

In both the experimental and computational set up, the femur was fixed at 30° flexion and the tibia fixed in all degrees of freedom. This loading case is different to the other specimens because unlike Knees 1 -5, there was no contact in the medial compartment of Knee 6 at 0° femur flexion. Contact in both compartments was considered necessary to avoid confounding factors due to disproportionate loading in only one compartment and to make the model comparable to the other models (Knees 1-5).

The contact pressure and von Mises stress distribution in the tibial cartilage and the minimum principal strain distribution in the tibia was compared for BML and non-BML cases.

5.2.7.1 Parametric tests on Knee 6 and Knee 1

Because Knee 6 contained a large natural BML, it is useful to investigate the effect of stiffness of bone in BML areas, therefore some other cases were created with BML areas assigned different homogenous elastic young's modulus (which were fractions of the average elastic modulus of the non-BML bone area), calculated from average bone volume fraction in non-BML bone plugs (Chapter 4.3). The use of homogenous material

properties to model the BML can also be used to consider idealised augmented cases where the homogenous cement material properties dominate in the region BML.

To investigate the effects of differing material properties in the BML region in 2 knees with different volumes of BML, the cases tested listed in Table 5.2 were tested for Knee 6 (containing a large BML) and Knee 1 (containing small simulated BML).

Table 5.2: FE model cases tested for Knee 6 and Knee 1

	Bone	BML
Case 1: Baseline	Heterogeneous greyscale based. Conversion factor for non-BML bone	none
Case 2	Heterogeneous greyscale based. Conversion factor for non-BML bone	Heterogeneous greyscale based. Conversion factor for BML.
Case 3	Heterogeneous greyscale based. Conversion factor for non-BML bone	Homogenous BML. 33.05 MPa
Case 4	Heterogeneous greyscale based. Conversion factor for non-BML bone	Homogenous BML. 15.83 MPa
Case 5	Heterogeneous greyscale based. Conversion factor for non-BML bone	Homogenous BML. 6.33 MPa
Case 6	Heterogeneous greyscale based. Conversion factor for non-BML bone	Homogenous BML. 3.17 MPa
Case 7	Heterogeneous greyscale based. Conversion factor for non-BML bone	Homogenous BML. 1 MPa

5.3 Results

5.3.1 Validation results

Contact pressure maps from experimental contact tests and FE models for each specimen are shown in Figure 5.5. The exact position of the Tekscan in the experimental set up was not known, therefore only the shapes of the contact areas and the pressure distributions can be compared between experimental and computational results.

From Figure 5.5, the shapes of the contact area in the experimental tests and FE models are very similar for Knees 1, 2, 4 and 5. For Knees 3 and 6, in the experimental results, the contact was almost all in one compartment. However, in the computational model there is some contact in both compartments.

In Knees 1, the shape of the contact area is similar between experimental and computational results for both compartments. There is one clear contact pressure peak in the lateral side which is clearly replicated in the computational results. Similarly for Knees 2 and 5, the distinct shape of the contact area in each compartment and the location of the contact pressure peak within the contact area is similar between experimental and computational results. In Knee 4, the two distinct contact areas shown in the experimental results is also shown in the computational results.

In Knees 3 and 6, there is a mismatch between the experimental and computational contact patches. In Knee 3, the experimental results show no contact in the lateral side while the computational results show contact in the lateral compartment. Also, the shape of the contact area in the medial compartment is different between the experimental and computational results. Similarly for Knee 6, the experimental results show contact in the medial compartment only while the computational results show contact in both compartments. However, the shape of the contact area in the medial side is similar for both experimental and computational results.

The maximum contact pressure was higher in the FE model for Knee 1 (50% difference) and Knee 2 (62% difference) compared to the experimental test, while the reverse was true for Knee 3 (6.5% difference). The shapes of the experimental and computational contact maps for Knee 4 and Knee 5 were similar. For Knee 6 there was a very small amount of contact in the medial compartment in the experimental result while there was contact in both compartments of the FE model. The maximum contact pressure was higher in the FE model for Knee 4 (44%) and Knee 5 (1.8%) compared to the experimental test result, while the reverse was seen for Knee 6 (37.4% decrease).

	Knee 1 (Left)	Knee 2 (Left)	Knee 3 (Right)
Experimental contact pressure map			
FE model			
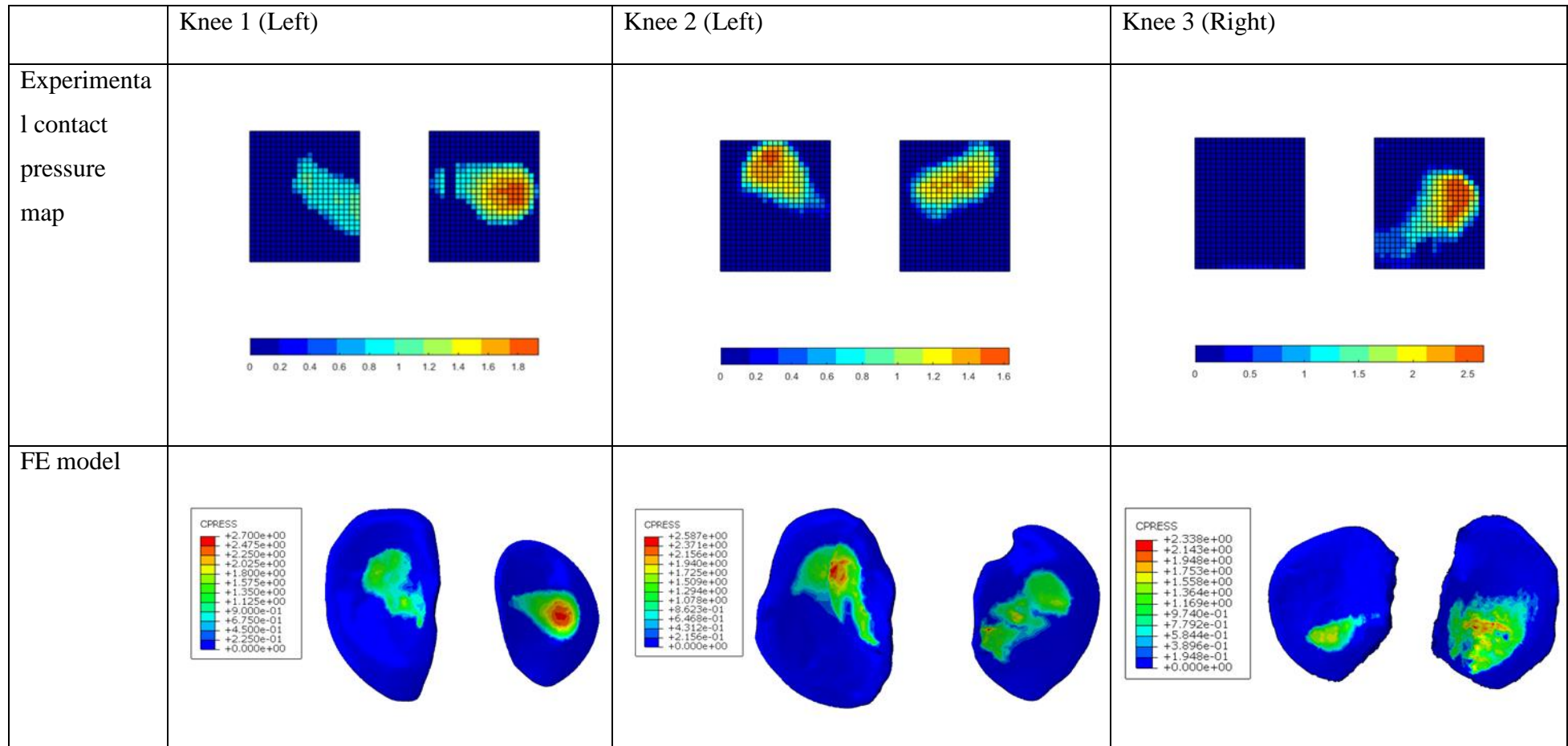
Figure 5.5: Experimental and computational contact pressure maps for Knees 1-6 (continued overleaf). (Left) or (Right) indicates if specimen is a left or right knee

	Knee 4 (Left)	Knee 5 (Right)	Knee 6 (Left)
Experimental contact pressure map			
FE model			

The force in the medial and lateral compartments for the experimental and computational models are shown in Figure 5.6. The average contact pressures in the medial and lateral compartments for the experimental and computational models are also shown in Figure 5.7. The worst agreement is between experimental and computational is for Knee 3 and Knee 6 where the experimental results show almost all of the force in one compartment.
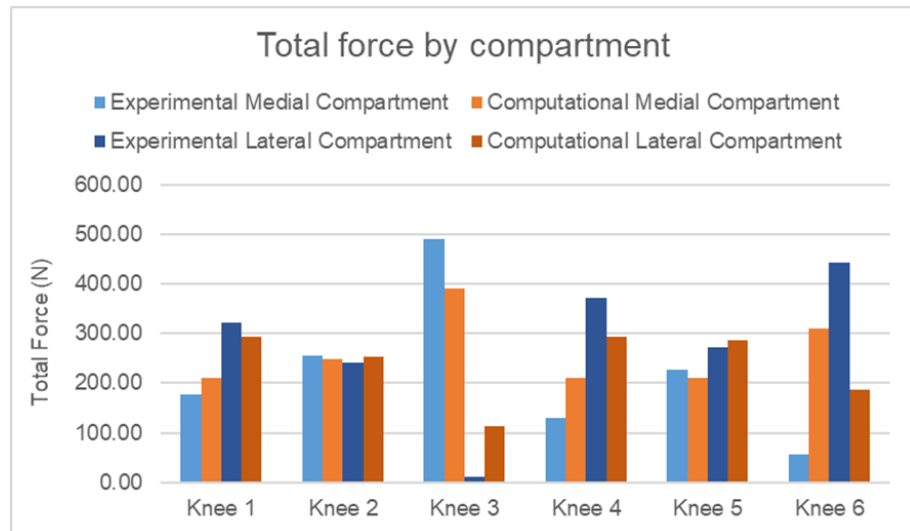
Figure 5.6: Experimental and computational force in each compartment for tested specimens.
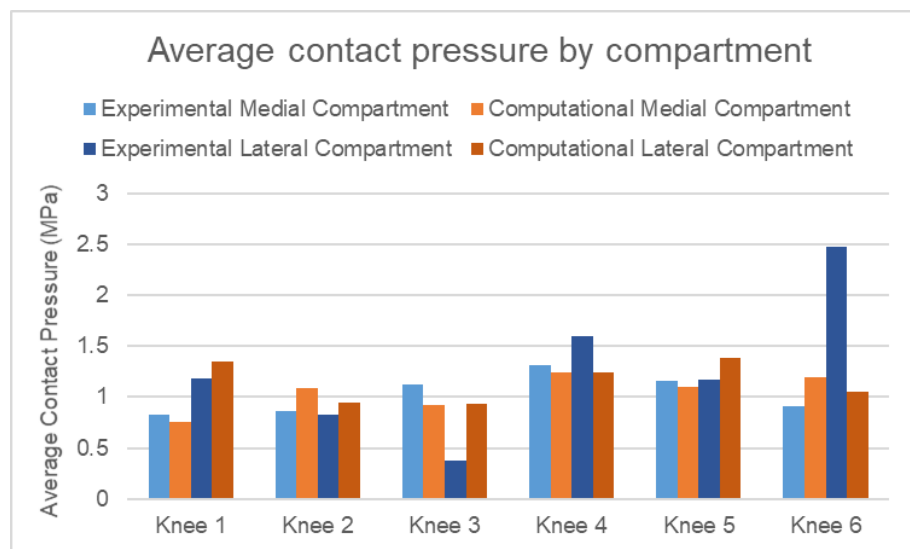
Figure 5.7: Experimental and computational average pressure in each compartment for all specimens.

5.3.1.1 Fixed tibia vs free tibia case (Knee 3)

Comparing the shapes of the contact patches shown in Figure 5.8, it can be seen that for the fixed case, there is no contact in the lateral side in the experimental result while there is contact in both compartments in the computational results. The shape and location of the contact peak in the medial side is similar between the experimental and computational results although the experimental contact area extends further. In the free case, there is contact in both compartments in the experimental and computational results. The shape of the contact area in the medial compartment is similar between the experimental and computational results. In the lateral compartment, the shape of the contact area is different between the experimental and computational results.

Results presented in Figure 5.8 show that, in the free case, there is contact in both compartments compared to the fixed case where there is no contact in the lateral side. In the fixed case, the tibia is constrained in all degrees of freedom, this means that it is not able to make small motions to ensure better contact or alignment between the femur and tibia. Freeing the tibia allows small tibial motion that allows it to correct the alignment between femur and tibia leading to better contact in both compartments instead of the medial compartment only contact seen in the fixed case.

The free case was more computationally expensive and complex with a runtime of ~5 hours compared to 1.5 hours for fixed case.

	Experimental contact test	FE model
Fixed		
Free		
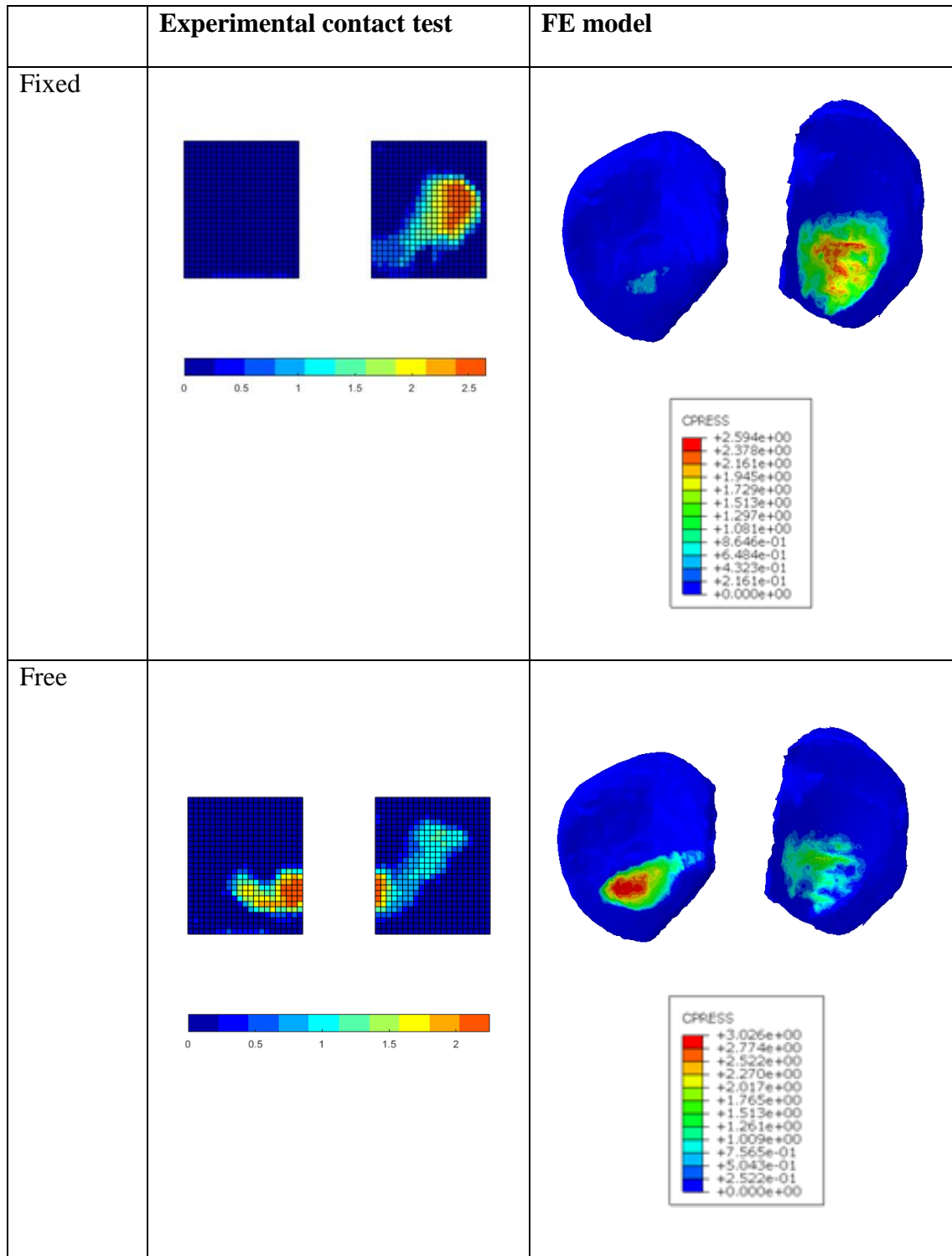
Figure 5.8: Experimental and computational contact pressure maps for the fixed tibia and free tibia cases for Knee 3 (Right Knee).

5.3.1.2 Discussion of validation study

The results provide confidence that the FE models can adequately represent the predict contact pressures, distinguish between specimens and loading conditions.

Some of the differences seen in the force and average contact pressures results between the experimental and computational model may be due to some limitations in the experimental set up. The Tekscan pressure sensor does not conform to complex shape of the tibia (where it is pinned as shown in Figure 5.2) therefore there could be some crinkling or shear in the sensor which would cause experimental errors. Other experimental errors could be due to contact outside of the sensor which would not be captured in the experimental result. Differences in the maximum contact pressures between the experimental and computational results could also be due to localised peaks in the FE models as a result of a coarse mesh, although this is unlikely given the smoothness of the contour plots in Figure 5.5. Localised peaks are less likely in the computational models because of a finer mesh (element edge length = 0.7 mm) in comparison to the coarser sensels used in the experimental tests (Pitch = 1.3 mm).

The material model used could also be a source of error, however, due to inter-specimen variability in the quality of cartilage it is doubtful that a single material model would give the best match with experimental contact tests for all specimens. Individual calibration of cartilage material property for each specimen could give better correlation between FE model and experimental maximum contact pressure but it is unlikely to fully resolve the differences.

Looking at the fixed and free cases of Knee 3 shown in Figure 5.8, it can be seen that there is better agreement between the contact area shape and the maximum contact pressure in the free case, where there are fewer constraints, than in the fixed case. This is because in cases when there are a lot of boundary conditions, the results are more sensitive to the alignment between the femur and the tibia. Small differences in the Femur-Tibia alignment between the experimental and computational set up can cause large differences in the results hence the mismatch between the experimental and computational results in the fixed case. However, given that the main purpose of this study is to compare the same model with and without BMLs, the most important requirement is for the boundary conditions and alignment to be consistent between cases. Additionally, the free case is computationally expensive to run, therefore, the fixed tibia case at 0° femur flexion was selected for Knees 1-5, and the fixed tibia case at 30° femur flexion was selected for Knee

6 as these always produce contact over the BML area and contact distribution between the two compartments.

5.3.2 Comparison of FE Models with and without BMLs

Contact pressure maps of cases with and without a BML are compared in Figure 5.9. It can be seen from Figure 5.9 that there is no observable difference in the contact pressure results between the cases with and without a BML for each of the specimen.

Maps of the von Mises stress on the tibial cartilage surface, for cases with and without BMLs are shown in Figure 5.10. It can be seen that there is no observable difference in the von Mises stress distribution in the cartilage between the cases with and without a BML for each specimen. There was also no observable difference in the maximum and minimum principal strains in the tibial cartilage for cases with and without BML.

The minimum principal strain distribution across cross-sections of the tibia for cases with and without a BML is shown Figure 5.11. The results show an increase in the peak compressive strain in BML regions for all specimens. In Knee 1, the peak minimum principal strain in the BML region increased from < 1% to ~3.5% with the presence of a BML. In Knee 2, the peak minimum principal strain in the BML region increased from < 2% to ~ 5% in the BML area and from ~ 3 – 4% to ~9% in the region adjacent to t the BML. In Knee 3, the peak increased from ~1% to ~3% in the BML region. In Knee 4, the peak increased from ~ 1.5% to ~ 4%. In Knee 5, the peak minimum principal strain in the BML region increased from ~ 2.5% to ~ 7%.
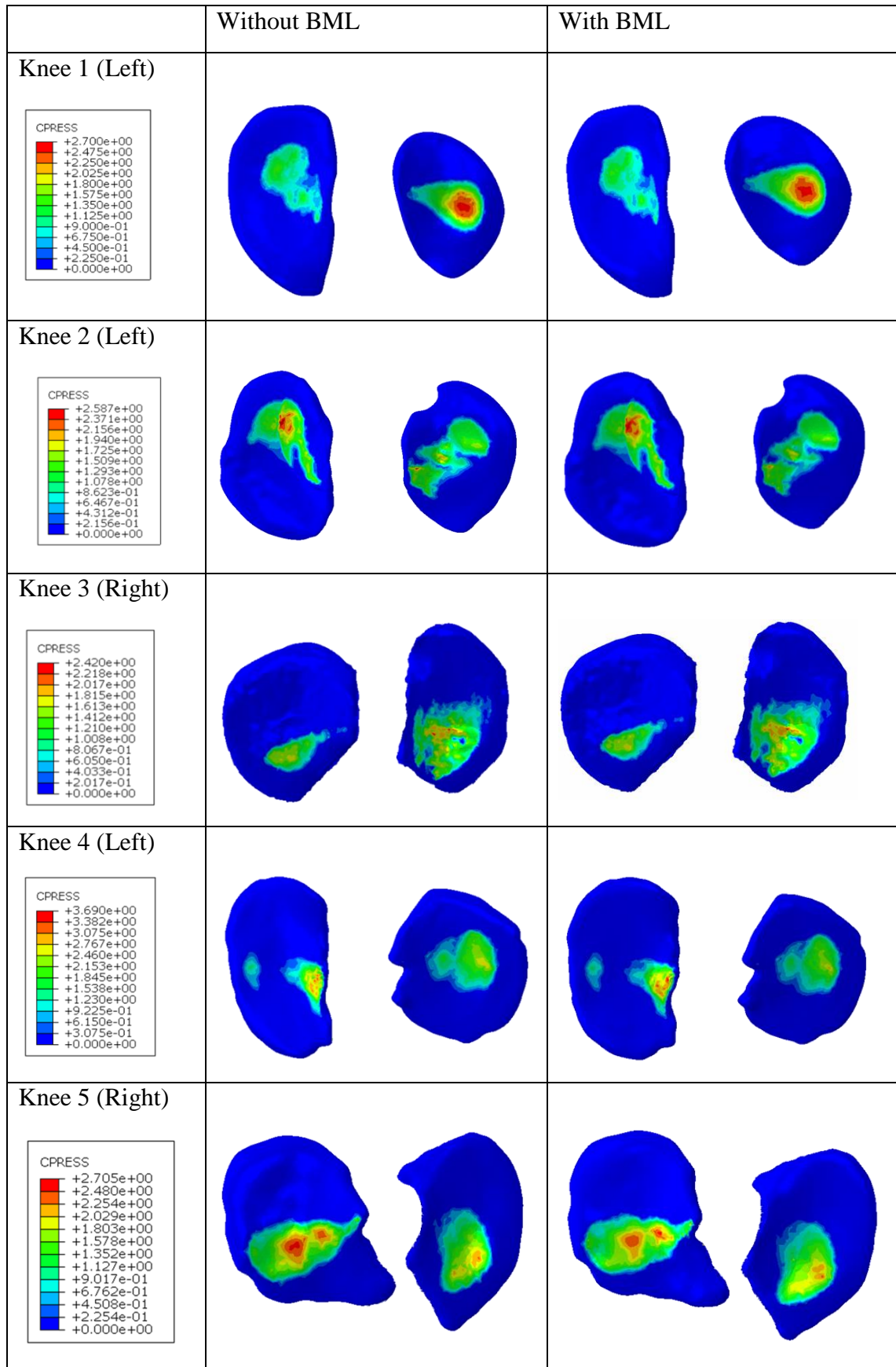
Figure 5.9: Contact pressure results in the tibial cartilage for cases without and with BMLs matched for each specimen. (Left) or (Right) indicates if specimen is a left or right knee
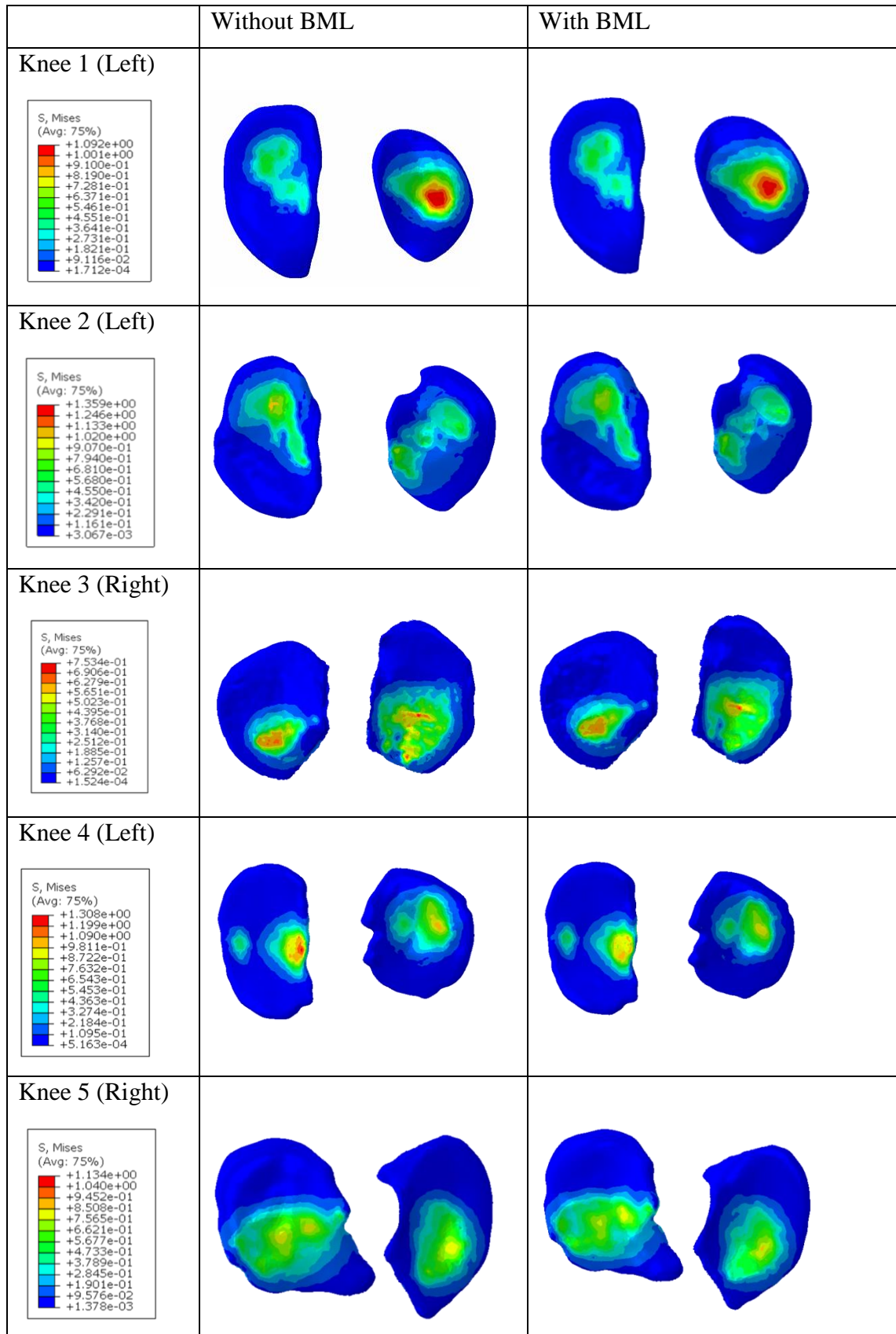
Figure 5.10: von Mises stress distribution in the tibial cartilage for cases without and with BMLs matched for each specimen. (Left) or (Right) indicates if specimen is a left or right knee

	Scale Bar	Without BML	With BML
Knee 1 (Left)			
Knee 2 (Left)			
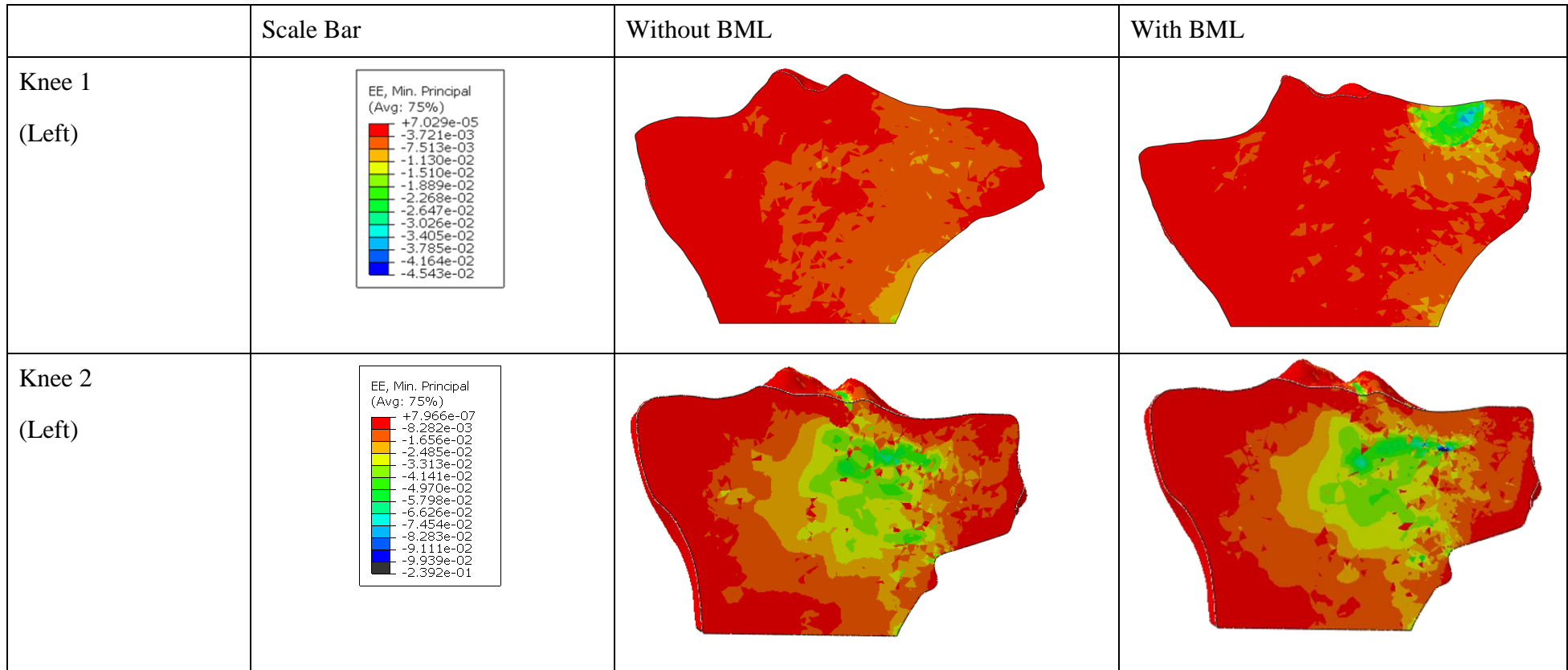
Figure 5.11: Minimum principal strain distribution for cases without and with BMLs for Knees 1- 5. (Continued overleaf). (Left) or (Right) indicates if specimen is a left or right knee

Knee 3 (Right)	EE, Min. Principal (Avg: 75%) +1.215e-04 -3.917e-03 -7.955e-03 -1.199e-02 -1.603e-02 -2.007e-02 -2.411e-02 -2.815e-02 -3.219e-02 -3.622e-02 -4.026e-02 -4.430e-02 -4.834e-02		
Knee 4 (Left)	EE, Min. Principal (Avg: 75%) +4.241e-04 -4.703e-03 -9.830e-03 -1.496e-02 -2.008e-02 -2.521e-02 -3.034e-02 -3.546e-02 -4.059e-02 -4.572e-02 -5.085e-02 -5.597e-02 -6.110e-02 -1.212e-01		
Knee 5 (Right)	EE, Min. Principal (Avg: 75%) +2.295e-04 -8.123e-03 -1.648e-02 -2.483e-02 -3.318e-02 -4.153e-02 -4.989e-02 -5.824e-02 -6.659e-02 -7.494e-02 -8.330e-02 -9.165e-02 -1.000e-01 -2.689e-01		

5.3.3 Effect of a large naturally occurring BML

The contact pressure and von Mises stress distributions in the tibial cartilages are shown for different cases of Knee 6 in Figure 5.12 and Figure 5.13 respectively. Using the same scale bar for the results, there is no observable difference seen in the contact pressure distribution between the case without BML (modelled using the conversion factor for non-BML bone) and the case containing a BML modelled using material properties based on the conversion factor derived for bone in BML areas. The contact pressure maps for the case with the BML assigned heterogeneous properties using the conversion factor and the homogenous BML with elastic modulus of 33.05 MPa are very similar. As the elastic modulus of the BML was reduced, the distribution of the contact pressure was found to shift away from the BML location in the medial compartment. Also, the contact pressure in the lateral side appeared to increase as the elastic modulus reduces. This same trend was seen in the von Mises stress distribution, shown in Figure 5.13.

The minimum principal strain in the tibia bone was compared for all cases and shown in Figure 5.14. It can be seen that there are higher maximum compressive strains in the BML region for the cases with a BML compared to the no BML case. Comparing the case with a BML, using the conversion factor derived for bone in BML area, to the no BML case, it can be seen that the peak minimum principal strain increases in the BML region from $< 1\%$ to $\sim 2.5\%$. As the elastic modulus in the BML region reduces, the peak compressive strain in this region increases, reaching up to 55%. Comparing the BML using greyscale conversion factor to the Homogenous (33MPa) case, the peak minimum principal strain is higher in the homogenous case and more distributed across the whole BML region in comparison to the greyscale conversion factor BML case.
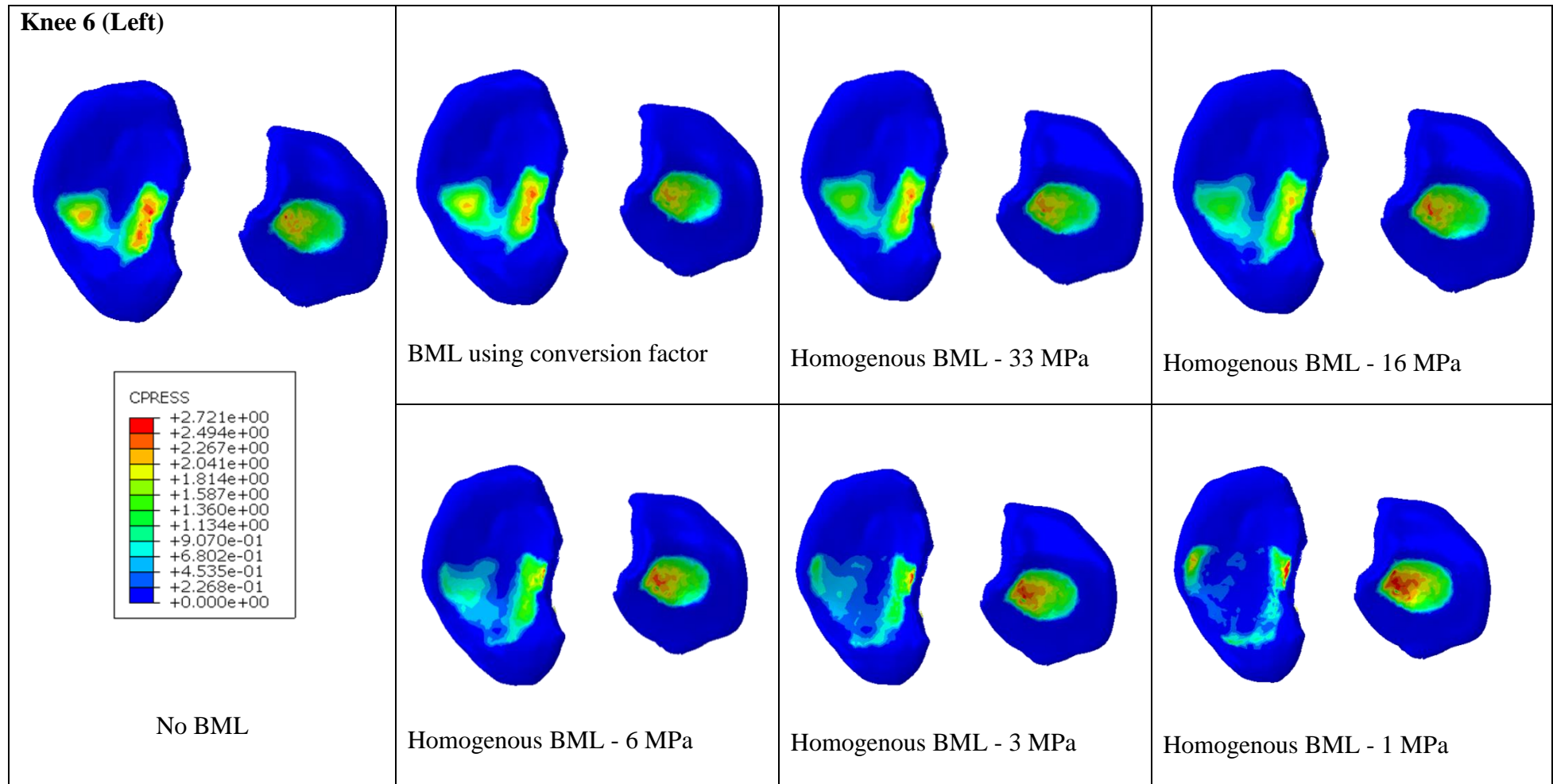
Figure 5.12: Contact pressure maps for FE models of Knee 6 at 30 degrees flexion without BML, and with BMLs of varying elastic modulus. (Left) indicates specimen is a left knee
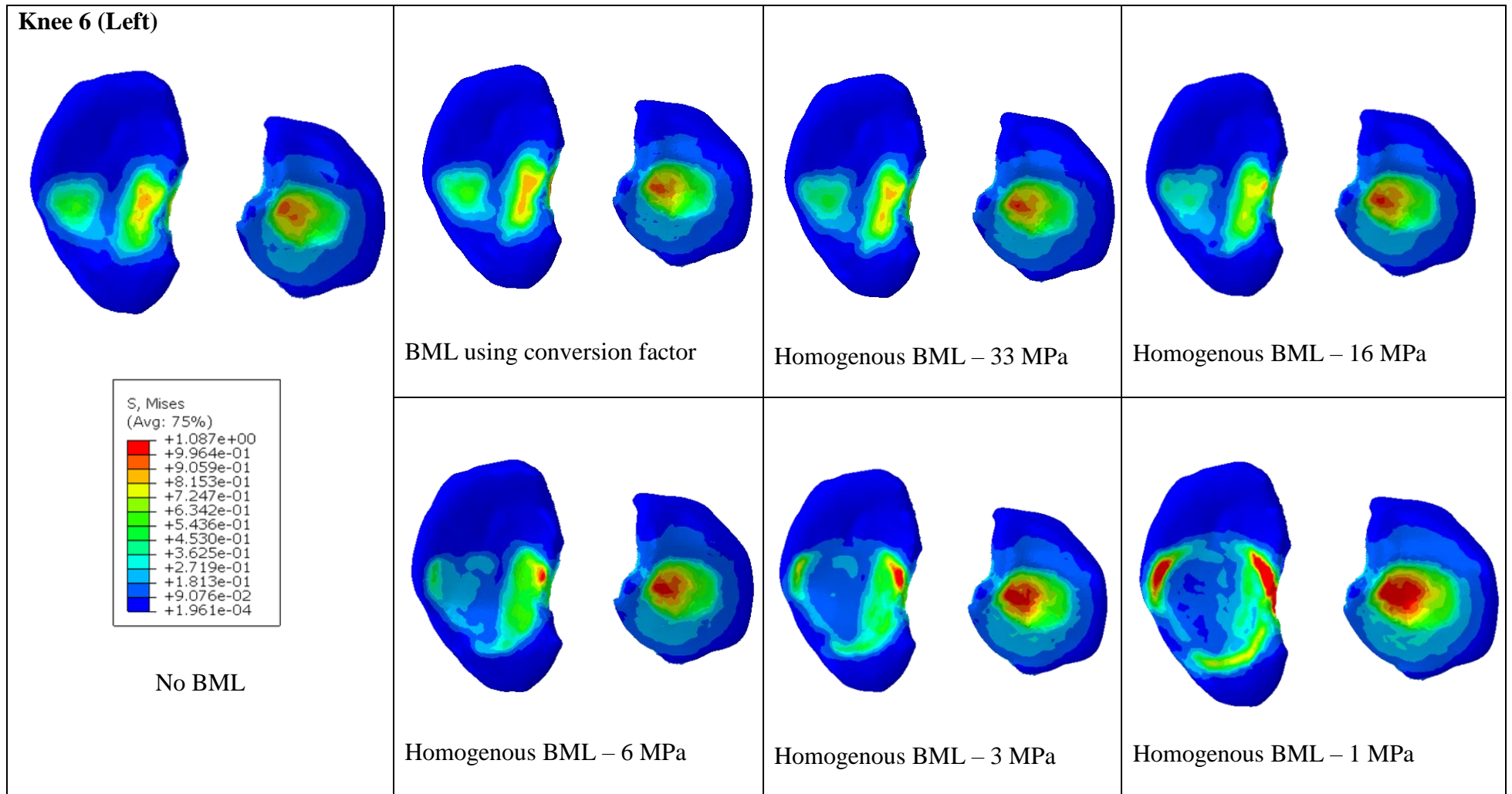
Figure 5.13: Von Mises stress maps for FE models of Knee 6 at 30 degrees flexion without BML, and with BMLs of varying elastic modulus.
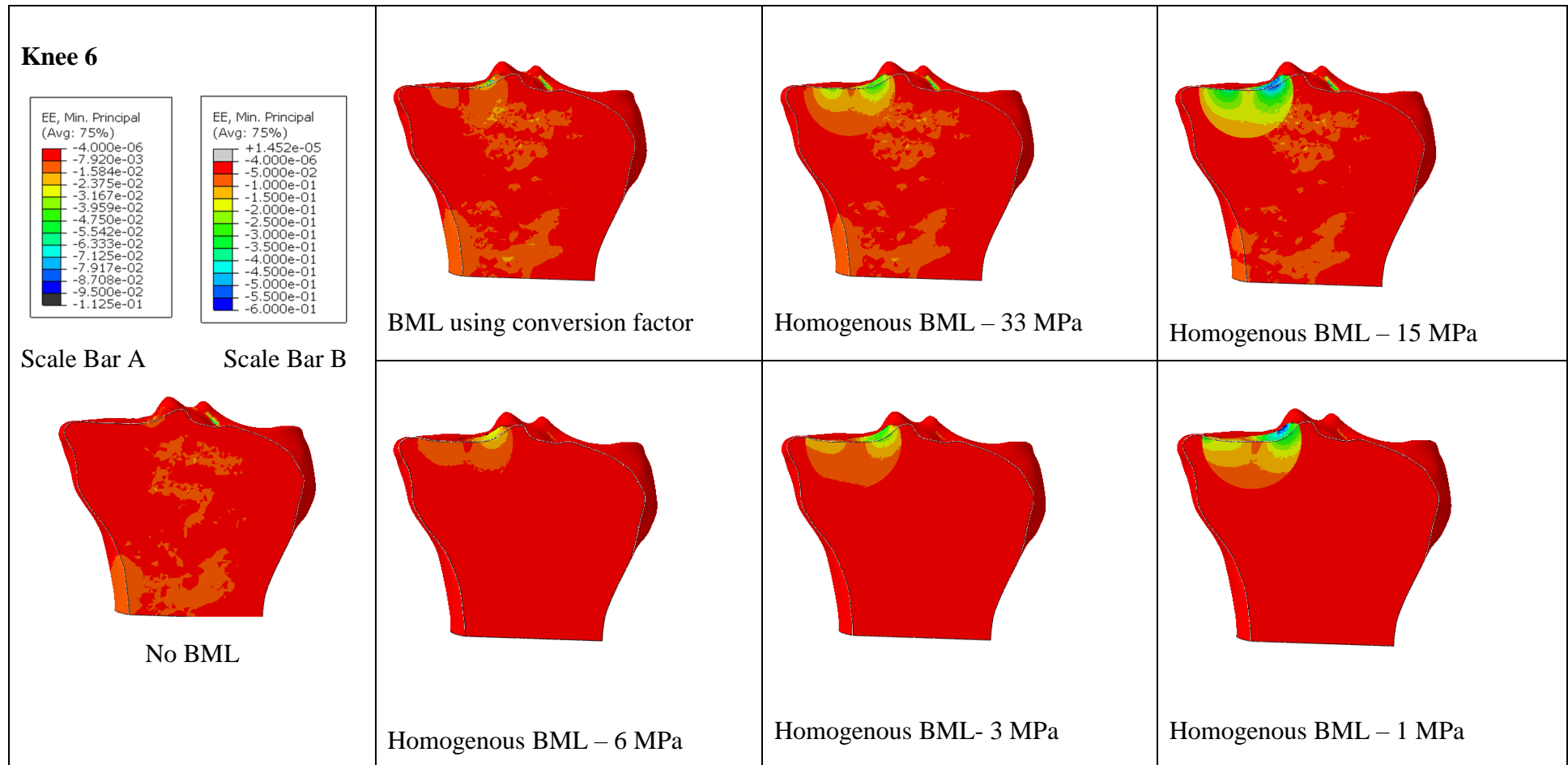
Figure 5.14: Minimum principal strain distribution for different cases of Knee 6. Scale Bar A is used for the No BML, BML with conversion factor, Homogenous BML 33MPa and 15 MPa cases; Scale bar B is for the Homogenous BML 6 MPa, 3MPa and 1 MPa cases.

5.3.3.1 Knee 1

The contact pressure and von Mises stress distributions for the different cases tested for Knee 1 are shown in Figure 5.15 and Figure 5.16 respectively.

The results in Figure 5.15 show that distribution of contact pressure in the cartilage overlying the BML changes as the elastic modulus of the BML area is reduced. The location of the maximum contact pressure moves away from the centre of contact where the BML is located. The same trend is seen in the distribution of von Mises stress shown in Figure 5.16.

The minimum principal strain in the tibia bone was compared for all cases and shown in Figure 5.17. Similar to Knee 6, it can be seen that there are higher maximum compressive strains in the BML areas for the cases with a BML compared to the no BML case. Comparing the case with a BML, using the conversion factor derived for bone in BML area, to the no BML case, it can be seen that the peak minimum principal strain increases from < 1% to ~ 4% in the BML region. As the elastic modulus in the BML region reduces, the peak compressive strain in this region increases reaching up to ~ 55% in the 1 MPa case. Comparing the case with BML modelled using greyscale conversion factor to the Homogenous (33MPa) case, the peak minimum principal strain is a little higher in the homogenous case and more distributed across the whole BML region in comparison to the greyscale conversion factor BML case.
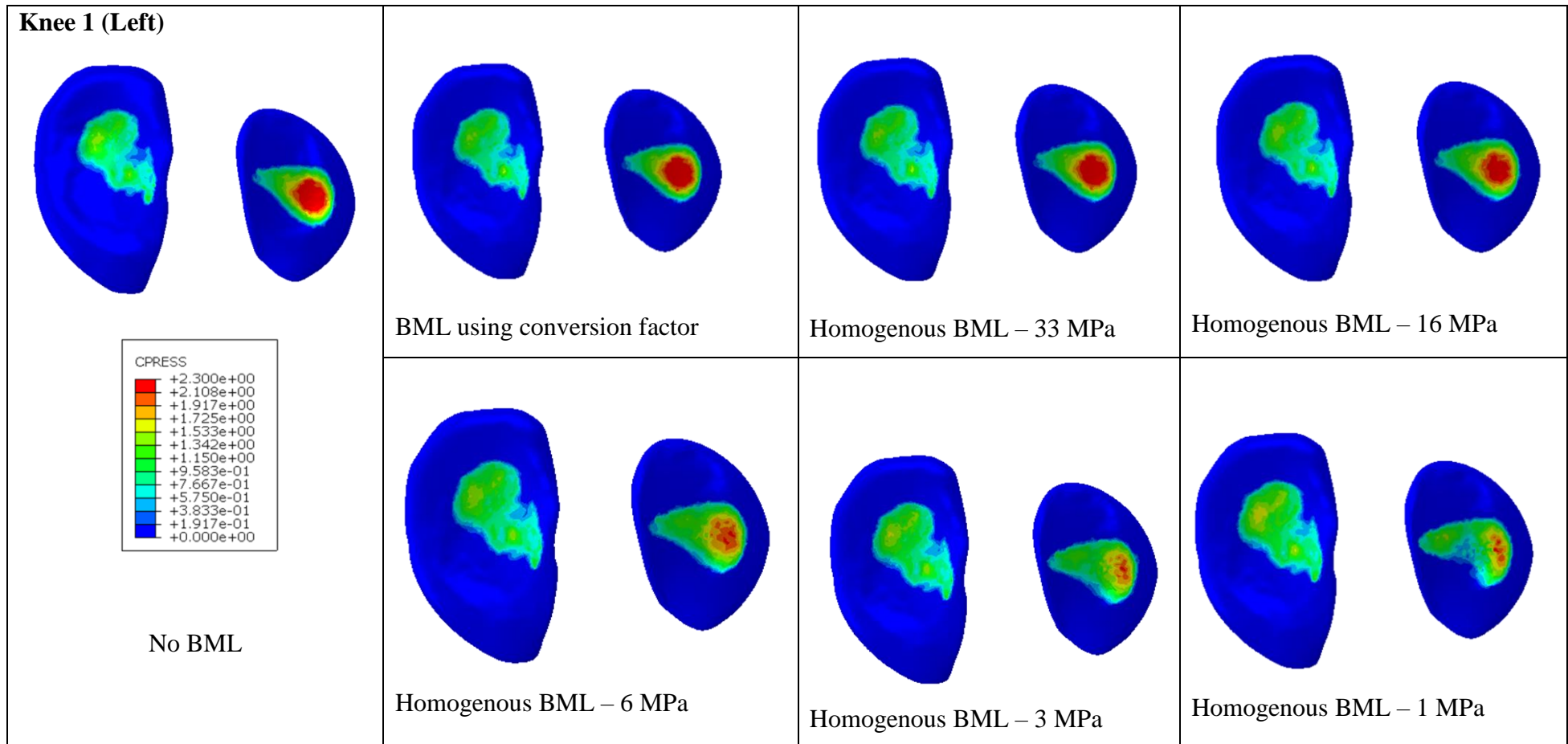
Figure 5.15: Contact pressure maps for FE models of Knee 1 without BML, and with BMLs of varying elastic modulus.
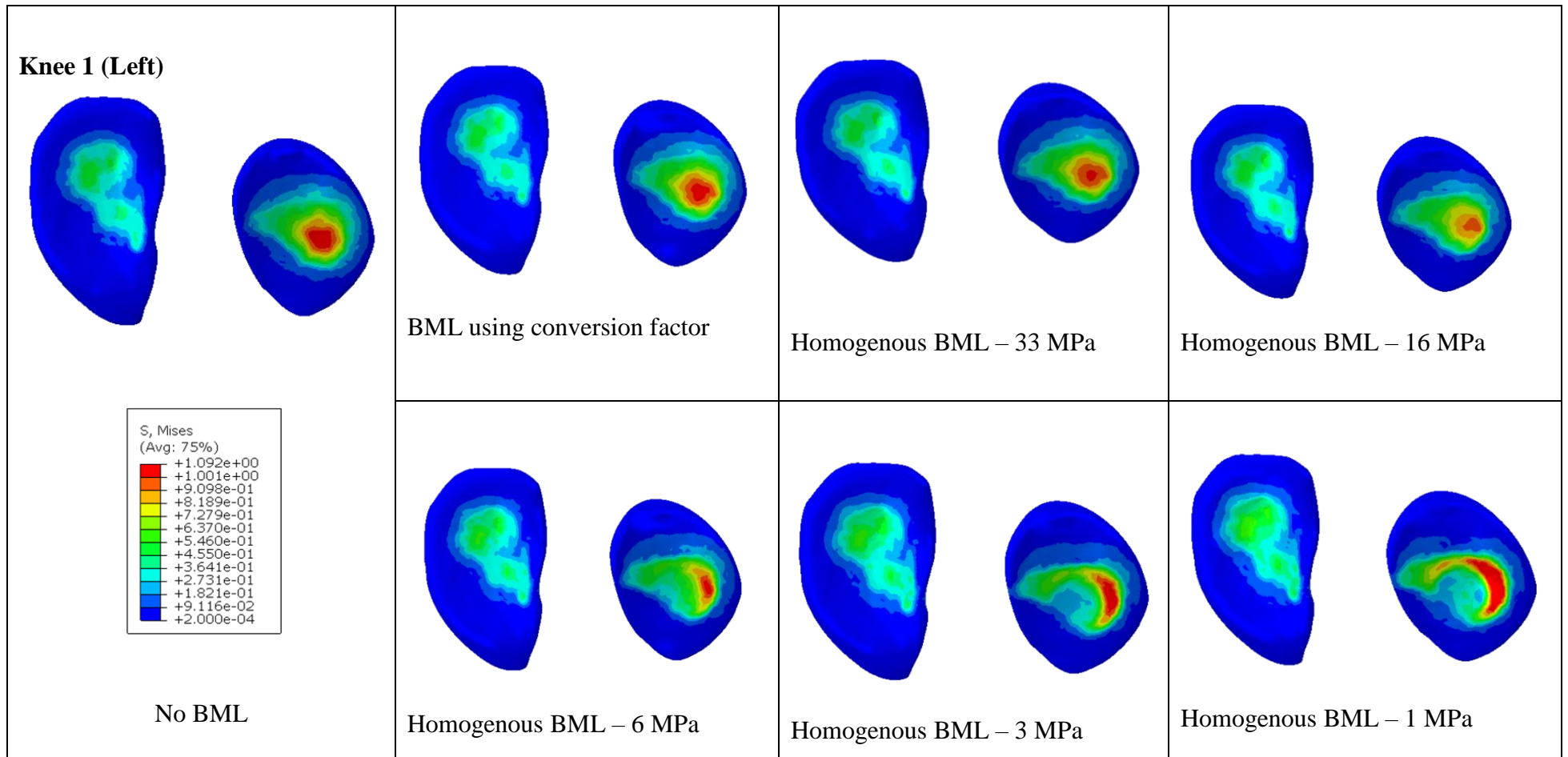
Figure 5.16: Von Mises stress maps for FE models of Knee 1 at 0 degrees flexion without BML, and with BMLs of varying elastic modulus
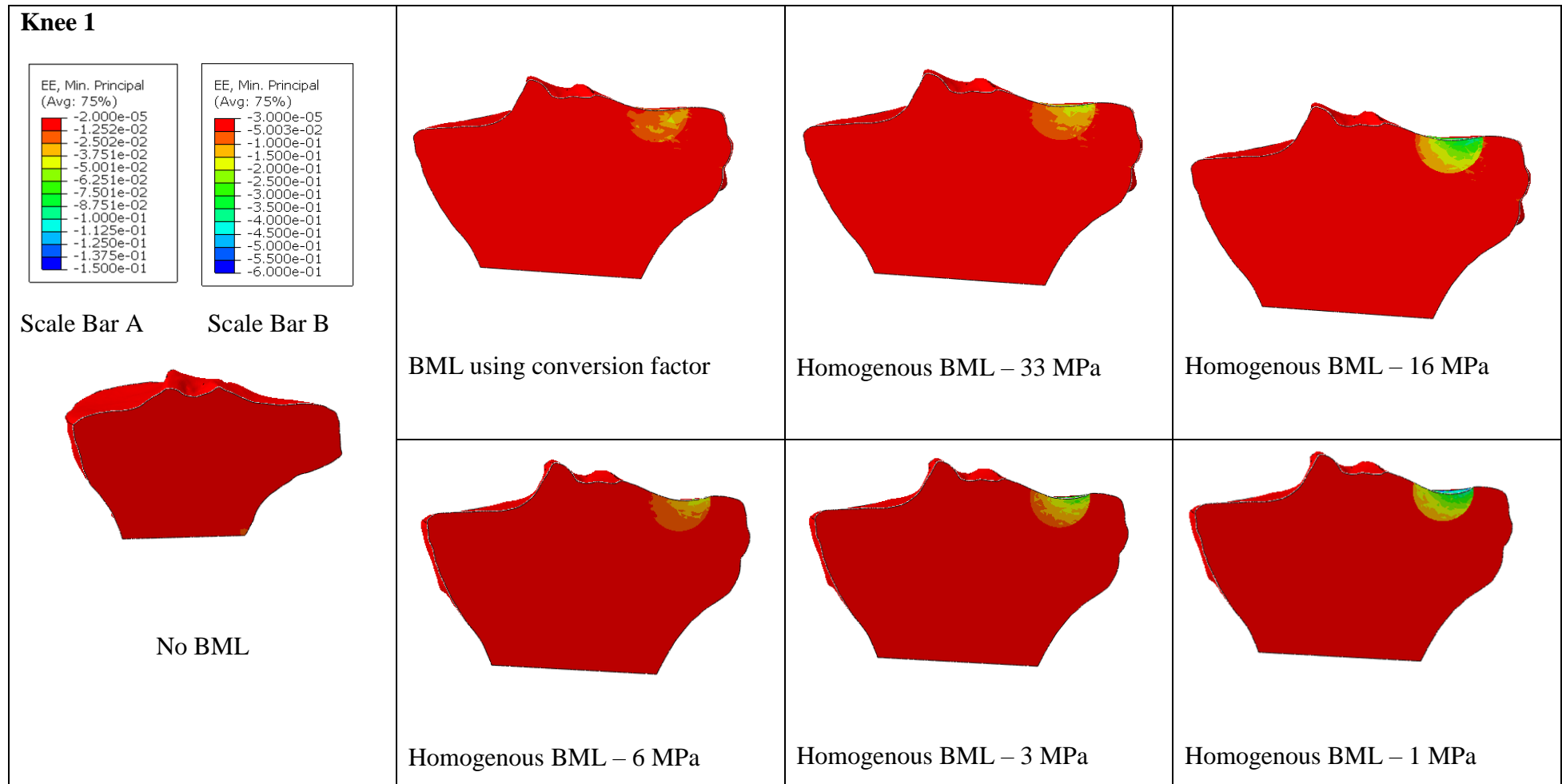
Figure 5.17: Minimum principal strain distribution for different cases of Knee 1. Scale Bar A is used for the No BML, BML with conversion factor, Homogenous BML 33MPa and 15 MPa cases; Scale bar B is for the Homogenous BML 6 MPa, 3MPa and 1 MPa cases.

5.4 Discussion

The specimen-specific FE models in this chapter were validated against experimental contact mechanics tests. Validation against experimental tests provides confidence in the model's ability to replicate the loading scenario. The similarities in the contact distribution maps between the FE models and experimental provide confidence that the FE models are able to adequately represent the loading scenario. The BML and non-BML cases modelled in this chapter were tested in the same loading scenario as the experimental set up against which the models were validated. This provides confidence in the results from this study.

The results presented in Section 5.3.2 show no observable differences in the contact pressure and stress distribution in the tibial cartilage between the cases without a BML and with a BML using the greyscale-based material properties to represent bone based on the conversion factors derived for non-BML and BML bone in Section 4.3. Also, from Figure 5.11, it can be seen that the peak minimum principal strain in the BML region increased for all cases up to ~6%. Odgaard et al. [40] reported local strains of 3.7% in failing regions of trabecular bone from human proximal tibias while Bayrakter et al. [144] found 0.6% - 1% yield strain using human femoral neck trabecular bone. However, recent studies looking at single trabeculae using digital image correlation have suggested have found high local strains of up to 10% before crack formation [145-147]. For each of the specimens (Knees 1 -5), the peak minimum principal strain increased in the BML regions while the strain in non-BML regions remain identical. The peak minimum strains in models with BMLs are high but remain less than 10% (threshold for crack formation) and are localized. This might suggest localized bone remodelling in BML areas. Since the cartilage results are identical for cases with and without BML, this suggests that increased strains seen in the bone might not be high enough to cause changes in the cartilage.

In Chapter 4, bone plugs from BML areas of human cadaveric patellae were tested. Only intact bone plugs were used for testing while others crumbled. The crumbling of some bone plugs suggests that some BML bone plugs have much poorer material properties than those that could be measured. To capture this, cases with further decrease in elastic modulus of BML area were tested. From Figure 5.12 and Figure 5.13, it can be seen that further decreases in the material property of bone in the BML regions changes the distribution of contact pressure and von Mises stress in the overlying cartilage.

From Figure 5.14, it can be seen that as the elastic modulus in the BML region reduces, the peak compressive strain in this region increases. It is interesting to note that from the case with BML elastic modulus of 6 MPa, the peak minimum principal strain in the BML region is > 10%, the changes in the contact pressure and von Mises stress distribution in the tibial cartilage become distinctly different from the prior cases (i.e., where the BML properties were derived from a conversion factor, where the BML was homogenous with a modulus of 33 MPa and homogenous with a modulus of 16 MPa). This suggests that at strains > 10%, the bone in the BML areas would fail and the overlaying cartilage would no longer be supported in these regions, leading to a change in the contact pressure and stress distributions in the cartilage. This may cause damage in the cartilage and perhaps contribute to further cartilage degeneration in knee osteoarthritis. Even without modelling failure in the bone, changes can be seen in the contact pressure and stress distribution in the overlying cartilage. Similar results are seen in Knee 1 which has a smaller simulated BML. The contact pressure and von Mises stress distribution in the tibial cartilage shown in Figure 5.15 and Figure 5.16 begin to show a distinctive change from the Homogenous 16 MPa case where the peak minimum principal strain in the BML region, shown in Figure 5.17, is at ~ 10%. This suggests that this trend is consistent regardless of size of BML.

Comparing the case with a heterogeneous BML based on the conversion factor derived in Chapter 4 to the case with the homogenous BML with averaged elastic modulus of 33 MPa, for both Knee 6 and Knee 1, it can be seen that there are some differences in the peak minimum principal strain and the distribution of the strain in the BML area shown in Figure 5.14 and Figure 5.17. However, there is no observable difference in the contact pressure and von Mises stress distribution between these cases. This suggests that for augmentation techniques, such as subchondroplasty, a homogenous material with close enough elastic modulus to the surrounding bone might be sufficient to restore normal joint mechanics.

Chapter 6 : Discussion and Conclusion

6.1 Introduction

The aim of this thesis was to investigate the effect of bone marrow lesions on knee joint mechanics in knee osteoarthritis. To achieve this aim, finite element models were developed that incorporated BMLs in the tibia. Different scenarios were tested and the results provided understanding of the different aspects of modelling a BML. Methods were also developed to characterize the elastic material properties of small volumes of bone using a combination of experimental compression tests and specimen-specific image-based FE models. Following the results, the methods were adapted and translated to human cadaveric bone to determine elastic material properties for bone in BML and non-BML regions of the human patella. Finally, the results from experimental models were incorporated into specimen-specific computational models of natural knee joints to evaluate the effect of BMLs in real human knees. The methodologies and results of the individual studies were discussed at the end of each chapter. In this chapter, an overview of the methods and results from each chapter is discussed along with their limitations and clinical significance. The overall conclusions from the thesis are also presented here, and recommendations are made for the continuation of this work.

6.2 Discussion of Methods and Limitations

In Chapter 3, a method was described to characterize mechanical properties of bone based on CT image data. The use of porcine bone in this study allowed the method to be tested on more abundant tissue before translation to the limited human tissue in Chapter 4. The method made use of simple compression tests to determine the experimental stiffness of small volumes of bone. Simple compression tests of cylindrical specimens between platens have been used successfully for mechanical testing of bone but in Section 4.2.1, a few bone plugs from a large BML area of patella P6 disintegrated in the surgical scorer and therefore were not tested. Simple compression tests in this manner may not be appropriate for testing specimens with large areas of significantly compromised bone, as the specimens may not withstand being fashioned unto cylindrical shapes. Another method of estimating local mechanical properties such in situ macro-indentation testing using a flat cylinder could be used. This method would avoid the need for excision of bone samples. Nano-indentation tests on individual trabeculae could also be used to evaluate differences in bone tissue properties between bone in BML and non-BML areas.

The computational aspects of this work made use of specimen-specific finite element models created from CT image data. The use of CT image data allowed the geometry including the trabecular architecture to be captured in great detail. The elastic modulus was also mapped and a linear relationship was derived between elastic modulus and CT greyscale image data based on a bone volume fraction method. As discussed in Section 1.4.5.1, the bone volume fraction method has been shown to improve the agreement between computational and experimental results in similar studies compared to a direct method of relating CT greyscale to elastic modulus [91, 113]. The agreement between computational and experimental models was generally better with porcine tissue compared to human tissue, possibly due to wider inter-specimen variability in human bone tissue. The results from the porcine tissue study also highlighted the potential effect of anatomical location on the bone morphology – elastic modulus relationship.

One limitation of using the bone volume fraction method is that it assumes the elastic modulus is governed only by the bone volume fraction and does not take into account differences in tissue properties such as alignment of trabecular struts, proportion of rod-like to plate-like struts or level of mineralization. All of which have been shown to contribute to apparent tissue level stiffness and strength [139, 140].

The specimen-specific finite element models developed in Chapter 5 were created using CT images which allowed the geometry to be captured in great detail but also the definition of inhomogeneous elastic material property based on CT image data. This was done using a bone volume fraction method, whose merits and limitations have already been discussed. The use of inhomogeneous material elastic properties to represent bone has been shown to improve the agreement between computational and experimental results [78]. However, the CT greyscale – elastic modulus relationship used to represent tibia ad femur was derived from patella samples due to lack of availability of samples with BMLs in the tibia or femur. Results from Chapter 3 highlight the potential effect of anatomic site on the CT greyscale – elastic modulus relationships. This may mean that the material properties used to model femur and tibia might not be accurate for those anatomic sites. Only one Tibial specimen was found to have a BML (Knee 6) and this did allow the development of one specimen-specific FE model, with a BML, validated against contact mechanics tests.

As discussed in Section 1.4.4, validation of FE models against experimental tests in similar loading situation provides confidence in the computational results. The validation method also imposes limitations on how the results are applied to a wider population. The

specimen-specific models developed in Chapter 5 were validated for a quasi-static loading scenario, and will not be valid for cyclic loading scenarios investigating wear or fatigue. The outputs validated were contact pressure, qualitative distribution of contact pressure and average force in each compartment. The results of the FE models looked at the distribution of minimum principal strain in the tibia, this was not validated experimentally. Therefore, while comparing the distribution of minimum principal strain between BML and non-BML cases can offer insight to the mechanical effects of BMLs, the strain results cannot be extrapolated as a quantification of damage or failure of trabeculae in the wider population.

6.3 Discussion of Results and Clinical Significance

The results of the bone modulus optimization for non-BML and BML bone, reported in Chapter 4, show that different CT greyscale – elastic modulus relationships were derived for non-BML and BML bone. Some work has been done to highlight some differences between bone in BML regions in comparison to bone in non-BML regions of the tibia [59], this work for the first time quantifies these differences with respect to elastic material properties. A study looking at early arthritic trabecular bone from the proximal tibia found lower bone tissue modulus in areas with overlying cartilage damage compared with unaffected areas [55]. While the study does not mention BMLs specifically, BMLs have been shown to collocate with overlying cartilage damage both in literature [62] and in this study (Section 4.2.1). The conversion factor derived for bone in BML regions (92 MPa) was lower than that derived for non-BML regions (177 MPa) despite a similar average and range of BV/TV values. This would mean lower elastic modulus in the BML regions compared to non-BML regions. Knowledge of how the material properties of bone in BML areas differ from unaffected bone provides valuable information for the development of interventions for treating bone marrow lesions and for developing materials to be used in augmentation techniques such subchondroplasty. The study was limited by availability of tibia and femur specimens. The study was carried out on patella samples. It is therefore difficult to say if the relationships derived for BML and non-BML areas and the challenges encountered are specific to patella tissue.

The development of FE models of the tibiofemoral joint to incorporate a BML area was described in Chapter 2. The models allowed the investigation of different aspects of a BML to determine what parameters were most important when modelling a BML. Parametric studies were conducted on the size, shape, location and elastic modulus of the BML to determine how the effect of different aspects of a BML on the contact mechanics

in the knee. As discussed in Section 2.5, the results showed that larger BMLs closer to the surface and aligned with the centre of contact had the greatest effect on contact pressure and von Mises stress distribution in the tibia. These effects were also more pronounced in cases where the cartilage was completely degenerated. Results from Chapter 5 also show changes in the distribution of contact pressure and stress in the overlying cartilage in cases where BML bone properties are poor. These results suggest that the mechanical effects of BMLs could contribute to arthritic degeneration in a somewhat cyclic manner where damage to the cartilage causes increased bone stress in BML areas which worsen the mechanical property of bone in those areas leading to changes in the distribution of overlying cartilage. Increased cartilage pressure and stress in typically unloaded areas with thin cartilage could then cause more damage to the cartilage in those areas.

There is conflicting evidence in the literature about BMLs and their relationship to OA symptoms. Guermazi et al [7] found that BMLs were prevalent in both painful and painless knees and the results from Chapter 2 show that smaller BMLs, and BMLs farther away from the centre of contact, distally and laterally, are less likely to have an effect on the stress distribution in the tibia. Since, Guermazi et al do not consider location or size of BMLs in their study, it is possible that there is a mix of BMLs likely and unlikely to cause mechanical effects in that study. Felson et al [8] found that increasing BML size was correlated with development of pain. Results from Chapter 2 also show that increase in BML size led to increase in the maximum contact pressure and stress in the tibia. These mechanical effects may be linked to the likelihood of further damage to the surrounding bone and subsequently, to pain.

Classification systems typically used for grading BMLs were discussed in section 1.3.2.3. The WORMS, MOAKS and BLOKS classification systems focus on the overall volume of BMLs, however results from Chapter 2 show that there are other important characteristics of the BML that influence its mechanical effects. The location of the BML (with respect to the centre of contact and the surface of the tibia) has been shown in to be influence BML mechanical effect, with BMLs closer to the surface and aligned with the centre of contact having more effect on the stress in the tibia compared to BMLs which are not. The Compagnoni classification system classifies the BML based on location and loosely, size. Articular and distal BMLs of the Compagnoni classification system were modelled in Chapter 2. Results show that distal BMLs, which have some unaffected bone region between the BML and tibia surface have less of effect on the joint contact

mechanics compared to articular BMLs which go up to the tibia surface. However, the Compagnoni classification has not yet been used in clinical studies. Clinical studies should make use of robust classification systems that take into account shape, size and location of the BML to investigate the mechanical effects of the BMLs and identify subsets of patients most affected by BMLs. The models developed in this study could provide a basis for identifying BMLs most likely to cause mechanical effects and stratifying patients most likely to benefit from treatment of BML based on size and BML shape.

The results from Chapter 2 showed that localized changes to the elastic modulus could have whole tibia effects highlighting the need to determine physically representative material properties for bone in BML areas. In Chapter 5, finite element methods developed in Chapter 2 and the information on the material properties of bone in BML and non-BML derived in Chapter 4 were combined using specimen-specific FE models. The specimen-specific FE models were validated against experimental contact mechanics tests which gives confidence in their ability to replicate the experimental set up. The FE models were used to model cases with and without BMLs and cases with worse BML properties than those derived in Chapter 5. The results showed no observable differences between cases with and without BMLs using the derived properties for BML and non-BML bone from Chapter 4. This is similar trend to the results from Model 3 (Section 2.4.2) which showed little difference in the distribution of contact pressure and von Mises stress in the tibial cartilage between the baseline case with no BML and a case with the BML represented with an elastic modulus half of the surrounding bone. This suggests that 'milder' cases of BMLs, where the bone can be extracted and tested, have little effect on joint contact mechanics and may not benefit from treatment with an augmentation technique like subchondroplasty. However, some of the bone plugs from Patella P6 crumbled in the surgical corer and were not tested. This crumbling during sample preparation suggests that material properties in some BML areas may be much worse than was derived using the specimens that were tested. In Chapters 2.3, 2.4 and Chapter 5.2.7, cases were considered with BML elastic modulus much lower than the surrounding bone. Results show an increase in the compressive strains in the BML regions which may cause remodelling within the BML and immediate surrounding regions, evidence of which has been reported in literature [55, 59]. Although the majority of the BML volumes modelled in Chapter 2 and Chapter 5 are small and most likely Grade 1 on both the WORMS and MOAKS classification systems, the trends seen in the result are repeated for a large BML,

modelled in Section 5.2.7, which provides confidence that the effects of BML material property seen is independent of size.

Subchondroplasty has been proposed as a treatment for BMLs by filling BML areas with bone substitute material with uniform material property. While the mechanical properties of the bone substitute material might vary from what was used in this thesis, the results from Section 5.3.3 show replacing inhomogeneous bone in the BML regions with homogenous material with comparable average elastic modulus appears to have little effect on the contact mechanics. The results also show that the mechanical properties of the bone substitute material do not have to exactly match that of normal bone, this flexibility in the specificity of the material property means that the same material could be applied to wide patient groups without compromising on outcomes. The concept of subchondroplasty using a homogenous bone substitute material has some merits, although further work is needed to identify cases where the properties of bone in BML regions are poor enough to benefit from augmentation.

6.4 Recommendations for future work

The agreement between computational and experimental results for the bone modulus optimization of human cadaveric bone was poor, although other studies using similar methods have reported good agreement. Carrying out the same bone modulus optimization on bone specimens from BML and non-BML regions of the femur and tibia will provide a better understanding of the issues here and highlight any differences due to anatomic site variation. For the experimental mechanical testing portion of the bone modulus optimization, a different method of estimating experimental stiffness such as in-situ macro-indentation testing is recommended. This method may be more suited to testing compromised areas of bone.

On the finite element modelling aspect, FE models could be developed to investigate other presentations of BMLs such as 'kissing BML' which refers to two BMLs directly opposing one another across the joint. Kissing BMLs are prevalent in tibiofemoral and patellofemoral joints and have been suggested to be induced by trauma [62]. These BMLs may behave differently to the ones modelled in this thesis. Also, Compagnoni et al [68] classified six types of BMLs based on topographical location and shape. Only two of the six types were modelled in this thesis. It would be interesting to investigate the similarities and differences between the mechanical effects of the different types of BMLs.

6.5 Conclusions

The aim and objectives of this project were outlined in Section 1.6. The work presented in Chapters 2 to 5 have addressed those objectives. The main conclusions from the different chapters are:

- Large BMLs, closer to the surface and aligned to the centre of contact have the biggest effects on knee contact mechanics. This provides a basis for identifying patient subsets that might benefit the most from treatment of BML.

- Articular BMLs, with tibia surface involvement, have more pronounced effect on the joint contact mechanics compared to Distal BMLs, with some area of unaffected bone underlying the cartilage. Especially in cases with the BML contains less stiff bone. This also provides a basis for identifying patient subsets that are likely to benefit the most from BML augmentation techniques like subchondroplasty

- Different bone morphology-to-elastic modulus relationships were found for bone in BML and non-BML areas, suggesting that the bone in BML areas is different to bone in non-BML areas.

- 'mild' BMLs, with up to a 50% reduction in bone stiffness compared to the surrounding bone, have little effect on the joint contact mechanics and as such may not require treatment with augmentation techniques such as subchondroplasty

- Material properties of bone in BML areas could be worse than that derived in this thesis. Less stiff bone in BML areas could lead to higher stresses and deformation in the cartilage and bone and drive further degeneration.

In Summary, the work presented in this thesis has developed new methods for incorporating BMLs in FE models and evaluating the effects of different BML parameters on knee contact mechanics. This has provided, for the first time, a basis for identifying subsets of patients likely to benefit from subchondroplasty. Elastic material properties were also characterized for bone in BML areas, which allowed the mechanical effects of BMLs in the knee to more fully investigated. Specimen-specific FE models of tibiofemoral joints including BMLs, with representative material properties, were created and validated against experimental contact mechanics tests providing tools to test other BML scenarios and treatment options.

References

1. ARTHRITIS RESEARCH UK. *State of Musculoskeletal Health 2018: Arthritis and other musculoskeletal conditions in numbers*. 2018.

2. CHARETTE, R.S., M. SLOAN, R.D. DEANGELIS and G.-C. LEE. Higher rate of early revision following primary total knee arthroplasty in patients under age 55: a cautionary tale. *The Journal of arthroplasty*, 2019, **34**(12), pp.2918-2924.

3. MARTINEZ-CARRANZA, N., A. PETTAS, D. RAZZAZ, E. BROSTRÖM and M. HEDSTRÖM. Younger age is associated with increased odds of manipulation under anesthesia for joint stiffness after total knee arthroplasty. *Journal of Orthopaedics Traumatology: Surgery Research*, 2019, **105**(6), pp.1067-1071.

4. MEEHAN, J.P., B. DANIELSEN, S.H. KIM, A.A. JAMALI and R.H. WHITE. Younger age is associated with a higher risk of early periprosthetic joint infection and aseptic mechanical failure after total knee arthroplasty. *Journal of Bone and Joint Surgery*, 2014, **96**(7), pp.529-535.

5. TOWNSEND, L.A., R.C. ROUBION, D.M. BOURGEOIS, C. LEONARDI, R.S. FOX, V. DASA and G.R. POLLOCK. Impact of age on patient-reported outcome measures in total knee arthroplasty. *J Knee Surg*, 2018, **31**(06), pp.580-584.

6. WITJES, S., R.C. VAN GEENEN, K.L. KOENRAADT, C.P. VAN DER HART, L. BLANKEVOORT, G.M. KERKHOFFS and P. KUIJER. Expectations of younger patients concerning activities after knee arthroplasty: are we asking the right questions? *Quality of Life Research*, 2017, **26**(2), pp.403-417.

7. GUERMAZI, A., J. NIU, D. HAYASHI, F.W. ROEMER, M. ENGLUND, T. NEOGI, P. ALIABADI, C.E. MCLENNAN and D.T. FELSON. Prevalence of abnormalities in knees detected by MRI in adults without knee osteoarthritis: population based observational study (Framingham Osteoarthritis Study). *Bmj*, 2012, **345**, p.e5339.

8. FELSON, D.T., J. NIU, A. GUERMAZI, F. ROEMER, P. ALIABADI, M. CLANCY, J. TORNER, C.E. LEWIS and M.C. NEVITT. Correlation of the development of knee pain with enlarging bone marrow lesions on magnetic resonance imaging. *Arthritis & Rheumatism: Official Journal of the American College of Rheumatology*, 2007, **56**(9), pp.2986-2992.

9. JAVAID, M.K., J. LYNCH, I. TOLSTYKH, A. GUERMAZI, F. ROEMER, P. ALIABADI, C. MCCULLOCH, J. CURTIS, D. FELSON and N.E. LANE. Pre-

radiographic MRI findings are associated with onset of knee symptoms: the most study. *Osteoarthritis and Cartilage*, 2010, **18**(3), pp.323-328.

10. ROEMER, F.W., C.K. KWOH, M.J. HANNON, D.J. HUNTER, F. ECKSTEIN, T. FUJII, R.M. BOUDREAU and A. GUERMAZI. What comes first? Multitissue involvement leading to radiographic osteoarthritis: magnetic resonance imaging–based trajectory analysis over four years in the Osteoarthritis Initiative. *Arthritis & rheumatology*, 2015, **67**(8), pp.2085-2096.

11. SHARKEY, P.F. and C.F. LEINBERRY. *Osteoarthritis treatment and device*. Patent number: US91446507P.

12. COHEN, S.B. and P.F. SHARKEY. Subchondroplasty for Treating Bone Marrow Lesions. *J Knee Surg*, 2016, **29**(7), pp.555-563.

13. COHEN, S.B. and P.F. SHARKEY. Surgical treatment of osteoarthritis pain related to subchondral bone defects or bone marrow lesions: subchondroplasty. *Tech Knee Surg*, 2012, **11**(4), pp.170-175.

14. CHATTERJEE, D., A. MCGEE, E. STRAUSS, T. YOUM and L. JAZRAWI. Subchondral Calcium Phosphate is Ineffective for Bone Marrow Edema Lesions in Adults With Advanced Osteoarthritis. *Clin Orthop Relat Res*, 2015, **473**(7), pp.2334-42.

15. FARR, J. and S.B. COHEN. Expanding Applications of the Subchondroplasty Procedure for the Treatment of Bone Marrow Lesions Observed on Magnetic Resonance Imaging. *Operative Techniques in Sports Medicine*, 2013, **21**(2), pp.138-143.

16. FODOR, P., R. PREJBEANU, V. PREDESCU, B. CODOREAN, R. FLEACA, M. ROMAN, A. TODOR, O. RUSSU and T. BĂȚAGĂ. Novel surgical technique for bone marrow lesion—case report. *Journal of Interdisciplinary Medicine*, 2016, **1**(s2), pp.27-30.

17. BONADIO, M.B., P.N. GIGLIO, C.P. HELITO, J.R. PÉCORA, G.L. CAMANHO and M.K. DEMANGE. Subchondroplasty for treating bone marrow lesions in the knee – initial experience. *Revista Brasileira de Ortopedia (English Edition)*, 2017, **52**(3), pp.325-330.

18. LEVY, A.S. and K. COUSINS. The rational for and efficacy of subchondroplasty in the injured worker. *Journal of Orthopaedics*, 2020, **22**, pp.48-52.

19. CHHABRA, A., C.C. ELLIOTT and M.D. MILLER. Normal anatomy and biomechanics of the knee. *Sports medicine and arthroscopy review*, 2001, **9**(3), pp.166-177.

20. SOPHIA FOX, A.J., A. BEDI and S.A. RODEO. The basic science of articular cartilage: structure, composition, and function. *Sports health*, 2009, **1**(6), pp.461-468.

21. TECKLENBURG, K., D. DEJOUR, C. HOSER and C. FINK. Bony and cartilaginous anatomy of the patellofemoral joint. *Knee Surgery, Sports Traumatology, Arthroscopy*, 2006, **14**(3), pp.235-240.

22. LOUDON, J.K. BIOMECHANICS AND PATHOMECHANICS OF THE PATELLOFEMORAL JOINT. *Int J Sports Phys Ther*, 2016, **11**(6), pp.820-830.

23. JARRAYA, M., L.E. DIAZ, W.F. ARNDT, F.W. ROEMER and A. GUERMAZI. Imaging of patellar fractures. *Insights into Imaging*, 2017, **8**(1), pp.49-57.

24. PROCTOR, C., M. SCHMIDT, R. WHIPPLE, M. KELLY and V. MOW. Material properties of the normal medial bovine meniscus. *Journal of orthopaedic research*, 1989, **7**(6), pp.771-782.

25. STEWART, T. and R. HALL. (iv) Basic biomechanics of human joints: Hips, knees and the spine. *Current Orthopaedics*, 2006, **20**(1), pp.23-31.

26. STANDRING, S. *In: Gray's anatomy : the anatomical basis of clinical practice*. Forty-second edition. ed. New York: Elsevier, 2021, pp.85 - 126.

27. DONZELLI, P.S., R.L. SPILKER, G.A. ATESHIAN and V.C. MOW. Contact analysis of biphasic transversely isotropic cartilage layers and correlations with tissue failure. *Journal of Biomechanics*, 1999, **32**(10), pp.1037-1047.

28. ATESHIAN, G., W. WARDEN, J. KIM, R. GRELSAMER and V. MOW. Finite deformation biphasic material properties of bovine articular cartilage from confined compression experiments. *Journal of Biomechanics*, 1997, **30**(11-12), pp.1157-1164.

29. MOW, V.C., M.H. HOLMES and W.M. LAI. Fluid transport and mechanical properties of articular cartilage: a review. *Journal of Biomechanics*, 1984, **17**(5), pp.377-394.

30. BUCKWALTER, J.A. and S. LY. Injury and repair of the musculoskeletal soft tissues. *Journal of orthopaedic research*, 1988, **6**, pp.907 - 931.

31. BUCKWALTER, J. and H. MANKIN. Articular Cartilage: Part I Tissue Design and Chondrocyte-Matrix Interactions. *JBJS*, 1997, **79**(4), pp.600-611.

32. BUCKWALTER, J.A., V.C. MOW and A. RATCLIFFE. Restoration of injured or degenerated articular cartilage. *JAAOS-Journal of the American Academy of Orthopaedic Surgeons*, 1994, **2**(4), pp.192-201.

33. RHO, J.-Y., L. KUHN-SPEARING and P. ZIOUPOS. Mechanical properties and the hierarchical structure of bone. *Medical engineering & physics*, 1998, **20**(2), pp.92-102.

34. REZNIKOV, N., R. SHAHAR and S. WEINER. Bone hierarchical structure in three dimensions. *Acta Biomaterialia*, 2014, **10**(9), pp.3815-3826.

35. MOW, V.C. and R. HUISKES. *Basic orthopaedic biomechanics & mechano-biology.* Lippincott Williams & Wilkins, 2005.

36. WEINER, S. and H.D. WAGNER. The material bone: structure-mechanical function relations. *Annual review of materials science*, 1998, **28**(1), pp.271-298.

37. GOLDSTEIN, S.A. The mechanical properties of trabecular bone: Dependence on anatomic location and function. *Journal of Biomechanics*, 1987, **20**(11), pp.1055-1061.

38. RHO, J.Y., M.C. HOBATHO and R.B. ASHMAN. Relations of mechanical properties to density and CT numbers in human bone. *Medical engineering & physics*, 1995, **17**(5), pp.347-355.

39. KEAVENY, T.M., T.P. PINILLA, R.P. CRAWFORD, D.L. KOPPERDAHL and A. LOU. Systematic and random errors in compression testing of trabecular bone. 1997, **15**(1), pp.101-110.

40. ODGAARD, A., I. HVID and F. LINDE. Compressive axial strain distributions in cancellous bone specimens. *Journal of Biomechanics*, 1989, **22**(8-9), pp.829-835.

41. PEAT, G., R. MCCARNEY and P. CROFT. Knee pain and osteoarthritis in older adults: a review of community burden and current use of primary health care. *Annals of the rheumatic diseases*, 2001, **60**(2), pp.91-97.

42. HENSOR, E.M., B. DUBE, S.R. KINGSBURY, A. TENNANT and P.G. CONAGHAN. Toward a clinical definition of early osteoarthritis: Onset of patient-reported knee pain begins on stairs. Data from the osteoarthritis initiative. *Arthritis care & research*, 2015, **67**(1), pp.40-47.

43. KELLGREN, J.H. Epidemiology of chronic rheumatism. *Atlas of standard radiographs of arthritis*, 1963.

44. WONG, S.H.J., K.Y. CHIU and C.H. YAN. Review Article: Osteophytes. *Journal of Orthopaedic Surgery*, 2016, **24**(3), pp.403-410.

45. B., G.M. and G.S. R. Articular cartilage and subchondral bone in the pathogenesis of osteoarthritis. *Annals of the New York Academy of Sciences*, 2010, **1192**(1), pp.230-237.

46.   GOLDRING, M.B. and K.B. MARCU. Cartilage homeostasis in health and rheumatic diseases. *Arthritis research & therapy*, 2009, **11**(3), p.224.

47.   HARDINGHAM, T. and M. BAYLISS. Proteoglycans of articular cartilage: changes in aging and in joint disease. *In: Seminars in arthritis and rheumatism*: Elsevier, 1990, pp.12-33.

48.   GOLDRING, S.R. Role of bone in osteoarthritis pathogenesis. *Medical Clinics of North America*, 2009, **93**(1), pp.25-35.

49.   BULLOUGH, P.G. The role of joint architecture in the etiology of arthritis1. *Osteoarthritis and Cartilage*, 2004, **12**, pp.2-9.

50.   BURR, D.B. Anatomy and physiology of the mineralized tissues: Role in the pathogenesis of osteoarthrosis. *Osteoarthritis and Cartilage*, 2004, **12**, pp.20-30.

51.   MARTIN, R. Targeted bone remodeling involves BMU steering as well as activation. *Bone*, 2007, **40**(6), pp.1574-1580.

52.   RADIN, E.L., H.G. PARKER, J.W. PUGH, R.S. STEINBERG, I.L. PAUL and R.M. ROSE. Response of joints to impact loading—III: Relationship between trabecular microfractures and cartilage degeneration. *Journal of Biomechanics*, 1973, **6**(1), pp.51-57.

53.   RADIN, E.L. and R.M. ROSE. Role of subchondral bone in the initiation and progression of cartilage damage. *Clinical orthopaedics and related research*, 1986, (213), pp.34-40.

54.   RADIN, E.L., D.A. SWANN, I.L. PAUL and P.J. MCGRATH. Factors influencing articular cartilage wear in vitro. *Arthritis & Rheumatism: Official Journal of the American College of Rheumatology*, 1982, **25**(8), pp.974-980.

55.   DAY, J., M. DING, J. VAN DER LINDEN, I. HVID, D. SUMNER and H. WEINANS. A decreased subchondral trabecular bone tissue elastic modulus is associated with pre-arthritic cartilage damage. *Journal of orthopaedic research*, 2001, **19**(5), pp.914-918.

56.   CASTAÑEDA, S., J.A. ROMAN-BLAS, R. LARGO and G. HERRERO-BEAUMONT. Subchondral bone as a key target for osteoarthritis treatment. *Biochemical pharmacology*, 2012, **83**(3), pp.315-323.

57.   WILSON, A., W. MURPHY, D. HARDY and W. TOTTY. Transient osteoporosis: transient bone marrow edema? *Radiology*, 1988, **167**(3), pp.757-760.

58. ZANETTI, M., E. BRUDER, J. ROMERO and J. HODLER. Bone marrow edema pattern in osteoarthritic knees: correlation between MR imaging and histologic findings. *Radiology*, 2000, **215**(3), pp.835-840.

59. HUNTER, D.J., L. GERSTENFELD, G. BISHOP, A.D. DAVIS, Z.D. MASON, T.A. EINHORN, R.A. MACIEWICZ, P. NEWHAM, M. FOSTER, S. JACKSON and E.F. MORGAN. Bone marrow lesions from osteoarthritis knees are characterized by sclerotic bone that is less well mineralized. *Arthritis Res Ther*, 2009, **11**(1), p.R11.

60. HUNTER, D.J., Y. ZHANG, J. NIU, J. GOGGINS, S. AMIN, M.P. LAVALLEY, A. GUERMAZI, H. GENANT, D. GALE and D.T. FELSON. Increase in bone marrow lesions associated with cartilage loss: a longitudinal magnetic resonance imaging study of knee osteoarthritis. *Arthritis Rheum*, 2006, **54**(5), pp.1529-35.

61. ROEMER, F.W., A. GUERMAZI, M.K. JAVAID, J A. LYNCH, J. NIU, Y. ZHANG, D.T. FELSON, C.E. LEWIS, J. TORNER and M.C. NEVITT. Change in MRI-detected subchondral bone marrow lesions is associated with cartilage loss: the MOST Study. A longitudinal multicentre study of knee osteoarthritis. *Annals of the rheumatic diseases*, 2009, **68**(9), pp.1461-1465.

62. BOWES, M.A., S.W. MCLURE, C.B. WOLSTENHOLME, G.R. VINCENT, S. WILLIAMS, A. GRAINGER and P.G. CONAGHAN. Osteoarthritic bone marrow lesions almost exclusively colocate with denuded cartilage: a 3D study using data from the Osteoarthritis Initiative. *Annals of the rheumatic diseases*, 2015.

63. HUNTER, D.J., Y. ZHANG, J. NIU, X. TU, S. AMIN, J. GOGGINS, M. LAVALLEY, A. GUERMAZI, D. GALE and D.T. FELSON. Structural factors associated with malalignment in knee osteoarthritis: the Boston osteoarthritis knee study. *The Journal of Rheumatology*, 2005, **32**(11), pp.2192-2199.

64. GARNERO, P., C. PETERFY, S. ZAIM and M. SCHOENHARTING. Bone marrow abnormalities on magnetic resonance imaging are associated with type II collagen degradation in knee osteoarthritis: A three-month longitudinal study. *Arthritis & Rheumatism*, 2005, **52**(9), pp.2822-2829.

65. PETERFY, C., A. GUERMAZI, S. ZAIM, P. TIRMAN, Y. MIAUX, D. WHITE, M. KOTHARI, Y. LU, K. FYE and S. ZHAO. Whole-organ magnetic resonance imaging score (WORMS) of the knee in osteoarthritis. *Osteoarthritis and Cartilage*, 2004, **12**(3), pp.177-190.

66.   HUNTER, D.J., G.H. LO, D. GALE, A.J. GRAINGER, A. GUERMAZI and P.G. CONAGHAN. The reliability of a new scoring system for knee osteoarthritis MRI and the validity of bone marrow lesion assessment: BLOKS (Boston–Leeds Osteoarthritis Knee Score). *Annals of the rheumatic diseases*, 2008, **67**(2), pp.206-211.

67.   HUNTER, D.J., A. GUERMAZI, G.H. LO, A.J. GRAINGER, P.G. CONAGHAN, R.M. BOUDREAU and F.W. ROEMER. Evolution of semi-quantitative whole joint assessment of knee OA: MOAKS (MRI Osteoarthritis Knee Score). *Osteoarthritis and Cartilage*, 2011, **19**(8), pp.990-1002.

68.   COMPAGNONI, R., J. LESMAN, P. FERRUA, A. MENON, C. MINOLI, M. GALLAZZI, M. DOMŻALSKI and P. RANDELLI. Validation of a new topographic classification of bone marrow lesions in the knee: the six-letter system. *Knee Surgery, Sports Traumatology, Arthroscopy*, 2021, **29**(2), pp.333-341.

69.   COLON, D.A., B.J.V. YOON, T.A. RUSSELL, F.P. CAMMISA and C. ABJORNSON. Assessment of the injection behavior of commercially available bone BSMs for Subchondroplasty® procedures. *The Knee*, 2015, **22**(6), pp.597-603.

70.   SOWERS, M., C.A. KARVONEN-GUTIERREZ, J.A. JACOBSON, Y. JIANG and M. YOSEF. Associations of anatomical measures from MRI with radiographically defined knee osteoarthritis score, pain, and physical functioning. *J Bone Joint Surg Am*, 2011, **93**(3), pp.241-51.

71.   PAPE, D., G. FILARDO, E. KON, C.N. VAN DIJK and H. MADRY. Disease-specific clinical problems associated with the subchondral bone. *Knee Surgery, Sports Traumatology, Arthroscopy*, 2010, **18**(4), pp.448-462.

72.   YANG, G., J. LIU, F. LI, Z. PAN, X. NI, Y. SHEN, H. XU and Q. HUANG. Bioactive calcium sulfate/magnesium phosphate cement for bone substitute applications. *Materials Science and Engineering: C*, 2014, **35**, pp.70-76.

73.   EDMONDSTON, S., K. SINGER, R. DAY, R. PRICE and P. BREIDAHL. Ex vivo estimation of thoracolumbar vertebral body compressive strength: the relative contributions of bone densitometry and vertebral morphometry. *Osteoporosis international*, 1997, **7**(2), pp.142-148.

74.   ROEMHILDT, M., S. WAGNER and T. MCGEE. Characterization of a novel calcium phosphate composite bone cement: flow, setting, and aging properties.

Journal of Materials Science: Materials in Medicine, 2006, **17**(11), pp.1127-1132.

75. HEINI, P.F., U. BERLEMANN, M. KAUFMANN, K. LIPPUNER, C. FANKHAUSER and P. VAN LANDUYT. Augmentation of mechanical properties in osteoporotic vertebral bones–a biomechanical investigation of vertebroplasty efficacy with different bone cements. *European Spine Journal*, 2001, **10**(2), pp.164-171.

76. JUNGBLUTH, P., M. HAKIMI, J. GRASSMANN, J. SCHNEPPENDAHL, A. KESSNER, M. SAGER, A. HAKIMI, J. BECKER, J. WINDOLF and M. WILD. The progress of early phase bone healing using porous granules produced from calcium phosphate cement. *European journal of medical research*, 2010, **15**(5), p.196.

77. TURNER, A.S.J.E.C.M. Animal models of osteoporosis-necessity and limitations. 2001, **1**(66-81), p.13.

78. DAY, G.A., R.J. COOPER, A.C. JONES, M. MENGONI and R.K. WILCOX. Development of robust finite element models to investigate the stability of osteochondral grafts within porcine femoral condyles. *Journal of the Mechanical Behavior of Biomedical Materials*, 2022, **134**, p.105411.

79. COOPER, R.J., A. LIU, G.A. DAY, V.N. WIJAYATHUNGA, L.M. JENNINGS, R.K. WILCOX and A.C. JONES. Development of robust finite element models of porcine tibiofemoral joints loaded under varied flexion angles and tibial freedoms. *Journal of the Mechanical Behavior of Biomedical Materials*, 2020, **109**, p.103797.

80. PROFFEN, B.L., M. MCELFRESH, B.C. FLEMING and M.M. MURRAY. A comparative anatomical study of the human knee and six animal species. *The Knee*, 2012, **19**(4), pp.493-499.

81. LITTEN-BROWN, J.C., A.M. CORSON and L. CLARKE. Porcine models for the metabolic syndrome, digestive and bone disorders: a general overview. *animal*, 2010, **4**(6), pp.899-920.

82. BEIDOKHTI, H.N., D. JANSSEN, M. KHOSHGOFTAR, A. SPRENGERS, E.S. PERDAHCIOGLU, T. VAN DEN BOOGAARD and N. VERDONSCHOT. A comparison between dynamic implicit and explicit finite element simulations of the native knee joint. *Medical engineering & physics*, 2016, **38**(10), pp.1123-1130.

83. VENÄLÄINEN, M.S., M.E. MONONEN, S.P. VÄÄNÄNEN, J.S. JURVELIN, J. TÖYRÄS, T. VIRÉN and R.K. KORHONEN. Effect of bone inhomogeneity on tibiofemoral contact mechanics during physiological loading. *Journal of Biomechanics*, 2016, **49**(7), pp.1111-1120.

84. HAUT DONAHUE, T.L., M.L. HULL, M.M. RASHID and C.R. JACOBS. A Finite Element Model of the Human Knee Joint for the Study of Tibio-Femoral Contact. *Journal of Biomechanical Engineering*, 2002, **124**(3), pp.273-280.

85. SHIRAZI, R. and A. SHIRAZI-ADL. Computational biomechanics of articular cartilage of human knee joint: Effect of osteochondral defects. *Journal of Biomechanics*, 2009, **42**(15), pp.2458-2465.

86. LI, G., J. GIL, A. KANAMORI and S.L.Y. WOO. A Validated Three-Dimensional Computational Model of a Human Knee Joint. *Journal of Biomechanical Engineering*, 1999, **121**(6), pp.657-662.

87. YENI, Y., C. BROWN and T.L. NORMAN. Influence of bone composition and apparent density on fracture toughness of the human femur and tibia. *Bone*, 1998, **22**(1), pp.79-84.

88. SCHAFFLER, M.B. and D.B. BURR. Stiffness of compact bone: effects of porosity and density. *Journal of Biomechanics*, 1988, **21**(1), pp.13-16.

89. WONG, D.M. and D.J. SARTORIS. Noninvasive method for assessment of bone density, architecture, and biomechanical properties: Fundamental Concepts. *Osteoporosis: Diagnosis and Treatment*, 1996, pp.201-232.

90. VAN DER PERRE, G. and G. LOWET. Physical meaning of bone mineral content parameters and their relation to mechanical properties. *Clinical Rheumatology*, 1994, **13**, pp.33-37.

91. DAY, G.A., A.C. JONES and R.K. WILCOX. Optimizing computational methods of modeling vertebroplasty in experimentally augmented human lumbar vertebrae. *JOR Spine*, 2020, **3**(1), p.e1077.

92. LIU, X.S., P. SAJDA, P.K. SAHA, F.W. WEHRLI and X.E. GUO. Quantification of the Roles of Trabecular Microarchitecture and Trabecular Type in Determining the Elastic Modulus of Human Trabecular Bone. 2006, **21**(10), pp.1608-1617.

93. MORGAN, E.F., H.H. BAYRAKTAR and T.M. KEAVENY. Trabecular bone modulus–density relationships depend on anatomic site. *Journal of Biomechanics*, 2003, **36**(7), pp.897-904.

94. SNYDER, S.M. and E. SCHNEIDER. Estimation of mechanical properties of cortical bone by computed tomography. *Journal of orthopaedic research*, 1991, **9**(3), pp.422-431.

95. MOOTANAH, R., C. IMHAUSER, F. REISSE, D. CARPANEN, R. WALKER, M. KOFF, M. LENHOFF, S. ROZBRUCH, A. FRAGOMEN and Z. DEWAN. Development and validation of a computational model of the knee joint for the evaluation of surgical treatments for osteoarthritis. *Computer methods in biomechanics and biomedical engineering*, 2014, **17**(13), pp.1502-1517.

96. WANG, Y., Y. FAN and M. ZHANG. Comparison of stress on knee cartilage during kneeling and standing using finite element models. *Medical engineering & physics*, 2014, **36**(4), pp.439-447.

97. PEÑA, E., B. CALVO, M.A. MARTÍNEZ and M. DOBLARÉ. A three-dimensional finite element analysis of the combined behavior of ligaments and menisci in the healthy human knee joint. *Journal of Biomechanics*, 2006, **39**(9), pp.1686-1701.

98. GUESS, T.M., G. THIAGARAJAN, M. KIA and M. MISHRA. A subject specific multibody model of the knee with menisci. *Medical engineering & physics*, 2010, **32**(5), pp.505-515.

99. SCHWER, L.E. Guide for Verification and Validation in Computational Solid Mechanics. *The American Society of Mechanical Engineers*, 2009.

100. TOZZI, G., Q.-H. ZHANG and J. TONG. 3D real-time micromechanical compressive behaviour of bone–cement interface: experimental and finite element studies. *Journal of Biomechanics*, 2012, **45**(2), pp.356-363.

101. SRINIVASAN, P., M.A. MILLER, N. VERDONSCHOT, K.A. MANN and D. JANSSEN. Experimental and computational micromechanics at the tibial cement-trabeculae interface. *Journal of Biomechanics*, 2016, **49**(9), pp.1641-1648.

102. JOFE, M.H., T. TAKEUCHI and W.C. HAYES. Compressive behavior of human bone-cement composites. *The Journal of arthroplasty*, 1991, **6**(3), pp.213-219.

103. RACE, A., K.A. MANN and A.A. EDIDIN. Mechanics of bone/PMMA composite structures: an in vitro study of human vertebrae. *Journal of Biomechanics*, 2007, **40**(5), pp.1002-1010.

104. KINZL, M., A. BOGER, P. ZYSSET and D. PAHR. The effects of bone and pore volume fraction on the mechanical properties of PMMA/bone biopsies extracted from augmented vertebrae. *Journal of Biomechanics*, 2011, **44**(15), pp.2732-2736.

105. MANN, K.A., M.A. MILLER, R.J. CLEARY, D. JANSSEN and N. VERDONSCHOT. Experimental micromechanics of the cement–bone interface. *Journal of orthopaedic research*, 2008, **26**(6), pp.872-879.

106. JANSSEN, D., K.A. MANN and N. VERDONSCHOT. Finite element simulation of cement-bone interface micromechanics: A comparison to experimental results. *Journal of orthopaedic research*, 2009, **27**(10), pp.1312-1318.

107. ---. Micro-mechanical modeling of the cement–bone interface: the effect of friction, morphology and material properties on the micromechanical response. *Journal of Biomechanics*, 2008, **41**(15), pp.3158-3163.

108. WAANDERS, D., D. JANSSEN, K.A. MANN and N. VERDONSCHOT. The mechanical effects of different levels of cement penetration at the cement–bone interface. *Journal of Biomechanics*, 2010, **43**(6), pp.1167-1175.

109. HELGASON, B., P. STIRNIMANN, R. WIDMER, A. BOGER and S. FERGUSON. Influence of cement stiffness and bone morphology on the compressive properties of bone–cement composites in simulated vertebroplasty. *Journal of Biomedical Materials Research Part B: Applied Biomaterials*, 2013, **101**(2), pp.364-374.

110. CHEVALIER, Y., D. PAHR, M. CHARLEBOIS, P. HEINI, E. SCHNEIDER and P. ZYSSET. Cement Distribution, Volume, and Compliance in Vertebroplasty: Some Answers From an Anatomy-Based Nonlinear Finite Element Study. *Spine*, 2008, **33**(16), pp.1722-1730.

111. KINZL, M., J. SCHWIEDRZIK, P.K. ZYSSET and D.H. PAHR. An experimentally validated finite element method for augmented vertebral bodies. *Clinical Biomechanics*, 2013, **28**(1), pp.15-22.

112. WIJAYATHUNGA, V.N., A.C. JONES, R.J. OAKLAND, N.R. FURTADO, R.M. HALL and R.K. WILCOX. Development of specimen-specific finite element models of human vertebrae for the analysis of vertebroplasty. *Journal of Engineering in Medicine*, 2008, **222**(2), pp.221-228.

113. ROBSON BROWN, K., S. TARSUSLUGIL, V.N. WIJAYATHUNGA and R.K. WILCOX. Comparative finite-element analysis: a single computational modelling method can estimate the mechanical properties of porcine and human vertebrae. *Journal of the Royal Society Interface*, 2014, **11**(95), p.20140186.

114. ERDEMIR, A. Open knee: a pathway to community driven modeling and simulation in joint biomechanics. *Journal of Medical Devices*, 2013, **7**(4), p.040910.

115. RHO, J.Y., R.B. ASHMAN and C.H. TURNER. Young's modulus of trabecular and cortical bone material: ultrasonic and microtensile measurements. *Journal of Biomechanics*, 1993, **26**(2), pp.111-119.

116. MAAS, S.A., B.J. ELLIS, D.S. RAWLINS and J.A. WEISS. Finite element simulation of articular contact mechanics with quadratic tetrahedral elements. *Journal of Biomechanics*, 2016, **49**(5), pp.659-667.

117. TADEPALLI, S.C., A. ERDEMIR and P.R. CAVANAGH. Comparison of hexahedral and tetrahedral elements in finite element analysis of the foot and footwear. *Journal of Biomechanics*, 2011, **44**(12), pp.2337-2343.

118. JOHNSON, K.L. *Contact mechanics.* Cambridge university press, 1987.

119. MCERLAIN, D.D., J.S. MILNER, T.G. IVANOV, L. JENCIKOVA-CELERIN, S.I. POLLMANN and D.W. HOLDSWORTH. Subchondral cysts create increased intra-osseous stress in early knee OA: A finite element analysis using simulated lesions. *Bone*, 2011, **48**(3), pp.639-646.

120. ANWAR, A., Z. HU, Y. ZHANG, Y. GAO, C. TIAN, X. WANG, M.U. NAZIR, Y. WANG, Z. ZHAO, D. LV, Z. ZHANG, H. ZHANG and G. LV. Multiple Subchondral Bone Cysts Cause Deterioration of Articular Cartilage in Medial OA of Knee: A 3D Simulation Study. *Frontiers in bioengineering and biotechnology*, 2020, **8**.

121. ROEMER, F.W., R. FROBELL, D.J. HUNTER, M.D. CREMA, W. FISCHER, K. BOHNDORF and A. GUERMAZI. MRI-detected subchondral bone marrow signal alterations of the knee joint: terminology, imaging appearance, relevance and radiological differential diagnosis. *Osteoarthritis Cartilage*, 2009, **17**(9), pp.1115-31.

122. AN, Y.H. and R.A. DRAUGHN. *Mechanical testing of bone and the bone-implant interface.* CRC press, 1999.

123. MENGONI, M. *opti4Abq, a generic Python code to run Abaqus in an optimisation loop*. 2015.

124. ZYSSET, P.K., X.E. GUO, C.E. HOFFLER, K.E. MOORE and S.A.J.J.O.B. GOLDSTEIN. Elastic modulus and hardness of cortical and trabecular bone lamellae measured by nanoindentation in the human femur. 1999, **32**(10), pp.1005-1012.

125. ZAPATA-CORNELIO, F.Y., G.A. DAY, R.H. COE, S.N.F. SIKORA, V.N. WIJAYATHUNGA, S.M. TARSUSLUGIL, M. MENGONI and R.K. WILCOX. Methodology to Produce Specimen-Specific Models of Vertebrae: Application to

Different Species. *Annals of Biomedical Engineering*, 2017, **45**(10), pp.2451-2460.

126. MENGONI, M. Using inverse finite element analysis to identify spinal tissue behaviour in situ. *Methods*, 2021, **185**, pp.105-109.

127. KORIA, L., M. MENGONI and C. BROCKETT. Estimating tissue-level properties of porcine talar subchondral bone. *Journal of the Mechanical Behavior of Biomedical Materials*, 2020, **110**, p.103931.

128. ODGAARD, A. and F. LINDE. The underestimation of Young's modulus in compressive testing of cancellous bone specimens. *Journal of Biomechanics*, 1991, **24**(8), pp.691-698.

129. JACOBS, C.R., B.R. DAVIS, C.J. RIEGER, J.J. FRANCIS, M. SAAD and D.P. FYHRIE. The impact of boundary conditions and mesh size on the accuracy of cancellous bone tissue modulus determination using large-scale finite-element modeling. *Journal of Biomechanics*, 1999, **32**(11), pp.1159-1164.

130. VICECONTI, M., R. MUCCINI, M. BERNAKIEWICZ, M. BALEANI and L.J.J.O.B. CRISTOFOLINI. Large-sliding contact elements accurately predict levels of bone–implant micromotion relevant to osseointegration. 2000, **33**(12), pp.1611-1618.

131. KEAVENY, T.M., R.E. BORCHERS, L.J. GIBSON and W.C. HAYES. Trabecular bone modulus and strength can depend on specimen geometry. *Journal of Biomechanics*, 1993, **26**(8), pp.991-1000.

132. ANG, B.L.S., Y.J. TAN, Y.J.P. NG, S.H.F. ONG, S.Y. YAP, S.X. GWEE, S.M. CHOU, C.L. POH and K.S. YEW. The Effect of Specimen Geometry on the Mechanical Behavior of Trabecular Bone Specimens. *Solid State Phenomena*, 2012, **185**, pp.129-132.

133. KEAVENY, T.M. and W.C. HAYES. A 20-Year Perspective on the Mechanical Properties of Trabecular Bone. *Journal of Biomechanical Engineering*, 1993, **115**(4B), pp.534-542.

134. DOMANDER, R., A. FELDER and M. DOUBE. BoneJ2 - refactoring established research software [version 2; peer review: 3 approved]. 2021, **6**(37).

135. RUEDEN, C.T., J. SCHINDELIN, M.C. HINER, B.E. DEZONIA, A.E. WALTER, E.T. ARENA and K.W. ELICEIRI. ImageJ2: ImageJ for the next generation of scientific image data. *BMC Bioinformatics*, 2017, **18**(1), p.529.

136. LIN, L.I.-K. A Concordance Correlation Coefficient to Evaluate Reproducibility. *Biometrics*, 1989, **45**(1), pp.255-268.

137. TOWNSEND, P., P. RAUX, R. ROSE, R. MIEGEL and E.J.J.O.B. RADIN. The distribution and anisotropy of the stiffness of cancellous bone in the human patella. 1975, **8**(6), pp.363-367.

138. KERRIGAN, J.R., D. SANCHEZ-MOLINA, J. NEGGERS, C. ARREGUI-DALMASES, J. VELAZQUEZ-AMEIJIDE and J.R. CRANDALL. Indentation response of human patella with elastic modulus correlation to localized fractal dimension and bone mineral density. *Journal of the Mechanical Behavior of Biomedical Materials*, 2014, **33**, pp.99-108.

139. MUSY, S.N., G. MAQUER, J. PANYASANTISUK, J. WANDEL and P.K. ZYSSET. Not only stiffness, but also yield strength of the trabecular structure determined by non-linear μFE is best predicted by bone volume fraction and fabric tensor. *Journal of the Mechanical Behavior of Biomedical Materials*, 2017, **65**, pp.808-813.

140. MAQUER, G., S.N. MUSY, J. WANDEL, T. GROSS and P.K. ZYSSET. Bone Volume Fraction and Fabric Anisotropy Are Better Determinants of Trabecular Bone Stiffness Than Other Morphological Variables. *Journal of Bone and Mineral Research*, 2015, **30**(6), pp.1000-1008.

141. NAZARIAN, A., D. VON STECHOW, D. ZURAKOWSKI, R. MÜLLER and B.D. SNYDER. Bone Volume Fraction Explains the Variation in Strength and Stiffness of Cancellous Bone Affected by Metastatic Cancer and Osteoporosis. *Calcified Tissue International*, 2008, **83**(6), pp.368-379.

142. RAUX, P., P.R. TOWNSEND, R. MIEGEL, R.M. ROSE and E.L. RADIN. Trabecular architecture of the human patella. *Journal of Biomechanics*, 1975, **8**(1), pp.1-7.

143. KATOH, T., M.P. GRIFFIN, H.W. WEVERS and J. RUDAN. Bone hardness testing in the trabecular bone of the human patella. *The Journal of arthroplasty*, 1996, **11**(4), pp.460-468.

144. BAYRAKTAR, H.H., E.F. MORGAN, G.L. NIEBUR, G.E. MORRIS, E.K. WONG and T.M. KEAVENY. Comparison of the elastic and yield properties of human femoral trabecular and cortical bone tissue. *Journal of Biomechanics*, 2004, **37**(1), pp.27-35.

145. TURUNEN, M.J., S. LE CANN, E. TUDISCO, G. LOVRIC, A. PATERA, S.A. HALL and H. ISAKSSON. Sub-trabecular strain evolution in human trabecular bone. *Scientific Reports*, 2020, **10**(1), p.13788.

146.   BAY, B.K., T.S. SMITH, D.P. FYHRIE and M. SAAD. Digital volume correlation: Three-dimensional strain mapping using X-ray tomography. *Experimental Mechanics*, 1999, **39**(3), pp.217-226.

147.   CARRETTA, R., E. STÜSSI, R. MÜLLER and S. LORENZETTI. Within subject heterogeneity in tissue-level post-yield mechanical and material properties in human trabecular bone. *Journal of the Mechanical Behavior of Biomedical Materials*, 2013, **24**, pp.64-73.

Appendix A: University of Leeds IMBE human tissue archive codes for human tissue samples

The human tissue samples used in this thesis were obtained from a tissue bank (MedCure Inc, USA) following National Research Ethics Committee (NREC) approval (reference 18/EM/0224). This study was part of a wider programme of work using whole cadaveric human knees. The archive codes for the samples used in this thesis with respect to the wider body of work are presented in Table A.1 and Table A.2

Table A.1: Human patella samples archive codes

Patella	Left/Right	Height (m)
P1	L	LTKN8941
P2	R	RTKN0668
P3	R	RTKN2795F
P4	L	LTKN7607
P5	R	RTKN9332
P6	R	RTKN9203R

Table A.2: Human knee samples archive codes

	Left/Right Knee	IMBE archive code
Knee 1	L	LTKN1468
Knee 2	L	LTKN8941
Knee 3	R	RTKN0668
Knee 4	L	LTKN9164R
Knee 5	R	RTKN2741
Knee 6	L	LTKN9347